A study of tau lepton production in $t\bar{t}$ events with ATLAS at the LHC

Neil J Collins

Thesis submitted for the degree of

Doctor of Philosophy

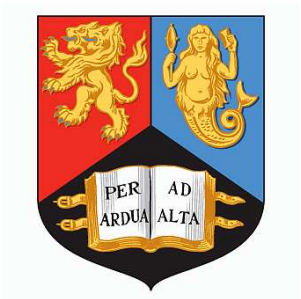

Particle Physics Group,

School of Physics and Astronomy,

University of Birmingham.

September 21, 2011

Abstract

A method is discussed for measuring the $t\bar{t}$ cross section from tau + jets events in early ATLAS data. Multivariant techniques were avoided in favour of simple cuts and the analysis was applied to 26.4pb^{-1}of 2010 data. A cut and count technique was used to estimate the number of $t\bar{t}$ events in a window around the hadronic top mass peak. Subtraction of QCD background from data was performed by scaling events from a QCD enriched sample by the ratio of events in a sideband region. With the current dataset a statistical error is expected of the order of $\pm$400% and a measurement is not feasible at this stage. The systematic error on the $t\bar{t}$ selection efficiency was estimated to be $\pm$50%. Simple luminosity scaling established that a measurement should become possible within the 2011-2013 LHC run. Once ATLAS has collected between 1 fb^{-1} and 3 fb^{-1} of data a fractional error of 20% on the expected number of signal events could be achieved. Suggestions are made for reducing the systematic uncertainty on the $t\bar{t}$ efficiency.

Author's Contribution

The nature of modern day particle physics is such that any work is usually of a collaborative nature. During the production of this thesis I have worked as a member of the Birmingham ATLAS Group, the L1Calorimeter Trigger Group and at different times various subsets of the overall ATLAS Collaboration.

This thesis comprises a collection of three separate areas of work; A study of LVL1 tau trigger efficiencies, a study of different tau identification techniques, and a proposed method for making a measurement ot the $t\bar{t}$ cross section in early ATLAS data. Each of these studies used data samples which were produced centrally by the ATLAS collaboration, while the Athena software framework used was also by necessessity an ATLAS standard.

My contribution involved writing all of the analysis code required to carry out each of the three studies, together with the software required to post process the results. The analyses described in each of the three sections, and all the analysis techniques contained within them, were also my own work. For the tau identification section this involved development of the single variable cuts, which were compared

to a standard set provided by ATLAS. In the cross section analysis the cuts and techniques developed to carry out the measurement were also my own.

To my family

Acknowledgements

It has been a privilege to be a member of the Birmingham Particle Physics Group over the last four years. A substantial part of what has made working in the group so special is the many people who have featured in that time, to whom I am deeply indebted and wish to express my thanks;

Firstly, to Peter Watkins, Dave Charlton and Paul Newman, who gave me the opportunity to study for my PhD in Birmingham during such an exiting period for the LHC, ATLAS and particle physics in general. Also, to the STFC (formerly PPARC) and the British taxpayers, who provided the funding to make it possible.

To my supervisor Alan Watson, for his advice, guidance and friendship over the years, and in particular over the last twelve months. I also apologise for any headaches and sleepless nights I may have contributed to, with the exception of those where licenced premises could have also been envolved.

To Chris Curtis who, when not wearing out his P.C. whistle, welcomed me to the group in the traditional postgrad fashion, and who gave me all the information I needed for visiting CERN; how to register and where, maps of CERN and Geneva,

how to use the buses and, most importantly, the location of the best McDonald's in Balexert.

To Juergen Thomas, for helping with my Athena problems, and for keeping me up to date on all things motorsport in Europe, in particular the DTM. To Miriam and Nigel Watson for their support at deadline time, and to Gilles Mahout and Richard Staley for breakfasts in R1. Also to Paul Thompson who orchestrated the departments representation in the Corporate Relay Challenge.

To Mark Stockton and Joseph Lilley for many memorable evenings, and who with Owen Miller made the RAL Summer School an enjoyable fortnight.

To David Hadley for tea, biscuits and C++, and to Tim Martin for morning coffee.

To Daniel Tapia Takaki for his enduring positivity, even when we couldn't find a home for his most expensive blender, and for interesting chats. For this I also thank Richard Booth and Pablo del Amo Sanchez.

To the many ATLAS students not yet mentioned who have made West 316 the friendliest office one could ever wish to work in; Benedict Allbrooke, Hardeep Bansil, Andrew Chisholm, Martin Gallacher, Ivan Hollins, Tom McLaughlan and Jody Palmer. To Steve Bull for organising the traditional summer lunch at The Bell in Harbourne, and to the other non-ATLAS postgrads I have got to know well; Ravjeet Kour, Zoe Matthews, Sparsh Navin, Arvinder Palaha, Plamen Petrov, Richard Platt, Tony Price, Angela Romano and Patrick Scott.

To Lawrie Lowe for the running repairs on epdt93, and for the laptop loan when my

netbook self-destructed at the worst possible time.

To all the staff in the Birmingham Particle Group for their support, from ATLAS group meetings to helping with masterclass computing sessions. Also to my colleagues at CERN, particularly within the friendly environment of the L1Calo group.

To Gron Jones for his calming influence before my viva, and my examiners John Wilson and Richard Batley.

To all those people, from all walks of life, that I am unanble to mention here but who have taken the time to express an interest in my studies over the years.

Finally, to my parents and my brother Clive, who regardless of my often abrupt replies to their enquiries, have supported me unequivocally throughout!

Neil Collins - 2011

If you can dream - and not make dreams your master;

If you can think - and not make thoughts your aim;

If you can meet with Triumph and Disaster

And treat those two impostors just the same;

Rudyard Kipling - 1895

Contents

List of Figures

List of Tables

Chapter 1

Top Quark and Tau Physics

1.1 Introduction

Particle physics strives to explain the fabric of the known universe by understanding the smallest building blocks from which it is constructed. The Standard Model, considered one of the greatest triumphs of 20^{th} century science, achieves this by describing a series of elementary particles and how they interact. Futhermore, it has made accurate predictions which have subsequently been verified by experiment. This chapter introduces the Standard Model, together with a more detailed coverage of the properties of the top quark, the most recently discovered elementary particle. The relationship between the top quark and the tau lepton is also covered, notably how it provides a possible window on new physics beyond the Standard Model.

1.2 The Standard Model

The Standard Model is the label applied to the theory which describes the current understanding of particle physics. The theory comprises a series of elementary particles and the forces which combine to produce the known matter seen in the universe.

Elementary particles within the Standard Model are refered to as fermions. Fermions have half-integer spin and are divided into two types, known as quarks and leptons [1]. Both types are currently known to each comprise six fundamental particles which are separated into three groups of pairs of particles. Equivalent particles in these three 'generations' have identical properties with the exception of their masses. Generation III particles are more massive than generation II particles, which in turn are more massive than those in generation I (the constituents of all known stable matter in the universe). The arrangement of the fermions within the generations is shown in Fig. 1.1 [2];

A distinction exists between the arrangement of the quarks and leptons within the three generations. In the case of quarks, six distinct versions refered to as flavours exist and are known as up (u), down (d), charm (c), strange (s), top (t) and bottom (b) [1]. The three 'up type' quarks have an electric charge of $+2/3$ while the three 'down type' quarks have a charge of $-1/3$ [2]. In contrast each generation has one massive lepton of charge -1 and one lepton neutrino with zero charge[1]. Consequently there are only three lepton flavours which are labeled as electron(e), muon(μ) and

[1]Electric charge is defined in units of the electron charge [2]

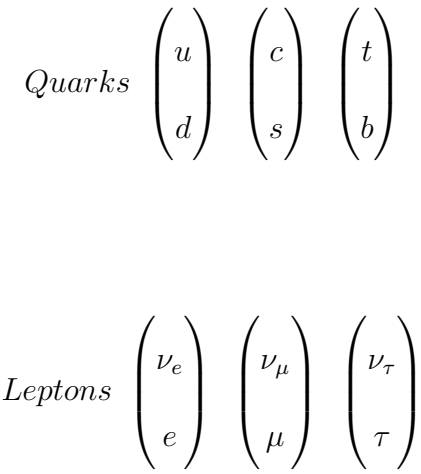

Figure 1.1: The three generations of quarks and leptons within the Standard Model [2]

tau(τ) [2]. For both quarks and leptons an equivalent set of antiparticles exist which have the same properties as the particles but with the sign of all charges, for example the electric charge, plus certain other quantum numbers reversed [1]. Quarks carry a property known as colour charge (red, green or blue), whereas leptons do not. Colour is a quantum number that allows for interactions with the strong force (in an analogy to the interaction of the electric charge with electric fields) but which is not observed in nature. This requires that quarks can only exist in a composite bound combination with overall zero colour. These bound states can either comprise three quarks (one of each colour), refered to as baryons, or alternatively a quark and antiquark pair (one with colour and the other with anticolour), known as mesons [2]. The leptons by contrast only exist as isolated particles.

Of the four known fundamental forces, the effect of the electromagnetic, weak and strong forces on the elementary particles are fully included in the Standard Model.

These forces are modeled by quantum field theories where the interactions between the particles are performed by the exchange of spin 1 gauge bosons [1]. For the electromagnetic force, which acts only on electrically charged particles, the exchange particle is the massless photon and the relevant area of the theory is refered to as Quantum Electrodynamics (QED) [2]. In the case of the strong interaction, the force is carried by one of eight gluon states. While gluons do not carry electric charge, they do possess colour charge. Consequently, gluons interact with quarks (it is the gluons that bind the quarks into baryons and mesons) and can also self-couple, but do not couple to leptons. The area of strong interactions is described by Quantum Chromodynamics (QCD) [2]. Finally, the weak force is accounted for within the Standard Model by exchange of the massive Z^0 and $W^{\pm}$ bosons [1]. These can self-interact but unlike the gluon do not carry colour charge. All fermions do however have weak charges. It is via exchange of the W bosons that quark flavour change is allowed to take place as occurs in beta decay [1].

The field theory is structured around a gauge symmetry described as being $\mathrm{SU}(3)_C \times \mathrm{SU}(2)_L \times \mathrm{U}(1)_Y$ [2]. Within this arrangement QCD and the gluons are covered by $\mathrm{SU}(3)_C$ alone. In contrast, QED and the weak force (with their associated bosons) are together covered by $\mathrm{SU}(2)_L \times \mathrm{U}(1)_Y$ and so are therefore usually refered to as the combined electroweak force [2]. The theory as a whole is required to be gauge invariant [3]

A currently unresolved area of the Standard Model is providing an explanation for why the various particles have their observed masses. This aspect of the theory

must explain why the Z^0 and $W^{\pm}$ bosons are massive but the photon is not, and also accommodate the mass hierarchy seen in the fermions, while at the same time ensuring the theory remains gauge invariant. The part of the Standard Model intended to address this is the Higgs mechanism. Within the Higgs mechanism four scalar fields are added to the theory which are arranged such that the scalar potential has a non-zero Vacuum Expectation Value [1] (the starting point for calculations made using perturbation theory). When combined with the rest of the theory, this allows the bosons and fermions to aquire mass, whilst also requiring the existence of an electrically neutral spin zero scalar particle; the Higgs boson. Unobserved to date at the LEP and TeVatron colliders the search for the Higgs is a major goal of the Large Hadron Collider, while its discovery (or otherwise) would be a significant landmark in particle physics.

1.3 Top Quark Physics

The top quark is the heaviest within the Standard Model, forming the weak isospin partner of the bottom quark in the third quark generation [4]. Fundamental parameters of the Standard Model associated with the top quark are its mass m_{t} and the CKM (Cabbibo-Kobayashi-Maskawa) mixing matrix elements, V_{tb}, V_{ts} and V_{td} [5]. All other Standard Model top quark properties are fixed because they must match those of the up and charm quarks in the first two generations.

Since the discovery of the top quark in March 1995, by the CDF and DØ teams at

the Fermilab TeVatron proton-antiproton collider, all direct measurements prior to 2010 have used the 10^4 top quark events recorded at that accelerator [6]. The first estimate of the top quark mass came from measurements made on twelve events observed in 1994 [7], before the top discovery was confirmed. The events suggested a top mass of;

$$m_{\mathrm{t}} = 174 \pm 10^{+13}_{-12}\ \mathrm{GeV} \tag{1.1}$$

and were fully analyzed in [8]. Subsequent analysis using the complete 100 pb^{-1} Run I Fermilab TeVatron data combined with further data from Run II sets the current value of the top quark mass from direct observation as [9];

$$m_{\mathrm{t}} = 172.0 \pm 0.9 \pm 1.3\ \mathrm{GeV}. \tag{1.2}$$

The matrix element V_{tb} is known less accurately. Results from single top observation at CDF and DØ currently indicte a value for V_{tb} of [9];

$$|V_{\mathrm{tb}}| = 0.88 \pm 0.07. \tag{1.3}$$

During 2010 the ATLAS experiment at the LHC collected approximately 46 pb^{-1} of data. Coupled to the estimated cross section for $\mathrm{t\bar{t}}$ pair production of 160 pb (NLO) [10] at a proton-proton centre-of-mass energy of 7 TeV, approximately 7300 $\mathrm{t\bar{t}}$ events should have been produced. Analysis of these data was ongoing at the

time of writing.

1.4 Standard Model Top Quark Production at Hadron Colliders

Within the Standard Model, top quarks are produced in two different ways at the LHC. These are as a $t\bar{t}$ pair via QCD processes (the strong interaction), or singly by electroweak processes [11]. For mass measurement $t\bar{t}$ pair production events are more convenient. Single top events are useful when measuring the matrix element V_{tb} or examining the W-t-b vertex properties [6].

An important aspect of hadron colliders is that the colliding particles are quark composites bound together by gluons. As a consequence, the production mechanism observed in QCD processes depends on the type and energy of the colliding particles. Within the parton model theory, hadrons are treated as being a collection of quasi-free quarks and gluons [1]. Each parton i within the hadron is taken as carrying a momentum p_i in the prescribed longitudinal direction (this would be taken as the beam direction in a hadron collider) and so possess a fraction $x_i = p_i/p$ of the overall momentum p of the hadron in that direction [1]. Parton Distribution Functions (PDFs) are used to describe the probability density for finding a parton within a hadron possessing a momentum fraction x_i [1], when considered for a given scale Q^2 [3]. When dealing with $t\bar{t}$ production the scale is often taken to be of the order $Q = m_t$, where m_t is the top quark mass [1]. Fig. 1.2 shows the Parton

Distribution Functions (PDFs) of the valence quarks and gluons for Q^2 of 175 GeV^2.

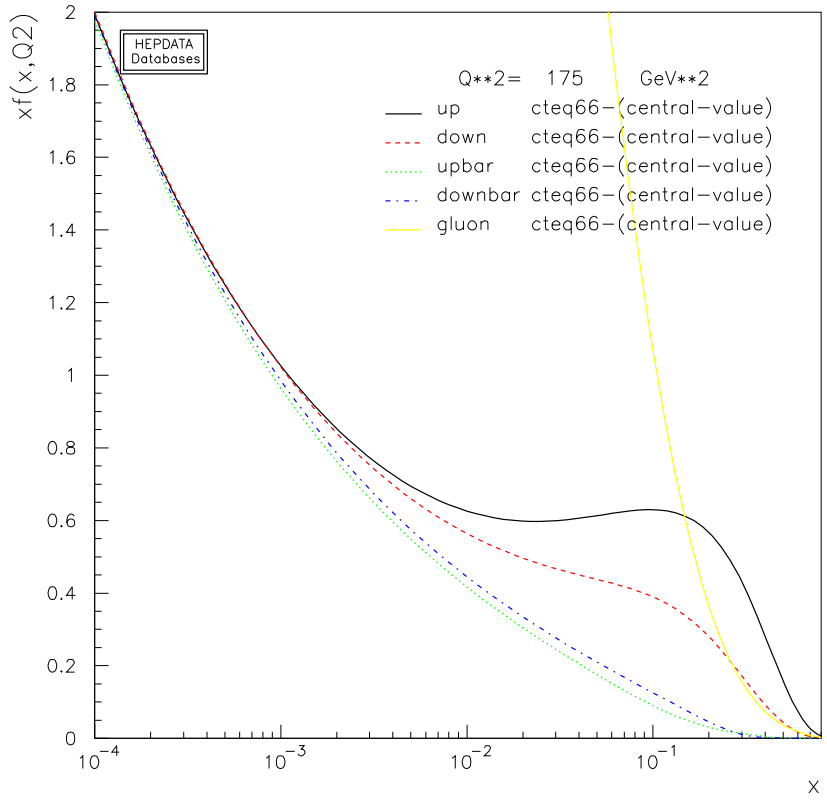

Figure 1.2: Pdf distributions of valence quarks and gluons for Q^2 of 175 GeV^2 [12]

For a symmetrical collider, assuming the colliding partons are of similar x_i, the value of x which is accessible during the collision can be expressed as $x \approx m_t/\sqrt{(s)}$ [1]. For the LHC operating in 7 TeV mode this has a value of 0.05 (0.025 when in 14 TeV configuration). From Fig. 1.2 it can therefore be seen that at the LHC QCD top quark pair production typically occurs for up to small values of the momentum fraction x [3] and so is dominated by gluon-gluon fusion processes [13]. The three lowest level Feynman diagrams for these processes are given in Fig. 1.3.

In contrast, the Fermilab TeVatron 1.96 TeV centre of mass energy collisions are only able to probe down to values of x of approximately 0.2, which is above the

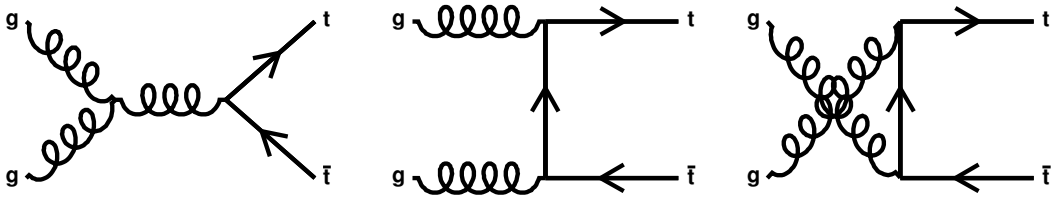

Figure 1.3: Diagrams for $t\bar{t}$ production by gluon-gluon fusion [3]

region where the gluon PDF begins to dominate. When added to the fact that the TeVatron is a proton-antiproton machine, top quark pair production is dominated by quark-antiquark annihilation as shown in Fig. 1.4, contributing 85% of events [14].

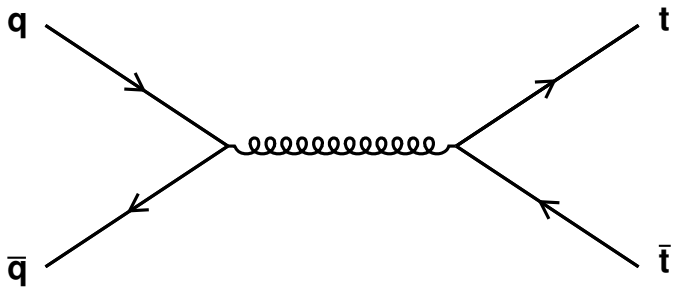

Figure 1.4: Diagram of $t\bar{t}$ production by quark-antiquark anhilation [3]

Electroweak single top production occurs within the Standard Model via three methods; s-channel, t-channel (or W-gluon reactions) and Wt production. The various means by which single top quarks are expected to be produced at the LHC are shown in Fig. 1.5.

A further aspect to consider with regards to top quark production is the variation of the cross section as a function of the centre-of-mass energy of the collision. Fig. 1.6 shows cross sections as a function of centre-of-mass energy for a series of different

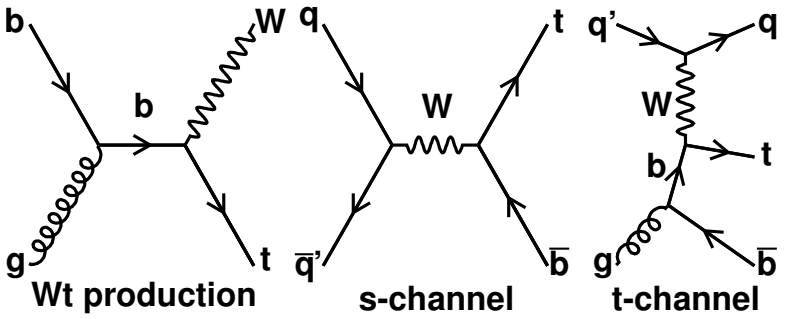

Figure 1.5: Mechanisms for single top quark production [3]

processes. For $t\bar{t}$ production the cross section is predicted to be approximately 160pb for a proton-proton collision energy of 7 TeV [13], which rises to 833pb at 14 TeV (at NLO) [3].

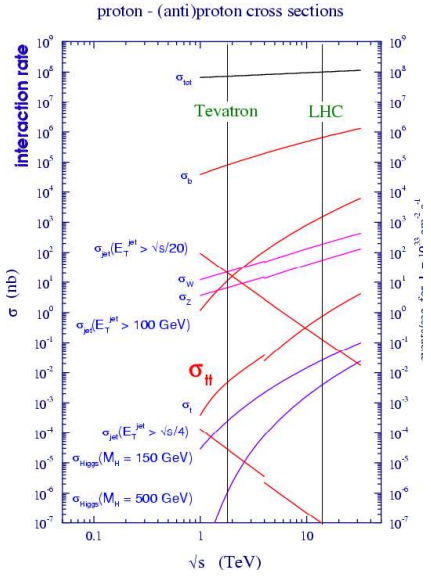

Figure 1.6: Cross sections for production of various physics processes at the TeVatron and LHC as a function of proton - (anti)proton centre of mass energy [3]

1.5 Top Quark Decay within the Standard Model

Quark decays within the Standard Model occur via flavour change through the weak interaction, by exchange of W^+ and W^- bosons. A quark of charge $+2/3$ (u, c, t) is always transformed to a quark of charge $-1/3$ (d, s, b) and vice versa. The top quark can decay to any of the three charge $-1/3$ quarks via W^+ boson exchange, in accordance with the CKM mixing matrix [1]. The CKM matrix elements also define the relationship between the weak and mass quark eigenstates [1].

The CKM matrix is defined as being unitary (assumed for three quark generations [3])and the elements within it squared are proportional to the probability of the corresponding decay occuring [15]. The matrix elements define how strongly the W boson couples to the various quarks. Non zero matrix elements correspond to decays that may occur, while matrix elements that are zero correspond to decays which cannot (no non-zero elements are known to exist, although some are very small). Therefore the matrix elements of the Standard Model define which decays can occur, which cannot and which are suppressed.

The allowed top quark decays; $t \rightarrow bW^+$, $t \rightarrow sW^+$ and $t \rightarrow dW^+$, are represented in the CKM matrix by the elements $|V_{tb}|$, $|V_{ts}|$ and $|V_{td}|$. Assuming $|V_{tb}| = 1$, measurements of the B_s^0 combined with lattice QCD calculations give estimates of $|V_{ts}| = (38.7 \pm 2.1) \times 10^{-3}$ and $|V_{td}| = (8.4 \pm 0.6) \times 10^{-3}$ respectively [9]. A direct measurement without assuming unitarity gives a value of $|V_{tb}| = 0.88 \pm 0.07$ [9]. The $t \rightarrow bW^+$ decay therefore dominates, while the $t \rightarrow sW^+$ and $t \rightarrow dW^+$ decays

are heavily suppressed, possessing expected branching ratios of approximately 0.1% and 0.01% [6]. The top quark undergoes a weak decay and is expected to do so as an isolated quark because the top lifetime (approximately 10^{-24} s) is shorter than the timescale required in QCD for hadrons to form (in the order of 10^{-23} s [8]).

For QCD top production, where a top and an antitop are produced, the antitop will decay following the same process as the top, but with the relative antiparticles. The antitop will therefore decay to an antibottom quark and a W^- boson.

Assuming 100% decay of the top to a bottom quark and W boson, the decay sequence of a $t\bar{t}$ pair is identified by the decay of the W^+ and W^- bosons produced by the decaying top and antitop [8]. Fig. 1.7 shows the generalized standard decay of a $t\bar{t}$ pair.

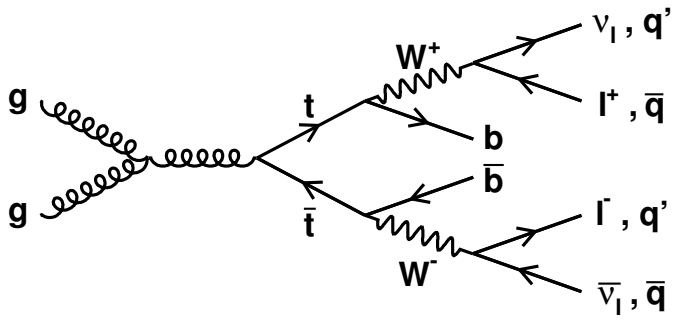

Figure 1.7: Illustration of the general decay for a $t\bar{t}$ pair, assuming 100% branching ratio for $t \rightarrow bW^+$ [8]

Each of the W bosons in a $t\bar{t}$ event may decay to a $q\bar{q}$ pair or to a lepton and neutrino. Consequently there are four classes of $t\bar{t}$ pair decays; single lepton events, dilepton events, fully hadronic events and 'tau plus X' events. Differences in the behaviour of

the tau compared to the electron and muon is the reason that $t\bar{t}$ events containing taus are classified separately, see 1.7.2. The branching ratios for these processes are 30%, 5%, 45% and 20% respectively [6]. The tau+X events are themselves divided in a similar way into tau+jets, tau+lepton and 'two tau' events.

Irrespective of how the W^+ and W^- bosons decay, the bottom and antibottom quarks produced will behave the same way in each case. The bottom quark lifetime is longer than that required for hadrons to form by the strong interaction. Consequently, confinement forces the bottom quark to undergo hadronisation. One of the hadrons produced contains the original bottom quark, usually as a B-meson. A cone of hadrons known as a jet (in this particular case a b-jet) is formed, the axis of which propagates in the same direction as the bottom quark was originally travelling. Any quarks produced from the W decays hadronise in the same way into light quark jets.

1.6 Top Quark Physics at the LHC

The number of top quarks to be produced each year at the LHC will enable a wide range of top quark physics to be carried out. Key areas to be studied include measurement of the top quark mass, searches for non Standard Model heavy resonances, study of electroweak single top production (including measurement of the matrix element V_{tb} and determination of the W-t-b vertex properties [6]), examination of top quark decays, branching ratios and couplings, top quark charge determination,

searches for flavour changing neutral currents (FCNC) and examination of top quark spin correlations. These have been fully described elsewhere, for example in [1] and [3].

1.7 Relation to the Higgs

The electroweak gauge bosons, Higgs boson and the heavy quarks are all interlinked through high order electroweak processes. Fig. 1.8 shows how the top quark and the Standard Model Higgs boson can occur in loop diagrams in relation to the W and Z bosons[3]. By making accurate measurements of electroweak processes, it is possible to extract an estimate of the Standard Model Higgs mass. Adding in the measured top quark and W boson masses allows the Higgs mass to be further refined. Fig. 1.9 illustrates where four different values of the Standard Model Higgs boson would lie in a plot of M_W versus M_t, and how the measured quantities therefore suggest the presence of a relatively light Higgs [3].

1.7.1 Importance of Studying Taus in Top Events

Tau final states are predicted for a number of physics processes, both within and beyond the Standard Model. Assuming the Standard Model, measurement of the $t\bar{t}$ production cross-section with tau+jets and tau+lepton events provides a cross check of measurements made in the electron and muon channels. Tau production has been predicted as a possible signature for certain beyond the Standard Model Higgs

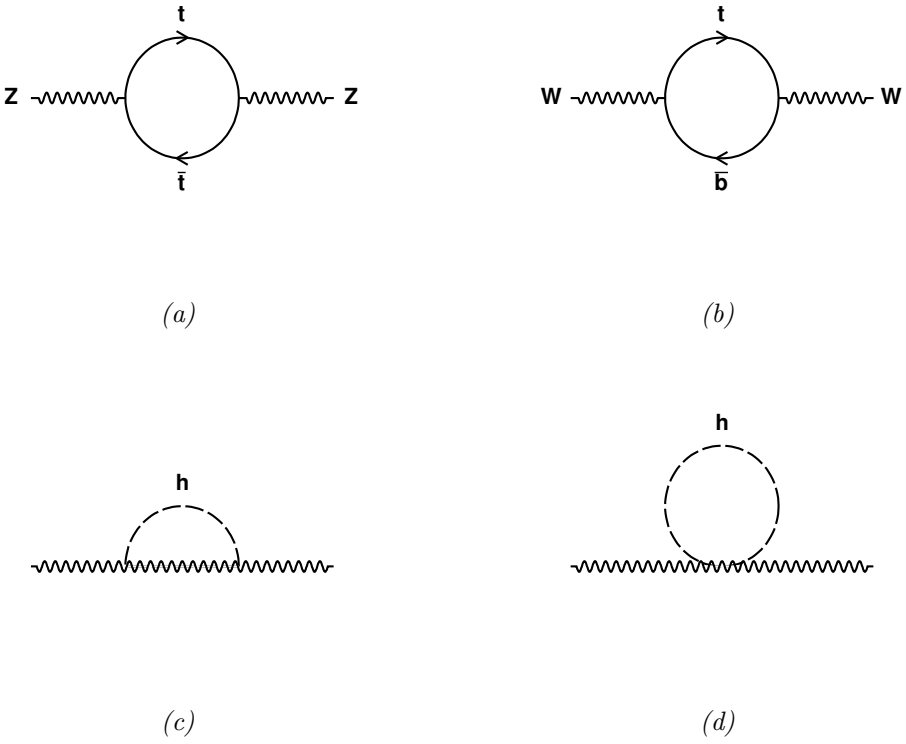

Figure 1.8: Electroweak loop corrections to the W and Z propagators from the top quark (a and b) and from the Higgs boson (c and d) [3]

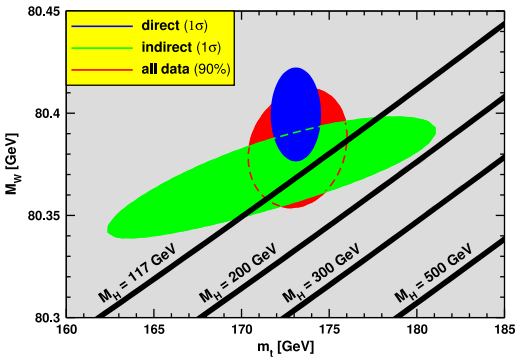

Figure 1.9: Plot of M_W versus M_t showing results from direct and indirect measurements. Lines are shown corresponding to the location of four different Higgs masses in the plane [9]

bosons, various supersymmetry (SUSY) models and other potential new physics [16].

The Standard Model Higgs mechanism consists of only one scalar field doublet [1]. Extensions to the Standard Model however can propose the existence of two Higgs doublets, refered to as Two Higgs Doublet Models (THDM) [1], which come in two types. Type I THDM only allow one doublet to couple to fermions, but in type II THDM (the simplest of which is the Minimal Supersymmetric Standard Model or MSSM) one doublet couples to up type quarks or neutrinos, while the second couples to down type quarks or charged leptons [1]. In both cases, five Higgs bosons are predicted as opposed to one in the Standard Model, comprising three neutral Higgs' h^0, H^0 and A^0, plus a pair of charged Higgs' $H^{\pm}$ [1].

The massive nature of the tau lepton, when compared to electron and muon masses, means that should a light charged Higgs boson exist, it would be expected to couple preferentially to the tau [17]. Fig. 1.10 demonstrates how such a coupling can occur in a $t\bar{t}$ decay, where the charged Higgs (with mass smaller than the difference between

the top and b quark masses) replaces one of the two W bosons in the decay. How such a charged Higgs would decay depends on the value of tan β, which is the ratio of the vacuum expectation values in the two Higgs doublets [1];

$$tan\beta = \frac{v_1}{v_2} \tag{1.4}$$

Such a charged Higgs is predicted in the MSSM to couple strongly to the massive top quark for values of tan $\beta \gtrsim 70$ and $\lesssim 1$ [1]. For tan $\beta > 1$ the $H^+ \rightarrow \tau\nu$ channel, as shown for one of the top quarks in Fig. 1.10, is predicted to feature significantly (rising to a branching fraction close to 100% for tan $\beta > 5$) thus making tops decaying to taus an ideal search candidate [1]. For tan $\beta < 1$ $H^+ \rightarrow c\bar{s}$ dominates while the $t \rightarrow H^+b$ production is minimised for tan β close to 1. The existence of a charged Higgs in the region preferable for tau production would manifest itself as an enhanced branching fraction for $t \rightarrow b\tau\nu$ when compared to the Standard Model [4].

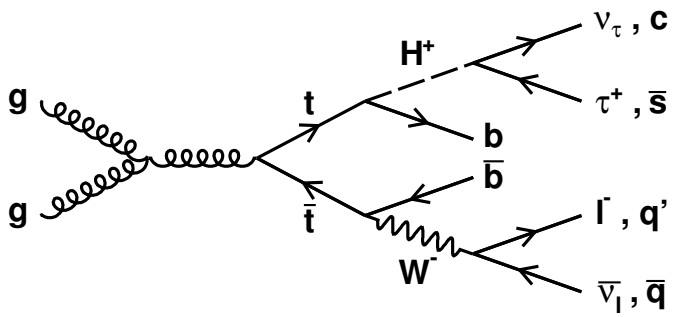

Figure 1.10: Illustration of how a hypothetical charged Higgs boson could be observed in $t\bar{t}$ decay through couplings to the top quark and tau lepton

1.7.2 Tau Decay Classification

The tau is unique in the lepton sector of the Standard Model. Due to its mass of $m_\tau = 1776.99^{+0.29}_{-0.26}$ MeV [18] it is the only one of the three leptons which is allowed to decay either leptonically or hadronically [19]. Consequently taus are classified in accordance with whether they decay to leptons (with branching fractions of $(17.36 \pm 0.05)\%$ to $\mu^- \bar{\nu}_\mu \nu_\tau$, $(17.84 \pm 0.05)\%$ to $e^- \bar{\nu}_e \nu_\tau$, $(3.6 \pm 0.4)\%$ to $\mu^- \bar{\nu}_\mu \nu_\tau \gamma$ and $(1.75 \pm 0.18)\%$ to $e^- \bar{\nu}_e \nu_\tau \gamma$ [18]) or hadrons (with a combined branching fraction of approximately 65%).

For the case where the taus decay into hadrons a further degree of classification is applied in relation to the number of charged mesons (dominated by pions) initially produced. Decays where only one charged pion or kaon is produced are refered to as 1-Prong and comprise mainly of $\tau \rightarrow \pi^\pm \nu$ and $\tau \rightarrow \mathrm{n}\pi^0 \pi^\pm \nu$, accounting for 22.4% and 73.5% of the decays respectively [19]. Likewise, decays producing three charged pions or kaons are refered to as 3-Prong and consist mainly of the modes $\tau \rightarrow 3\pi^\pm \nu$ and $\tau \rightarrow \mathrm{n}\pi^0 3\pi^\pm \nu$, which make up 61.6% and 33.7% of the total number of 3-Prong taus [19]. Note that in both cases $\mathrm{n}\pi^0$ signifies the production of any number of neutral pions. Decays to 1-Prong and 3-Prong modes occur with relative fractions of approximately 85% and 15% of the total hadronic branching fraction respectively [9]. Further 5-Prong and 7-Prong hadronic decays can also occur with negligible branching ratios, but due to their higher track multiplicity are more difficult to distinguish from conventional non-tau jets. The branching fraction to modes containing $K^\pm$ is small, of the order of 1% in both 1-Prong and 3-Prong

cases. These modes are indistinguishable to the ATLAS detector from the equivalent $\pi^{\pm}$ decays [19].

1.8 Conclusions

Within this chapter the Standard Model of particle physics has been introduced and its main features described. Further detail was provided on the top quark, including its decay mechanism and the production methods accessible at hadron colliders. Current experimentally measured values of the top quark mass and the CKM matrix element V_{tb} were given. The relationship between the top quark and the as yet undiscovered Standard Model Higgs boson was also noted. A brief explanation was then given as to why, for certain values of tan β, top quarks decaying to tau leptons can provide a probe for light charged Higgs bosons proposed by certain two Higgs doublet models. Finally, the decay modes of the tau lepton were described and their appropriate branching ratios quoted.

Chapter 2

The LHC and the ATLAS detector

2.1 Introduction

Constructed under the French-Swiss border and assembled over a decade, the Large Hadron Collider (LHC) is often described as the largest machine ever made. Commencing operation in 2010 the LHC is the world's most powerful particle collider, producing data which are analysed by some of the most sophisticated detectors produced to date. Within this chapter can be found a brief overview of the LHC and how it operates. The ATLAS detector is described together with its constituent components, while the physics goals and their demands are mentioned. In addition the ATLAS data structure is also summarised.

2.2 The LHC

The Large Hadron Collider (LHC) accelerates and collides beams of protons or Pb nuclei in the highest energy particle collisions ever produced artificially. The LHC has been constructed at the CERN laboratory in the 27 km circumference tunnel formerly used to house the LEP and LEP II electron - positron colliders between 1989 and 2000. Designed to produce 14 TeV centre of mass energy proton-proton (pp) collisions at a luminosity of 10^{34} $\mathrm{cm}^{-2}\mathrm{s}^{-1}$ [20], during 2010 the LHC operated in proton-proton mode with a centre of mass energy of 7 TeV and up to a maximum luminosity of approximately 2×10^{32} $\mathrm{cm}^{-2}\mathrm{s}^{-1}$. Comprising a mixture of commissioning and physics running, a total of approximately 46 pb^{-1} of proton-proton data were collected during this period [21]. Fermilab's TeVatron proton-antiproton ($\mathrm{p\bar{p}}$) collider, the most powerful machine previously available, has a Run II centre of mass energy of 1.96 TeV and luminosity of approximately 10^{32} $\mathrm{cm}^{-2}\mathrm{s}^{-1}$ [1].

2.2.1 LHC Machine Overview

At the LHC, counter rotating beams of protons are accelerated to a maximum of 7 TeV (3.5 TeV during 2010) and brought together to collide at the centre of the four LHC detectors. At the mimimum bunch spacing configuration collisions are produced every 25 ns. Each bunch will contain up to 1.15×10^{11} protons and will have an RMS length of 0.075 m and a nominal diameter of approximately 1 mm. However, the bunch diameter is further reduced to 16 μm at the collision points. At

full intensity and design energy, each LHC beam will contain 2808 proton bunches 25 ns apart and would hence have a beam energy of approximately 362 MJ.

In order to produce high energy proton beams, a series of different accelerators are used to provide and then ramp the particle energy up in stages, culminating in the LHC main ring. To begin with, the CERN Linac2 linear accelerator is used to produce 50 MeV protons which are then fed into the Proton Synchrotron Booster (PSB). The protons are accelerated to 1.4 GeV in the Booster and are then injected into the Proton Synchrotron (PS) itself where they are further accelerated to 26 GeV. From the PS, the protons pass into the Super Proton Synchrotron (SPS) and are taken up to an energy of 450 GeV before passing down two tunnels, built to link the SPS and the LHC, and filling the two separate LHC beam pipes. Final acceleration of each beam to the desired energy, of up to 7 TeV, occurs within the LHC itself. The chain of accelerators is show in Fig. 2.1

The two proton beams are accelerated within the LHC by strong electric fields provided via radio frequency (RF) cavities (energy is transfered from the radio waves in the cavity to the particles in the beam) and steered around the ring by powerful dipole magnets. As a pp collider, both LHC beams possess the same charge. To keep two counter rotating proton beams travelling around the LHC ring, the directions of the magnetic fields applied to the two beams must be exactly opposite so that each beam is bent the correct way. Beams are contained in separate pipes with a magnetic field applied independently to each one. The beam energy limit obtainable at the LHC is determined by the maximum bending power of these magnets to keep

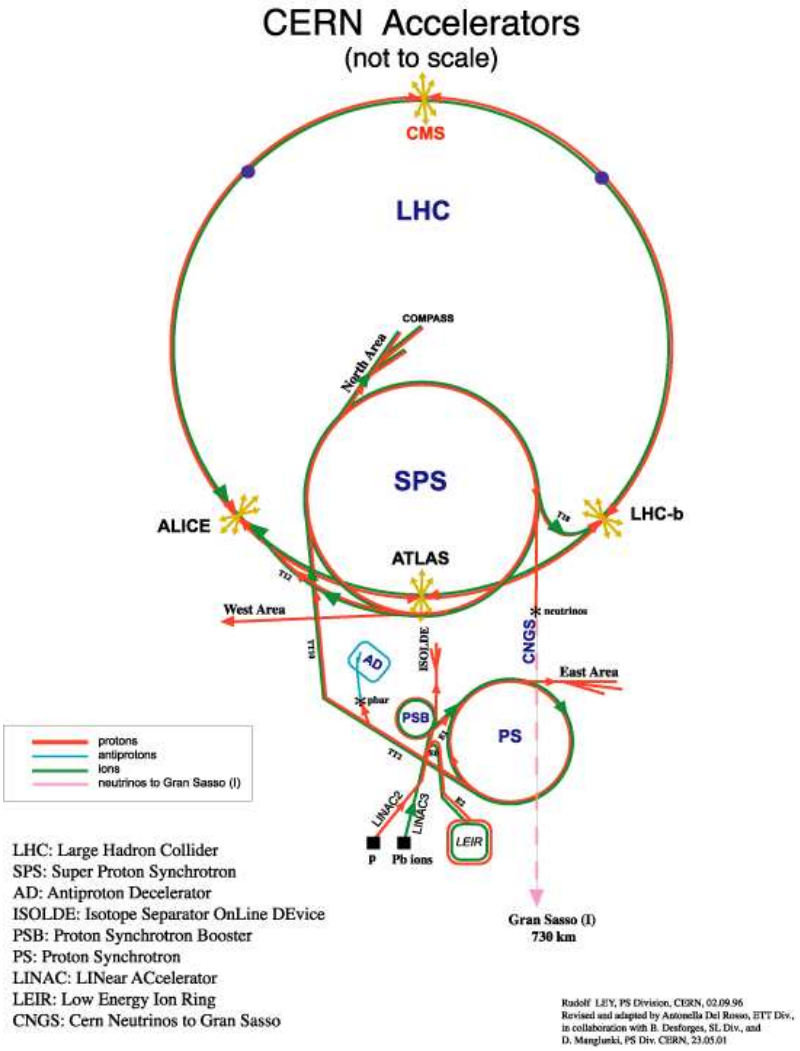

Figure 2.1: Schematic showing the accelerators used to produce 7 TeV protons at the LHC. 50 MeV protons are produced by the Linac2 and are accelerated sequentially via the PSB, PS and SPS before final injection and acceleration in the LHC main ring

protons travelling around the tunnel (of approximately 4.5 km radius). To achieve a maximum proton beam energy of 7 TeV, and hence a maximum centre of mass energy for a symmetrical collider of 14 TeV, 1232 superconducting dipoles producing a field of 8.4 T are required, the most powerful ever made. For the LHC special two-in-one magnets have been developed which allow the two beams of protons, in

separate beam pipes, to be dealt with by one unit [22]. In the design, there are two magnet windings, one for each beam pipe, but there is a common support and yoke, and the whole ensemble is housed in a single cryostat. The magnets are cooled to 1.9 K using superfluid helium and the superconductor used is NbTi. Fig. 2.2 shows a cross section through one of the main accelerator dipoles. Manufacturing the magnets in this way was cheaper than producing separate items for each beam and also took up less space in the machine tunnel previously occupied by the single beam pipe of LEP.

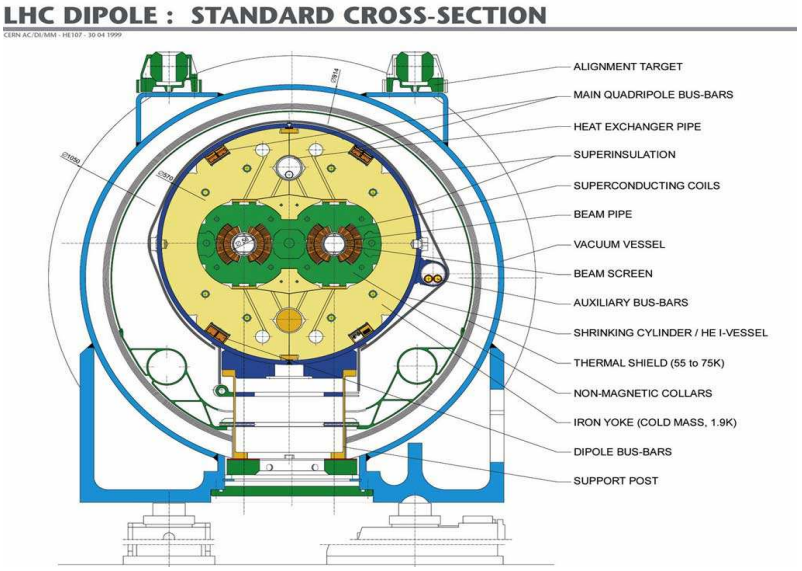

Figure 2.2: Cross section through one of the LHC main dipole magnets [23]

In addition to the accelerator magnets, there are a number of others which add up to more than 1700 overall. Most notable of these are the eight sets of focusing magnets located in pairs either side of the four LHC collision points.

In general the LHC is described as a ring, however in practice it is comprised of eight curved sections and eight straight sections. The eight LHC points are situated

on the straight sections, which are each 528 m long, with their locations as shown in Fig. 2.3.

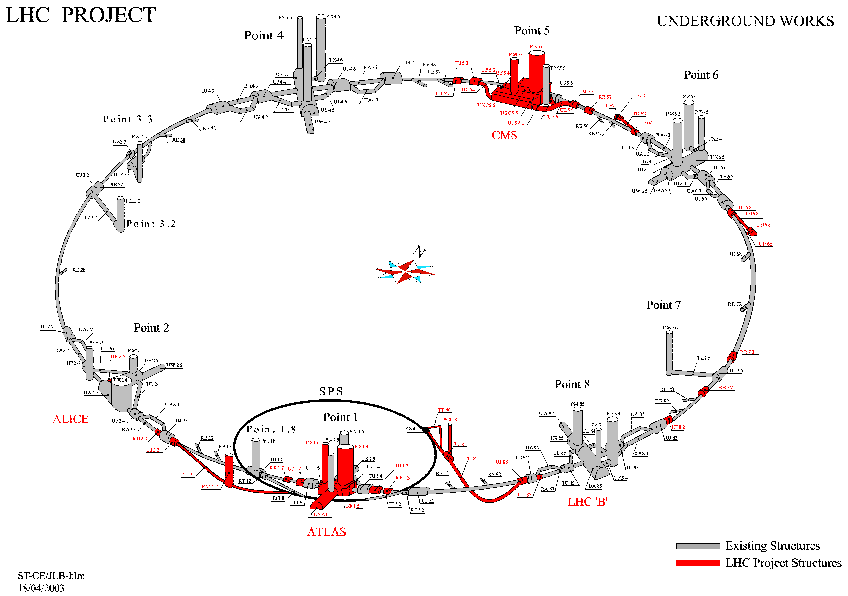

Figure 2.3: Illustration of the eight LHC sectors and the locations of the four major LHC experiments

Four of the eight points (1, 2, 5 and 8) house the LHC experiments as discussed later and are the only places where collisions take place. In addition to being experimental areas, points 2 and 8 are also where the two beams enter the LHC from the SPS. At points 3 and 7 are located beam cleaning magnets to keep the two LHC beams collimated. Point 4 is where the LHC RF (radio frequency) beam control system is found, which has been covered in detail elsewhere [24]. Finally point 6 (the former location of the LEP OPAL detector) is the site of the beam dump, where the beams can be removed from the LHC ring and disposed of in a controlled way via a combination of 'kicker' and septum magnets [20].

2.2.2 The LHC detectors

The LHC has four principal experiments situated around the accelerator ring. These are ALICE [25], ATLAS [26], CMS [27] and LHCb [28] and their relative underground locations are illustrated by Fig.2.3. In addition there are two further experiments called TOTEM [29] and LHCf [30].

ATLAS (A Toroidal LHC ApparatuS) and CMS (Compact Muon Solenoid) are situated at points 1 and 5 on the LHC ring respectively. Housed in caverns built from scratch for the LHC they are the largest particle physics collider detectors ever built; ATLAS is the largest with respect to volume and CMS with respect to mass. Both are general purpose detectors intended to look at all aspects of LHC physics [31] with a bias towards pp running but also some ability to study Pb-Pb collisions. ALICE (A Large Ion Collider Experiment) is located at point 2 in the pit which formerly contained the LEP L3 experiment. The magnet from this experiment is also used as part of the ALICE detector, which has been designed to study the heavy ion physics of the Pb-Pb LHC runs. The last of the big four experiments, LHCb (Large Hadron Collider beauty experiment) will continue the work of the B-factories by examining various aspects of flavour physics, notably the measurement of CP violation in B-meson decays. It is sited at LHC point 8 and uses the pit which previously held the DELPHI detector. TOTEM is primarily designed to measure the total LHC pp cross-section in a way that does not depend on the luminosity and consists of detectors placed each end of CMS at LHC point 5. Finally, LHCf (Large Hadron Collider forward) is intended to look at the forward region of LHC collisions

(very close to the beam pipe) and is located either side of the ATLAS detector.

2.3 The ATLAS Physics Programme

The ATLAS physics programme has an extremely broad coverage by virtue of being one of the two LHC general purpose detectors. This is covered in detail by volume II of the ATLAS Detector and Physics Performance Technical Design Report (TDR) [32] and also in the more recent studies covered in [33]. In summary, the main physics aims of the ATLAS experiment can be stated as follows:

- Look for the presence of the standard model or other possible Higgs bosons (such as the MSSM Higgs) in the region between the existing LEP and TeVatron mass limits and the theroretical mass constraint of approximately 1 TeV.

- Carry out searches for supersymmetric (SUSY) particles or other alternative new physics outside the current Standard Model. It is expected that particle searches will be possible up to around 5 TeV over the lifetime of the experiment (limited by the momentum fraction carried by the quarks and glouns which make up the proton).

- Make precision measurements of the top quark including its mass, decays and couplings. Studies will cover both $t\bar{t}$ and single top quark production scenarios. In addition it will be possible to look for the presence of any additional generations of heavy quarks (requiring associated heavy neutrinos; studies at

LEP and SLAC have produced results consistent with there only being three generations of light neutrinos).

- The electroweak gauge bosons can be examined to produce new precision measurements of the W boson mass, $W\gamma$ and WZ production and their associated Triple Gauge Couplings (TGC).

- A whole array of QCD processes will be studied and precision measurements made. This will provide both a test of QCD itself, and also allow the background to other Standard Model (or otherwise) LHC processes to be better understood.

- There will be a comprehensive B-physics programme to complement that of LHCb. This will include work on B_s^0 oscillations, CP-violation and measurement of B hadrons including their decays.

- Search for any additional new physics outside the Standard Model (including the existence of possible new gauge bosons, either charged or neutral).

The ATLAS detector has been designed to perform well with respect to all these physics areas, in addition to being able to operate successfully in the high luminosity environment of the LHC, which is required to study them. To do this ATLAS must:

- Have a high radiation resistance and a high detector granularity, coupled to fast readout electronics, to handle the LHC collision rate.

- Be able to work to high values of pseudorapidity (η) and cover the maximum possible region of azimuthal angle (ϕ). See 2.4.1.

- Possess excellent ability to identify, resolve and reconstruct charged particles, plus recognise the presence of secondary vertices (tracking detectors)

- Have electromagnetic calorimetry which allows for good photon and electron identification and which combined with comprehensive hadronic calorimetry will allow suitable measurements to be made of transverse jets energies and the accurate inferring of any missing transverse energy associated with neutrinos.

- Identify muons, including the charge of those possessing high transverse momentum (p_{T}).

- Be able to trigger on interesting LHC physics processes, including those which may produce low p_{T} particles, while still rejecting enough background so as to keep the data rate for final processing and storage within the desired limits.

ATLAS is described in section 2.4.

2.4 ATLAS detector

It is intended to give a general overview of the ATLAS (A Toroidal LHC ApparatuS) detector, illustrated in Fig.2.4. Further details can be found in the ATLAS Technical Proposal [34] and the ATLAS Detector and Physics Performance TDR volume I [35],

or alternatively through the specific TDR's corresponding to the various detector components. To account for specificication changes made during construction, updated information on the key components is contained within the ATLAS Detector Paper [26].

2.4.1 Detector Overview

As stated previously, ATLAS has been designed to analyse the physics of the LHC (primarily) pp collisions. Because the LHC beams are symmetric, a cylindrical geometry was chosen for the detector so as to allow the maximum spatial coverage of the particles produced in each collision. Furthermore, as a general purpose detector, it is important that ATLAS is able to measure the properties of all the particles produced in each event. To do this ATLAS uses a series of different detector layers arranged radially around the beam pipe.

Different types of particles can be identified by the way they behave in the various layers. Tracking chambers are usually housed within a magnetic field (this is true for all the ATLAS trackers) which allows the sign of charged particles to be identified by observing the direction in which they are bent by the field. The momentum component perpendicular to the field can also be determined for charged particles from the radius of curvature of their tracks. Energy possessed by electrons and photons is measured by an electromagnetic calorimeter, while a hadronic calorimeter when combined with the electromagnetic calorimeter provides the energy and position of hadrons and jets. In addition, the two calorimeters provide information on whether

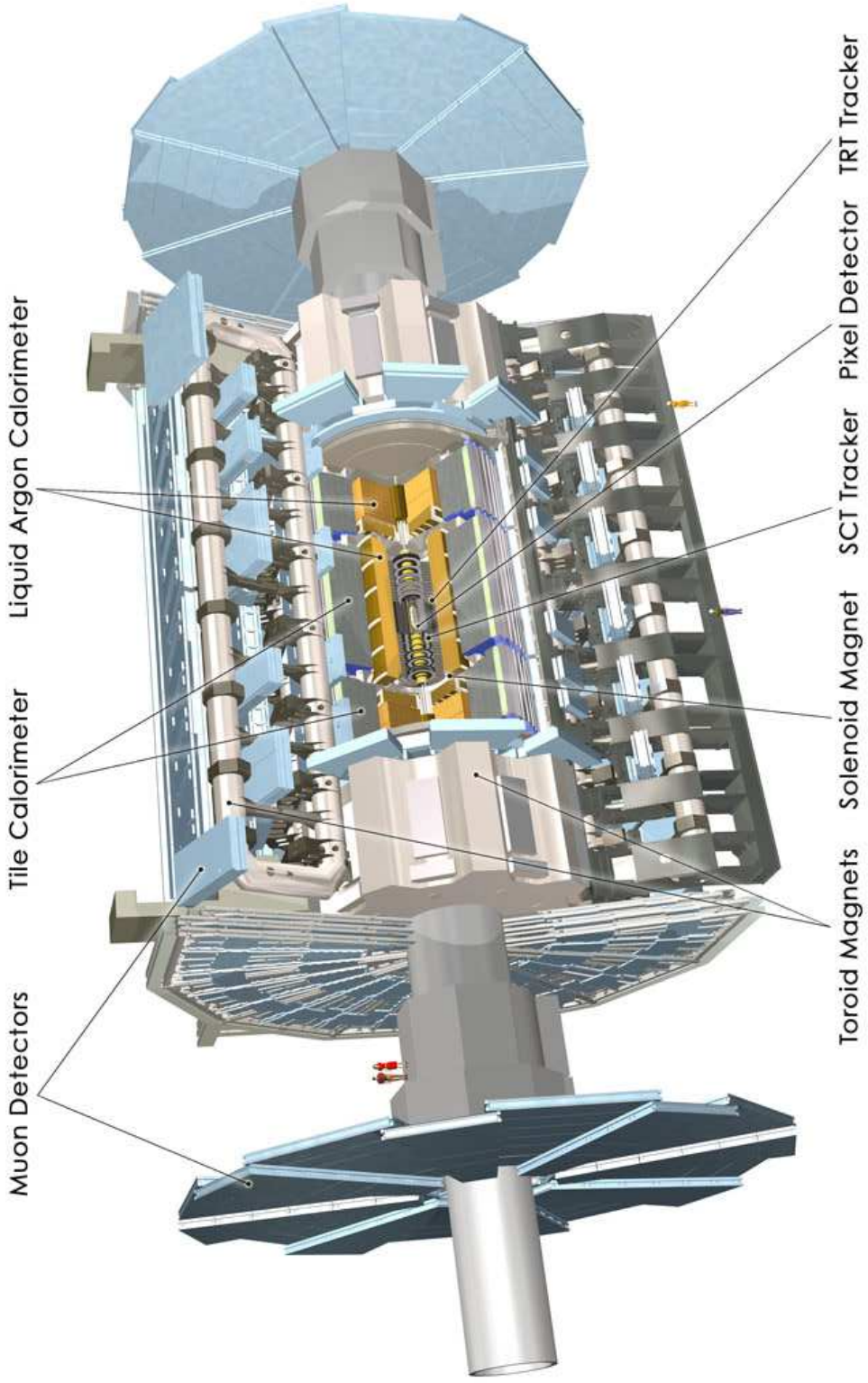

Figure 2.4: The ATLAS Detector [26]

any neutrinos or other weakly-interacting particles were present in an event. This is done by studying whether the total vector sum of the transverse momentum comes to zero, (as it would be before a collision took place) hence conserving momentum, or not. If transverse momentum, usually refered to as transverse energy (E_{T}), is not conserved and some is seen to be 'missing' from the calculation, then this imbalance is assumed to be due to the presence of one or more undetected weakly interacting particles (such as neutrinos). Conservation of total energy cannot be used as gaps are required in the detector for the beam pipe and so it is not possible to produce an accurate measure of the total longitudinal energy in an event (some of the particles will pass through the gap in the detector if they are produced very close to the beam pipe). Finally, the muon system (also housed in a magnetic field) provides explicit muon identification and together with the tracker gives an enhanced measure of muon momentum. Fig. 2.5 provides a schematic illustration of how these layers work together to allow the identification of different particle types.

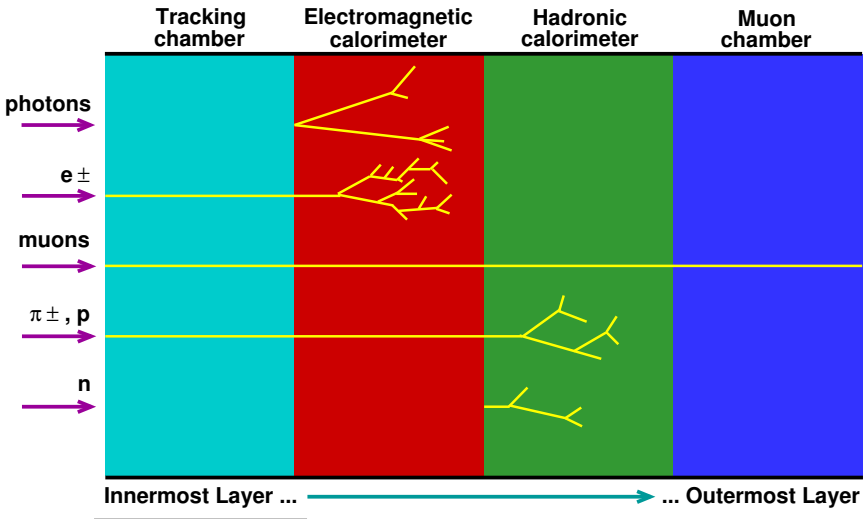

Figure 2.5: Schematic illustration of a slice through a general particle detector

ATLAS measures 46 m in length (parallel to the beam pipe), is 22 m in diameter and weighs 7000 t. Located in the UX15 pit at point 1 of the LHC, the z-axis is taken as being parallel to the beam pipe and defines the positive direction as towards point 8. The x-y plane is defined as being perpendicular to the beam pipe, with the origin at the collision point in the centre of the detector. As a right handed co-ordinate system, the positive x-direction points towards the centre of the LHC ring and the positive y-direction points vertically upwards. In polar co-ordinates, θ is the angle from the beam pipe and ϕ the angle around it. The pseudorapidity (η) is defined in the usual way [1] [35]. The physical body of the detector can be divided into three main parts; the inner detector, the calorimeters and the muon spectrometer. These are discussed here with specific values taken from [26]. In addition there are also trigger and data aquisition (TDAQ) which will be discussed separately in chapter 3.

2.4.2 Inner Detector

The inner detector consists of a series of different tracking devices mounted inside a solenoid magnet 5.3 m in length and of 2.46 m inner diameter [26]. This magnet has been engineered to produce a 2 T nominal field (2.6 T peak field) and has

[1] The pseudorapidity is defined in terms of the angle θ by $\eta = -\ln \tan(\frac{\theta}{2})$ and for particles travelling close to the speed of light is approximately equal to the particle rapidity (defined in terms of the particle's energy and momentum in the direction along the beam axis). Pseudorapidity is used to define the position of particles in the detector instead of the angle θ because the separation of particles in η does not depend on the lorentz boost of the particles along the beam axis. This is not true for θ.

also had to be designed so as to minimise the interference produced to particles travelling through the solenoid and into the surrounding calorimeters. This requires the amount of material between the tracking detectors and the calorimeters to be as small as possible. The solenoid shares a vacuum chamber with the liquid argon (LAr) calorimeter barrel for this reason. As the solenoid produces a magnetic field parallel to the beam pipe, charged particles are bent in a plane perpendicular to this. The inner detector itself is 5.5 m long and 2.5 m in diameter and is divided into a central barrel region 1.6 m long and two matching endcaps [35]. The barrel consists of a series of cylinders, each consisting of a layer of detectors, wrapped around the beam pipe (of 36 mm radius). For the endcaps a series of circular disks are used perpendicular to the beam, with the detectors arranged radially. Both the barrel and the endcaps contain layers of both silicon and gas filled straw tube detectors. Fig. 2.6 shows a cut-away view of the complete inner detector, minus the surrounding solenoid.

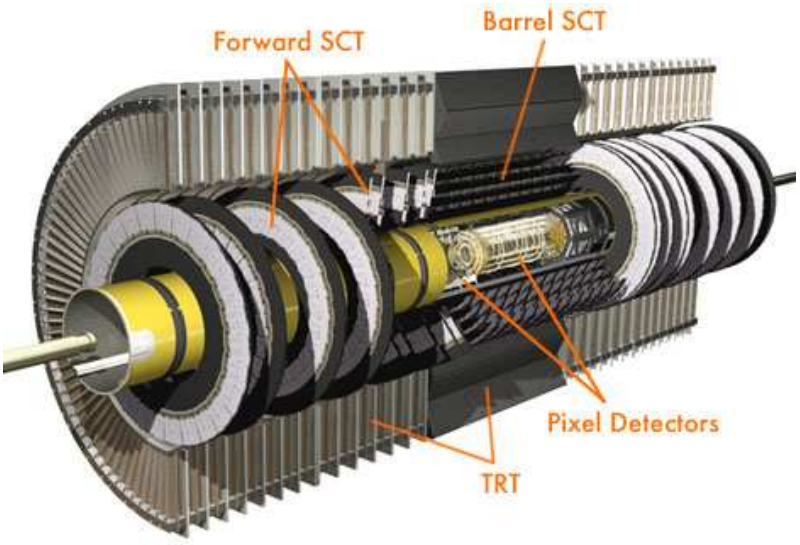

Figure 2.6: Cut-away view of the ATLAS inner detector (central solenoid not shown) [26]

Three different types of tracking detectors are used in the tracking region. These are silicon pixel detectors, silicon strip detectors and Transition Radiation Trackers (TRT) in order of decreasing granularity.

Pixel Detectors

The pixel detectors have the finest granularity of the tracking detectors, each measuring a minimum of 50×400 μm. In the barrel region, pixels are arranged in three layers between radii of 50.5 mm and 122.5 mm (0 is defined as being at the centre of the beam pipe) and over a length of 802 mm. Each end cap has three disks of pixels at radii from 89 mm to 150 mm. The two pixel endcaps are found between 495 mm and 650 mm from the collision point at either end of the barrel [26]. In total there are approximately 140 million pixels.

Strip Detectors (SCT)

Found outside the pixels, the silicon strip detectors are approximately 12 cm long by 80 μm wide. The barrel has four layers situated between 299 mm and 514 mm radius and over a length of 1492 mm. Each end cap has 9 disks of between 270 mm and 560 mm radius and these are situated between 847.5 mm and 2727 mm from the collision point in each case [26]. Each layer consists of two strip sets, with an angle of 2.3 degrees between each set. The stereo angle provides a measurement of z (and thus a value of η) in the barrel, whilst providing a measurement of the radial distance r in the endcaps. Barrel strips are parallel to the beam pipe and endcap

strips arranged radially.

Transition Radiation Tracker (TRT)

TRT are used for the outer layers of the tracking region. Each TRT sensor consists of a 4 mm diameter tube with a thin wire running down the centre, filled with a gas mixture (mainly xenon). The barrel straws are 1.44 m long and the end cap straws 0.37 m long [26]. A large potential difference is maintained between the metal tube walls and the wire so that when a particle passes through a tube, an output signal is produced which also gives how far from the wire the particle passed (by use of timing) as well as which tubes were traversed. Although the measurement for a single tube is not as accurate as that for a single pixel or strip detector, this can be countered by using many more layers. The TRT barrel has 73 planes of straws set at radii between 559 mm and 1080 mm over a length of 1430 mm. The end caps have 160 straw planes at radii between 635 mm and 999 mm and in each case between 847.5 mm and 2727 mm from the collision point [26].

In general, the combined tracking region covered by the pixels, SCT and TRT is $|\eta| < 2.5$.

2.4.3 Calorimetry

ATLAS uses a combination of liquid argon (LAr) and tile scintillator calorimeters. Electromagnetic (EM) calorimetery is provided via a barrel (actually made of two

jointed half barrels with a 6 mm gap at the collision point, z = 0) covering $|\eta| <$ 1.475 and two endcaps covering 1.375$< |\eta| <$3.2 [26]. All use LAr technology. There is also a LAr presampler at $|\eta| < 1.8$. Hadronic calorimetery is performed up to $|\eta| < 4.9$ courtesy of a tile scintillator barrel ($|\eta| < 1.0$) and extended barrel (0.8$< |\eta| <$1.7), LAr hadronic endcaps (HEC) for 1.5$< |\eta| <$3.2 and finally a LAr forward calorimeter (FCal) for 3.1$< |\eta| <$4.9. The complete ATLAS calorimeter system is shown in Fig. 2.7.

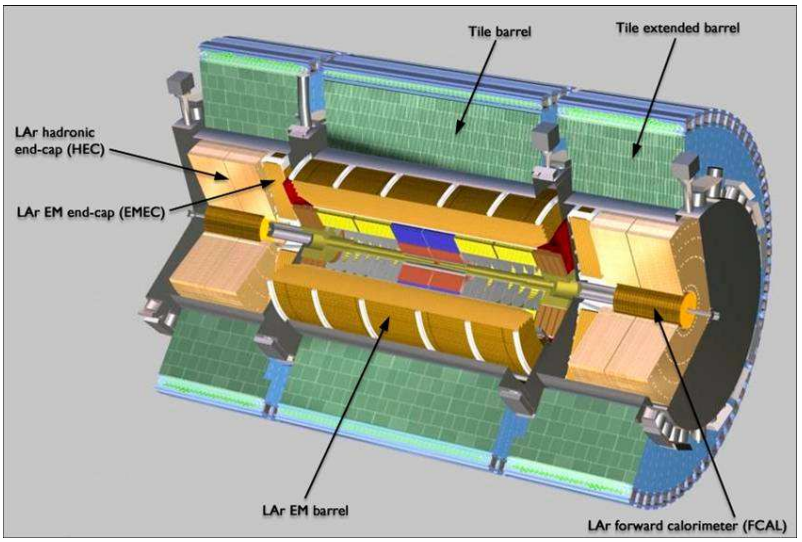

Figure 2.7: Cut-away view showing the complete ATLAS calorimeter [26]

Electromagnetic Calorimeter

Both the EM calorimeter barrels and endcaps use a sampling calorimeter consisting of layers of lead absorber immersed in LAr to provide the active medium. The lead absorbers used take an 'accordion' shape, intended to give complete, symmetrical, coverage with respect to ϕ without the presence of any gaps.

The barrel assembly is taken to constitute the two main LAr half barrels and also the presamplers. As stated in section 2.4.2 the LAr barrel assembly shares a cryostat with the inner solenoid magnet. This is made from aluminium and insulated via a vacuum layer. The total length of the cryostat (when the two halves are joined together) is 6.8 m and the inner and outer radii are 1.15 mm and 2.25 m respectively [36]. For each EM calorimeter half barrel there are 1024 of the lead accordion absorbers [26]. The thickness of the lead ranges from 1.53 mm to 2.2 mm on going from zero to 3.2 in pseudorapidity (η); see [36]. To give structural rigidity, the lead layers are actually trapped between two sheets of stainless steel 0.2 mm thick. Lead absorbers, approximately 4 mm apart, alternate with Kapton electrodes required to read out the calorimeter signals. Presamplers are present in front of the calorimeter and inside the barrel cryostat in the form of a 1 cm layer of LAr [26], which is read out by electrodes perpendicular to the beam pipe. In general the barrel is divided into three sampling layers along its length, while being divided into 32 sectors in ϕ to be read out by 7808 channels. There are approximately 110000 channels overall.

A section of the EM calorimeter barrel can be seen in Fig. 2.8, indicating the three sampling layers. The radiation lengths of the samplings are marked while the accordion shape of the absorbers is also illustrated. For the barrel, the overall material thickness is > 24 radiation lengths. The finest granularity in the barrel is provided by the strip layer of the first sampling, so called because of the cell shapes in this region, which is used to help identify the direction and width of showers (particularly those produced by photons).

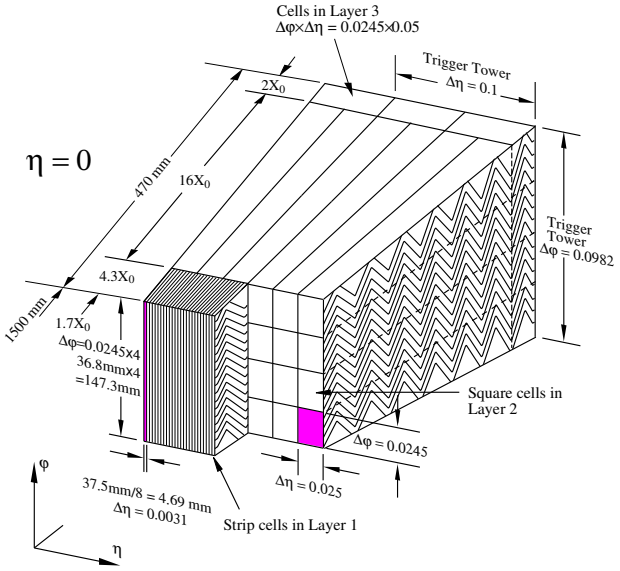

Figure 2.8: A section of the ATLAS EM calorimeter barrel. The three depth samplings can be seen, together with the accordion shape of the electrodes and the difference in granularity in the three layers [26]

For each EM calorimeter endcap, eight wedge-shaped units are used to produce a wheel of 2098 mm radius and 632 mm thickness. Each of these endcap wheels actually consist of an inner wheel (256 absorber plates) and an outer wheel (768 absorber plates) to cover 2.5-3.2 and 1.375-2.5 in η respectively [26]. The absorber plates are arranged radially, and are divided into two samplings longitudinally. In each endcap there is a 5 mm layer of LAr to act as the presampler which is read out by electrodes parallel to the beam pipe. The endcaps have approximately 64000 read out channels. Each aluminium end cap cryostat has an outer radius (warm skin) of 2.25 m and a length of 3.17 m. In the endcaps the material thickness is $>$ 24 radiation lengths except for values of $|\eta|$ $<$1.475 [26].

Athough both the barrel and endcaps use lead-LAr calorimeters, a large gap is

present in coverage at approximately $|\eta| = 1.4$ where they meet. To try and reduce the effect of this for jets, photons and electrons, a slab of scintillating plastic is positioned in this region. Fig. 2.9 shows a cut-away view of one half of the complete EM calorimeter system (the hadronic and forward LAr endcaps are also shown but the gap scintillator is not).

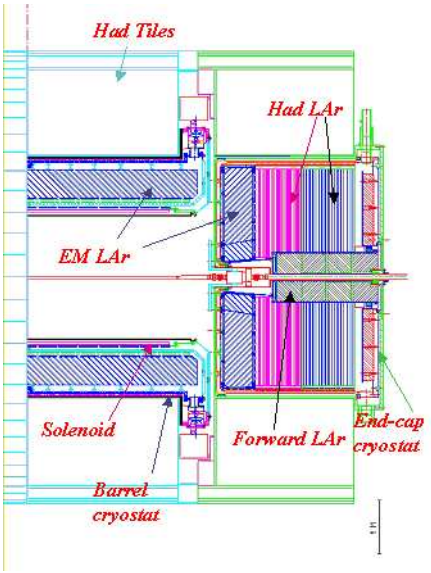

Figure 2.9: Cut-away view showing one half of the ATLAS EM calorimeter (together with complete endcap)

For both the barrel and endcap the number of calorimeter layers and the granularity vary as a function of η. Table 2.1 summarises this information for the complete EM calorimeter [26].

Hadronic Calorimeter

The hadronic calorimeter barrel and extended barrel consists of a tile sampling calorimeter. The central barrel wraps around the EM calorimeter barrel and has

EM Calorimeter	Barrel		Endcap	
Number of layers and $\|\eta\|$ coverage				
Presampler	1	$\|\eta\|<1.52$	1	$1.5<\|\eta\|<1.8$
Calorimeter	3	$\|\eta\|<1.35$	2	$1.375<\|\eta\|<1.5$
	2	$1.35<\|\eta\|<1.475$	3	$1.5<\|\eta\|<2.5$
			2	$2.5<\|\eta\|<3.2$
Granularity $\triangle\eta \times \triangle\phi$ versus $\|\eta\|$				
Presampler	0.025×0.1	$\|\eta\|<1.52$	0.025×0.1	$1.5<\|\eta\|<1.8$
Calorimeter 1st layer	$0.025/8\times0.1$	$\|\eta\|<1.40$	0.050×0.1	$1.375<\|\eta\|<1.425$
	0.025×0.025	$1.40<\|\eta\|<1.475$	0.025×0.1	$1.425<\|\eta\|<1.5$
			$0.025/8\times0.1$	$1.5<\|\eta\|<1.8$
			$0.025/6\times0.1$	$1.8<\|\eta\|<2.0$
			$0.025/4\times0.1$	$2.0<\|\eta\|<2.4$
			0.025×0.1	$2.4<\|\eta\|<2.5$
			0.1×0.1	$2.5<\|\eta\|<3.2$
Calorimeter 2nd layer	0.025×0.025	$\|\eta\|<1.40$	0.050×0.025	$1.375<\|\eta\|<1.425$
	0.075×0.025	$1.40<\|\eta\|<1.475$	0.025×0.025	$1.425<\|\eta\|<2.5$
			0.1×0.1	$2.5<\|\eta\|<3.2$
Calorimeter 3rd layer	0.050×0.025	$\|\eta\|<1.35$	0.050×0.025	$1.5<\|\eta\|<2.5$

Table 2.1: Coverage and granularity of the ATLAS EM calorimeter [26]

an inner radius of 2.28 m. The outer radius is 4.25 m and the central section is 5.8 m long, with each of the two extended barrels being 2.6 m in length [26]. Each tile consists of a steel absorber and a plastic scintillator active medium 3 mm thick. Layers of tiles are arranged in planes parallel to the beam direction and these are staggered over depth, making them periodic in z. Wavelength shifting fibres are used to take the light from both sides of the scintillator for each tile and, running radially, transfer it to a photomultiplier tube to be read out. By grouping fibres together it is possible to produce a three dimensional output.

Like the EM calorimeter barrel, the central barrel section is also divided into three radial layers which provide the three samplings. At $\eta = 0$ these layers are designed to be at radii which give them thicknesses of 1.5, 4.1 and 1.8 interaction lengths respectively [26]. The overall 'thickness' of material found inside the ATLAS muon system (comprising the inner detector and solenoid/cryostat, electromagnetic calorimeter, hadronic calorimeter and their associated support systems) in total at $\eta = 0$ is 11 interaction lengths. This enables hadronic showers/jets to be confined within the hadronic calorimeter and hence restricts passage of particles other than muons (or neutrinos) out into the surrounding muon spectrometer [37]. Similarly the two extended barrels, intended to study the $|\eta|$ region between 0.8 and 1.7, are also divided into the same three samplings as the central barrel. Both the central and extended barrels are divided into 64 sectors with respect to ϕ, as shown in Fig. 2.10. This produces an overall granularity of 0.1×0.1 in $\Delta\eta \times \Delta\phi$ except for in the last radial layer where it is 0.2×0.1 [38].

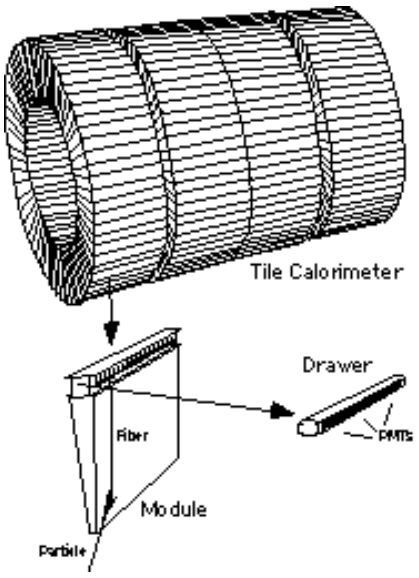

Figure 2.10: Schematic representation of the hadronic tile calorimeter assembly, with a single module shown for comparison

The two hadronic end-cap calorimeters (HEC's) use LAr technology similar to the EM calorimeters, but with a different metal absorber. Intended to cover an $|\eta|$ range between 1.5 and 3.2, each end-cap has two wheels of 2.03 m external radius [26]. Both use copper plates as the absorber and LAr as the active medium, with the inner wheel using 25 mm thick plates and the outer 50 mm thick plates [26]. read out is provided via the central one of three electrodes found between each set of plates, which are spaced 8.5 mm apart. A total of 5632 read out channels are present [26]. Both wheels are constructed from 32 units and split into two samplings. The wheels, which share the end-cap cryostat with the EM calorimeter end-cap and the forward calorimeter, weigh approximately 67 and 90 tonnes respectively.

Two forward calorimeter (FCal) end-caps, each comprising three module units, are designed to provide calorimetry in the region $3.1 < |\eta| < 4.9$ [26], overlapping slightly

with the hadronic end-cap calorimeters. The FCal uses a metal matrix and LAr design, which uses metal rods centred inside metal tubes mounted between two metal tubeplates. The gaps between the rods and the tubes are filled with the LAr active medium. Of the three units which make up each FCal, the innermost uses copper as the metal and contains 12000 tubes and rods, each rod being 4.75 mm in diameter and the gap between the rod and tube being 0.25 mm [36]. For the remaining two units, tungsten metal is used. The inner unit has 10000 rods and tubes with a rod diameter of 4.75 mm and a gap of 0.375 mm, while the outer unit has 8000 elements, each rod being 5.5 mm in diameter and the LAr gap being 0.5 mm. Both FCals are read out by 11288 channels. The design of the FCal was formulated largely to try to limit the damage produced by the high particle flux that will be present in the FCal region. For this reason, a copper 'plug' is also located behind each of the FCals to attempt to protect the forward muon chambers of the detector. Fig. 2.11 illustrated the general layout of the FCal.

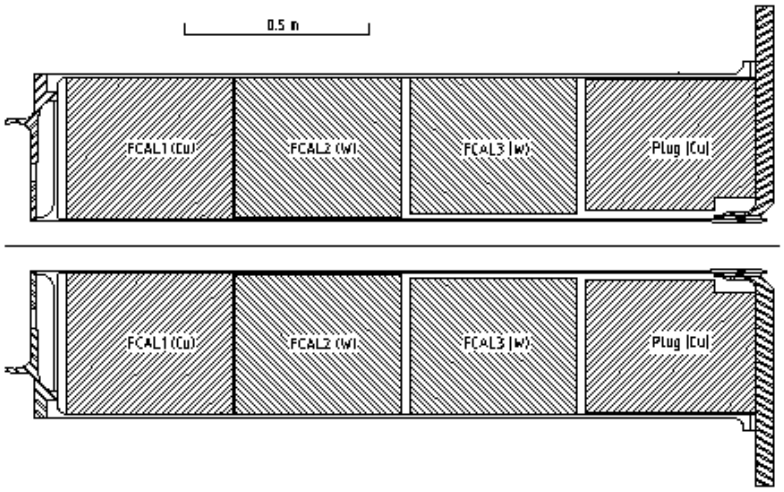

Figure 2.11: General arrangement of the LAr forward calorimeter

2.4.4 Muon Spectrometer

The muon spectrometer is what defines the overall size of the ATLAS detector. It consists of three superconducting air-cooled toroid magnet systems, one barrel and two endcaps. These magnets are used to bend the path travelled by muons, which is recorded by a series of tracking chambers in both the barrel and endcap regions, as per the inner detector.

All three of the toroid magnets use eight coils arranged around the beam axis. In the barrel, each coil that makes up the toroid is approximately 25 m long, 5 m wide and weighs 40 tonnes. They are comprised of two double-pancake windings of 20.5 kA NbTi superconducting wire, stabilised using aluminium [35], and are contained inside an alloy outer shell. In addition, all the barrel coils have individual cryostats to provide the cooling, weighing 40 tonnes each, which are used as part of the structural support for the whole toroid, together with additional alloy struts. The eight coils are linked together and mounted on the detector feet as shown in Fig. 2.12 to produce a toroid with inner and outer diameters of 9.4 m and 20.1 m respectively [26]. The barrel toroid produces a peak field of 3.9 T and in the region for $|\eta|$ of 0.0-1.4 the bending power produced is from 2 to 6 Tm.

The two end-cap toroid magnets use the same coil winding type as for the barrel, with each of the eight coils per endcap measuring approximately 4.5 $\times$ 4 m and weighing 13 tonnes. The smaller size means that for each end-cap the eight coils are mounted into one single structure housed in a single cryostat. Each assembled magnet has an inner diameter of 1.65 m and an outer diameter of 10.7 m [26];

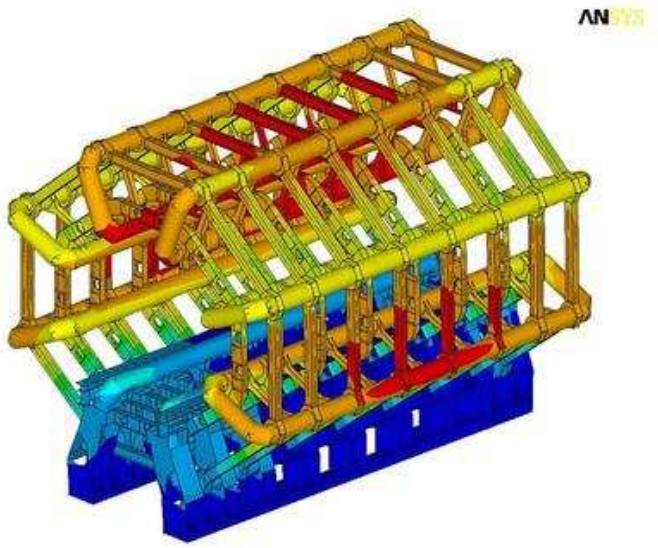

Figure 2.12: Illustration of how the eight coils of the ATLAS barrel toroid magnet are linked together and mounted on the detector feet

the complete assembly including the cryostat is approximately 5 m long, 11 m in diameter and weighs roughly 240 tonnes. A complete endcap unit is illustrated in Fig 2.13. The peak field for each end-cap toroid magnet is 4.1 T and the resultant bending power is 1 to 8 Tm for $|\eta|$ from 1.6 to 2.7. Each end-cap toroid is mounted within the relevant end of the main barrel toroid. To permit this and to maximise the bending power possible in the region $1.4 < |\eta| < 1.6$ where overlap of the two sets of fields occurs, the coils of the barrel and end-cap are offset relative to each other by 22.5° in ϕ. Despite this, the bending power is still reduced in this region.

Measurement of muons in the spectrometer is carried out using four different types of tracking detectors. As with the other detector components, these are arranged into a barrel region and two sets of big wheel end-caps. The barrel provides coverage for $|\eta| < 1$ and comprises three layers of chambers, wrapped around the beam pipe,

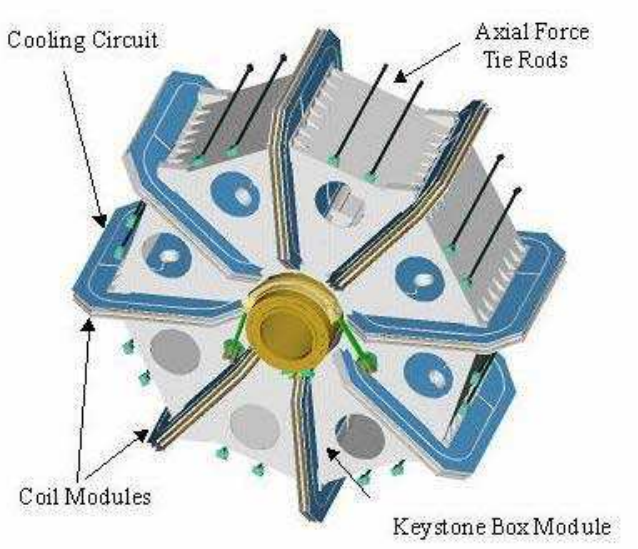

Figure 2.13: View of one of the ATLAS end-cap toroid magnets

at 5, 7.5 and 10 m radius [26]. End-cap coverage is for 1.0< $|\eta|$ <2.7, with each end-cap having four big wheels of radially arranged chambers located perpendicular to the beam pipe at distances of 7.4 m, 10.8 m, 14 and 21-23 m from the collision point at the centre of the detector [26]. The spacing of the layers of muon chambers is shown in Fig. 2.14

Precision position measurement of the muon primary coordinates (in the main magnet bending plane) is mainly provided by 11088 Monitored Drift Tubes (MDTs) for $|\eta|$ <2.7, with 32 Cathode Strip Chambers (CSCs) replacing the inner endcap layer of MDTs for 2.0< $|\eta|$ <2.7 [26]. These are read out by 339000 and 30700 channels respectively [26]. Measurement of the secondary muon coordinate (in the non-bending plane and perpendicular to the primary) and also triggering is provided via 544 Resistive Plate Chambers (RPCs) for $|\eta|$ <1.05 and 3588 ThinGap Chambers (TGCs) for 1.05< $|\eta|$ <2.4 [26]. Triggering is not provided for $|\eta|$ >2.4. These

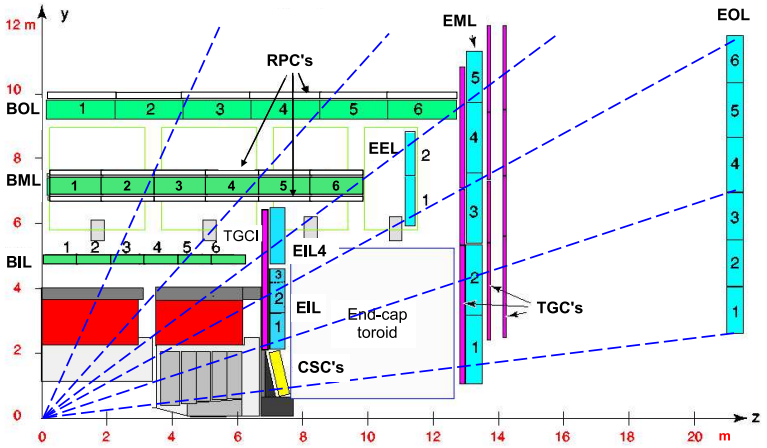

Figure 2.14: Section throught the side of the ATLAS detector illustrating the arrangement of the muon chambers [26]

chambers are read out by 359000 channels for the RPCs and 318000 channels for the TGCs [26]. The location of the different chamber types is summarised in Fig. 2.15.

2.5 ATLAS analysis tools

Within the ATLAS experiment a standard framework exists for use in all ATLAS physics analysis. This Athena framework is primarily designed to carry out analysis on Analysis Object Data (AOD) files which are the format in which the majority of the real data from the running ATLAS experiment are stored. Athena uses algorithms written in C++, controlled by job option files written in python, to carry out the desired analyses.

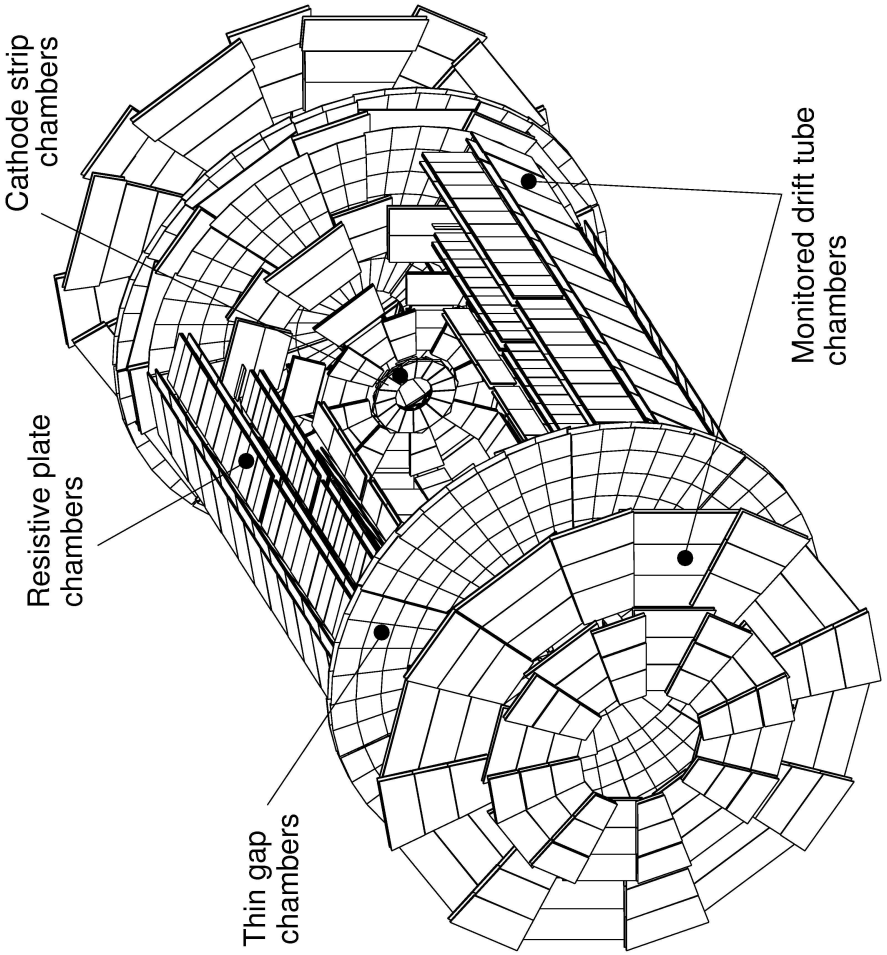

Figure 2.15: Location of the different chamber types within the muon spectrometer

To compare the real ATLAS data to theory and to evaluate different analysis strategies, it is necessary to produce artificially sets of AOD files for a whole series of different processes. These 'Monte Carlo' datasets are produced by a process referred to as running the ATLAS full chain, illustrated in Fig. 2.16.

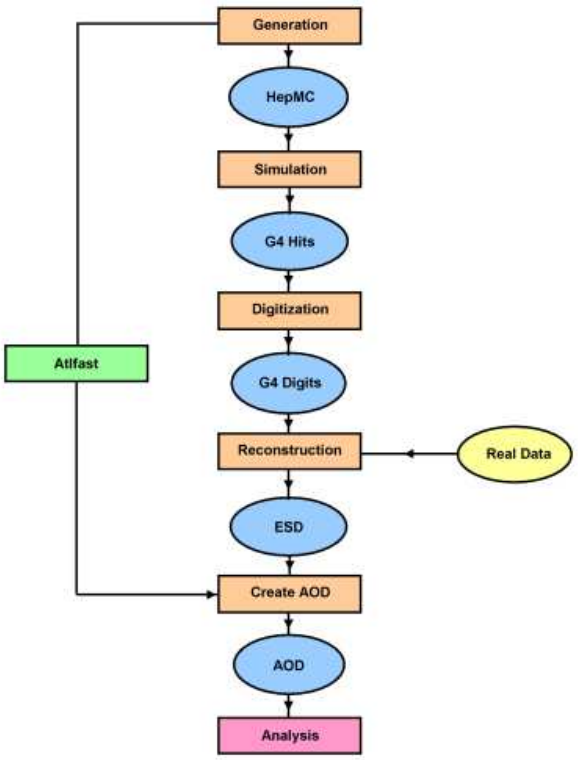

Figure 2.16: Flow diagram showing the stages required to produce artificially ATLAS AOD datasets

Events are produced by an ATLAS approved generator [2], such as MC@NLO [39], Pythia [40] or Herwig [41], and passed through a full simulation of the ATLAS de-

[2] An event generator simulates the various stages of a particle collision. It reproduces the initial state and any associated radiation, the hard scatter, and the production and then subsequent decay of particles in a given physics process. Final state showering and radiation are also produced. Generators can be tuned depending on the particular process and conditions being studied

tector provided by GEANT4 [42]. Simulated detector hits (recording which sensors within ATLAS fired for a given event, together with the size of the recorded signals) are converted into raw data objects (RDO) by the digitization stage. For real ATLAS data the raw output of the readout ('bytestream') is unpacked into RDO format as the first stage of the reconstruction. The same process is now followed for simulated and real ATLAS data. RDO undergo an event reconstruction stage to produce Event Summary Data (ESD) files, which are a detailed output format. These are then condensed to produce finally the AOD files for analysis. AOD consist of collections which contain the information relating to the different particle types; for example the electron collection contains information on the η, ϕ, p_{T} and so on of each electron recorded in the event, together with a summary of any quality cuts applied. In addition to the various reconstructed particle types, there are separate collections for jets, trigger information, truth information (for simulated data only) and selected information on tracks, calorimeter clusters and similar. Truth information contains the details about an event as produced by the generator before the detector simulation was applied.

2.6 Conclusions

An overview of the Large Hadron Collider at CERN has been presented. The main components of the accelerator complex have been briefly described, together with how they are used to produce proton-proton collisions at a given centre of mass energy. Figures were provided for the design beam parameters and also those used to

collect a total of 46 pb^{-1} of proton-proton collision data (for a centre of mass energy of 7 TeV) during 2010. The ATLAS experiment was introduced and the ATLAS physics programme was briefly covered, together with the resulting detector requirements. An overview was given of the complete ATLAS detector and how it is used to identify different experimental signatures. A detailed description was provided of the various ATLAS subdetectors, focusing in particular on the electromagnetic and hadronic calorimeters, while finally the ATLAS data format and analysis framework was summarised.

Chapter 3

The ATLAS Trigger System

3.1 Introduction

Within this chapter is provided an overview of the ATLAS trigger system. The three trigger levels are introduced and briefly described. Further detail is then provided on the first level calorimeter trigger, describing how regions of interest are formed and how the trigger menu thresholds are assigned.

3.2 ATLAS Trigger Overview

The ATLAS trigger system is designed to reduce the ATLAS data rate sufficiently that permanent storage is possible. In doing so, it must retain as far as is possible the maximum number of ATLAS events which are likely to yield new physics or are

required for detailed study, while at the same time discarding those events which are of minimal interest. When the LHC is running at the design luminosity of 10^{34} cm^{-2}s^{-1} the bunch crossing rate of 40 MHz produced will correspond to a pp interaction rate of approximately 1 GHz. This had to be reduced in the 2009-2010 running to just 200 Hz for storage on disk [43]. From 2011 storage of the complete ESD (see 2.5) was to be dropped for most events, allowing the final data rate to be raised to 400 Hz. The final rate is limited by the amount of data storage available, together with the time required to analyse the data fully. In general, this is mainly done by removal of the low p_{T} QCD events produced by soft pp collisions.

The ATLAS trigger uses three levels. Level 1 is hardware based and reduces the $\sim$1 GHz LHC interaction rate to 75 kHz. A maximum of 2.5 μs is available for the level 1 trigger decision, however a 2.2 μs latency is actually used for caution. The rate is then further reduced by the software based level 2 to $\sim$3.5 kHz, which takes approximately 40 ms (on average) [43]. Finally the Event Filter (EF) is applied to reduce the overall rate to a few hundred hertz ready for storage on hard disk. The difference between level 2 and the event filter is described in 3.3.2 and 3.3.3. Approximately 4 s is required for the Event Filter stage, which is able to use offline algorithms as part of the selection process. Level 2 and the Event Filter are jointly referred to as the higher level trigger (HLT). The three trigger levels are summarised in Fig. 3.1.

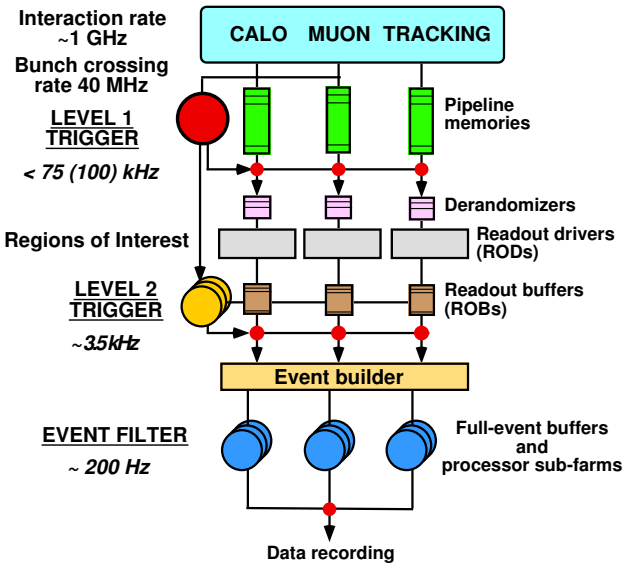

Figure 3.1: Overview of the ATLAS trigger system [43]

3.3 Trigger Performance

3.3.1 Level 1 Trigger

At level 1 (LVL1), the speed of response required means that the whole ATLAS detector is not read out. Instead, the LVL1 trigger decision is made by accessing only the calorimeters and muon detectors. In addition, the granularity used at LVL1 from these systems is coarser than what is actually possible for these two subsystems. For the calorimeters, reduced granularity is used in both the barrel and endcaps for both EM and hadronic parts. For the muon detectors, only the trigger RPCs and TGCs are used in the barrel and endcaps respectively (see sections 2.4.3 and 2.4.4 for details of the calorimeters and muon spectrometer). While the LVL1 decision is awaited, events are stored in the on detector pipeline memories. For those bunch crossings which pass LVL1 this is then read out from the detector and passed on

to storage in the readout buffers (ROBs). Events not selected are discarded and cannot be recovered. The Central Trigger Processor (CTP) is responsible for using the LVL1 muon and LVL1 calorimeter data to produce the decision, based upon a trigger menu of various different items [43]. LVL1 muon and calorimeter triggers together look for [44]:

- High p_{T} muons
- High p_{T} electrons and photons
- Jets and taus decaying to hadrons
- Large missing and total E_{T}

The LVL1 trigger has two main purposes. The first is to deduce whether a particular LHC bunch crossing is likely to contain an event which may be of interest for further study, and hence whether the corresponding information should be retained and passed to the level 2 (LVL2) trigger or not. Secondly, if an event is noted as being of interest at LVL1, the LVL1 trigger also produces Regions-of-Interest (RoI), in terms of η and ϕ coordinates, that mark the areas of the event which are of interest. It is these areas that are studied by LVL2 in order to make the LVL2 decision. Information on the trigger thresholds passed at LVL1 is also available.

3.3.2 Level 2 Trigger

At LVL2 the full granularity information is available for the calorimeters and muon chambers, plus the inner detector is also used, again at full granularity. However, the LVL2 trigger is only allowed to use data from the regions which have been marked by a LVL1 RoI. By restricting the fraction of the detector read out available to LVL2, the bandwidth and processing requirements needed are reduced. This is done by the LVL2 trigger using the RoI information as a guide, so as to look only at the specific parts of the data in the ROBs necessary to make the LVL2 decision. LVL1 produces two types of RoI, both of which can be studied by LVL2. Primary RoI are those produced by signatures within an event which were directly responsible for the event passing LVL1. Secondary RoI are produced for features of interest that were not directly responsible for the event selection (these are little used at present). By use of the RoI system, the amount of data which has to be processed at LVL2 before a decision is made is approximately 2% of the total readout [43], and as a result the trigger latency is reduced accordingly. Events which pass the LVL2 trigger condition are moved from the ROBs on to the Event Filter via the event building stage. Event building results in all the data for a particular event being stored as one item, rather than being split up as at earlier trigger stages. As for LVL1, events which are not selected by LVL2 are discarded completely.

3.3.3 Event Filter

The Event Filter (EF) uses sophisticated algorithms, of the type normally used for offline analysis, which have been adapted to work online and provide the final stage of event rejection. Use of conventional offline algorithms that have been packaged up to work online removes the need to develop software specifically tailored to the EF. Unlike LVL1 and LVL2, the EF has the ability to use all the data for each event which are received via the event builder. However, the EF algorithms are expected to be 'seeded' on what areas of the data to concentrate on by the results of LVL2. In order to realise the desired data rate of 200 Hz for hard disk storage, the EF is expected to [45]:

- Reject any remaining events which are not desired for physics analysis
- Minimise storage size (if possible) for events which pass the EF
- Apply some data compression

For initial ATLAS running, LVL2 and the EF were switched off. Here, events successfully selected by LVL1 effectively passed straight through the HLT and on to permanent disk storage. The HLT was enabled when necessary during 2010, with the selection applied depending on which signatures were needed and validated at a given time. The EF will play an increasingly important role as the LHC luminosity is ramped up.

3.3.4 Trigger Menus, Chains and Event Selection

The ATLAS trigger decision for a given event is made by referencing a set trigger menu stored in a database. The menu comprises a large number of items, each of which has a particular signature for the three trigger levels. Each item comprises a chain of signatures with the LVL2 signature building on from the LVL1 thresholds and likewise the EF signature refining that of LVL2. For a given event, the LVL1 trigger signatures are first checked for each chain. Should all chains fail at this stage then the event is immediately rejected. Otherwise, the remaining chains progress to LVL2 where the process is repeated. If any of the chains pass all three levels, then the event is accepted and written to storage on disk.

ATLAS trigger menus also allow for prescaling of the items. Prescales are factors which can be applied to a given trigger signature to ensure that only a predetermined fraction of the events that would otherwise have passed the signature can do so. As a consequence, they allow the trigger to select lower priority but still interesting physics events without compromising the overall trigger rate. All three levels of the trigger have the capability for prescaling and a given trigger chain can contain a mixture of prescaled and non-prescaled signatures.

3.4 Level 1 Calorimeter Trigger

3.4.1 Overview

As described in 3.3.1 the level 1 calorimeter (L1Calo) trigger uses a reduced granularity from the ATLAS calorimeters. This granularity varies depending on the trigger being considered.

3.4.2 Cluster Triggers

For electron/photon and tau/hadron cluster triggers, the granularity used is approximately 0.1×0.1 in $\triangle\eta \times \triangle\phi$ [1] and the calorimeter elements are arranged into approximately 7200 trigger towers [43], which split into electromagnetic (EM) trigger towers and hadronic trigger towers. L1Calo cluster triggers only cover $|\eta|$ <2.5, the region corresponding to inner tracker and high granularity calorimetry coverage [46]. The details of how the L1Calo electronics are arranged have been described in a number of sources, such as [26], and will not be discussed here. The trigger towers are grouped into EM and hadronic clusters, cores and isolation rings and are analysed by an algorithm which uses a sliding 4×4 trigger tower window as shown in Fig. 3.2 [46].

EM clusters are formed by summing pairs of adjacent trigger towers in the 2×2 EM core, in the centre of the algorithm window, over the depth of the EM calorime-

[1] Actual granularity used is $0.1 \times \frac{\pi}{32}$ in $\triangle\eta \times \triangle\phi$

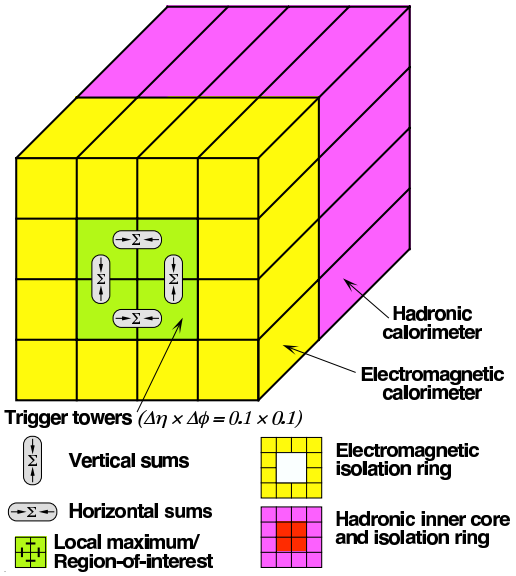

Figure 3.2: Groupings of trigger towers used in L1Calo electron/photon and tau/hadron triggers [43]

ter. The equivalent 2×2 tower block, located behind the EM core, in the hadronic calorimeter is defined as the hadronic core. Hadronic clusters are also formed by summing each of EM clusters, with the hadronic core. The transverse energies deposited in these regions (the ATLAS trigger works entirely in E_{T}) are defined as being the EM cluster energy, EM core energy, hadronic (or tau) cluster energy and the hadronic core energy. In addition, the 12 towers around the EM core are defined as the EM isolation ring, and the equivalent 12 towers in the hadronic calorimeter around the hadronic core are defined as being the hadronic isolation ring. The energies deposited in these rings are defined as being the EM isolation and hadronic isolation energies respectively. It is by setting limits on the amount of energy allowed in these different regions that the trigger isolation thresholds are defined.

Electron/Photon Trigger

The electron/photon and hadron/tau triggers together have a total of 16 different sets of programmable thresholds. Eight of these are allocated to the electron/photon trigger only, with the remaining eight shared between the two triggers as desired. The electron/photon thresholds use cuts on the EM cluster energy and on three different isolation energies (EM isolation ring, hadronic isolation ring and hadronic core) to select candidates. To pass the electron/photon trigger, the most energetic EM cluster must have an energy larger than the EM cluster threshold and the three isolation sums produced must be less than or equal to the appropriate thresholds.

Hadron/Tau Trigger

A maximum of eight threshold combinations exist for the hadron/tau trigger. The thresholds are on the hadron/tau cluster energy plus the EM and hadronic ring isolation energies. The most energetic hadron/tau cluster must have an energy larger than the hadronic cluster threshold and the EM and hadronic isolation ring energy sums must be less than or equal to their associated thresholds for a particular hadron/tau trigger to be passed.

In addition to the cluster and isolation conditions, a window can only produce an RoI if the central 2×2 'core' cluster (EM plus hadronic) is an E_{T} maximum when compared to the eight other 'cores' of the surrounding, overlapping windows. The requirement avoids multiple counting of, for example, a large energy deposit centred

in only one or two trigger towers [43]. The cluster RoI consists of the EM core (2×2 cluster region) added to the hadronic core. Successful cluster trigger candidate RoI are passed on to the LVL2 trigger, together with details of which trigger thresholds have been passed.

3.4.3 Jet Trigger

The L1Calo jet trigger covers the region $|\eta|$ <3.2 and uses a lower granularity than the cluster triggers. Instead of just using trigger towers alone, the jet trigger uses jet elements consisting of blocks of 2×2 towers and as a result each element has a granularity of approximately 0.2×0.2 in $\triangle\eta \times \triangle\phi$. A jet trigger RoI consists of 2×2 jet elements summed over the depth of the EM and hadronic calorimeters. Jet E_{T} can be measured via one of three different algorithm windows, and these are shown in Fig. 3.3.

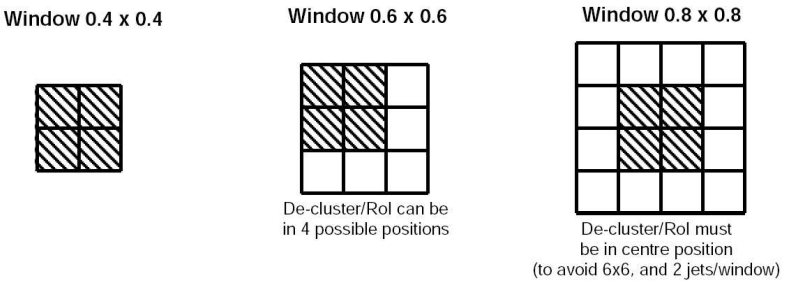

Figure 3.3: Groupings of jet elements used in the L1Calo main jet trigger for jet E_{T} measurement (Jet RoI are hatched) [43]

There are eight threshold groups for the jet trigger, each of which comprises a particular choice of algorithm window size and a value for the minimum jet E_{T}. If

the jet trigger is passed, a jet trigger candidate is produced. For this to happen, the E_{T} of the jet window must exceed the minimum jet E_{T} threshold and the E_{T} of the jet RoI must be larger than that of the surrounding RoI. The jet trigger candidates produced are passed on to LVL2.

In addition to the main jet trigger, there is also an ATLAS forward jet trigger that covers $|\eta|$ <4.9. This makes use of the ATLAS forward calorimeters and has four threshold groups. The granularity is also further reduced relative to the main jet trigger.

3.4.4 Missing E_{T} and Total E_{T} Triggers

The missing and total E_{T} triggers use the full calorimeter system, including the forward calorimeters, and hence cover the region $|\eta|$ <4.9. A summation over jet elements (as used for the jet trigger) is carried out to produce a map of the energy coverage which has a granularity of 0.2×0.2 in $\triangle\eta \times \triangle\phi$. The E_{x} and E_{y} vectors are summed to produce a vector corresponding to the direction of any missing E_{T} present in the event. All the E_{T} values recorded in the calorimeter are also simply added to produce a value for the total event scalar E_{T}. For details on how E_{x} and E_{y} are obtained in the trigger hardware, see [46]. The missing E_{T} trigger has eight thresholds while in 2009-2010 the total scalar E_{T} trigger had four thresholds. From the 2011 run the total E_{T} trigger will also have eight thresholds, and a new trigger on missing E_{T} significance, proportional to missing $E_{\mathrm{T}}/\sqrt{(\mathrm{SumET})}$, will be added.

3.5 Conclusions

An overview was provided of the ATLAS trigger system. The three trigger levels were introduced, comprising the hardware based level 1 and the software based level 2 and event filter (together known as the higher level trigger), and each briefly described. This was followed by a note on how the levels are combined into trigger chains and menus. Finally, more detail was provided on the level 1 calorimeter trigger including information on how the cluster, jet and and missing/total E_{T} triggers are formed.

Chapter 4

Level 1 Tau Trigger Performance

4.1 Introduction

Contained within this chapter is a description of a study carried out into the performance of the ATLAS level 1 tau trigger. Official ATLAS simulated data were used for samples of $t\bar{t}$ and $Z \rightarrow \tau\tau$ events to make comparisons between the Monte Carlo truth taus present and the Regions of Interest (RoI, see chapter 3 for details) produced when the generated events were passed through a complete simulation of the ATLAS detector and trigger system. The aim of the study was to look at the level 1 tau trigger performance for different processes, trigger thresholds, isolation cuts and over a range of p_{T}. $Z \rightarrow \tau\tau$ events provided a very clean source of taus which in principle are easy to trigger on, whereas $t\bar{t}$ events tested the trigger in a much more complicated enviroment, but one which is normal at the LHC.

4.2 Trigger analysis details

The work detailed in this chapter was initially carried out in Athena release 11.0.41/12.0.6 for a centre of mass energy of 14 TeV prior to the commencement of LHC running. This was carried out as part of the ATLAS 'CSC' (Computer System Commissioning) effort which was a collaboration wide exercise to test the readiness of all analyses prior to the planned start of data taking. The precise details covered here began as an examination of the acceptance of a proposed tau trigger menu for top physics, which was extended to examine the performance of LVL1 tau trigger isolation as a function of p_{T} and cluster cut value. As the LHC beam energy changed between the end of the CSC effort and the beginning of data taking in 2010, these studies were subsequently revisited in 2010 when a more realistic set of trigger simulations were available. Also presented in this chapter are the results of repeating this analysis for release 15.6.13.7 7 TeV centre of mass simulated data. Differences produced as a result of the centre of mass energy change, together with changes made to the trigger calibration between the two releases, are stated where necessary. Analysis was carried out on complete sets of AOD files without the application of any preselection.

To produce the results described, datasets of two event types were considered, all of which were produced centrally by ATLAS. The first was the $t\bar{t}$ dataset containing semileptonic and dileptonic decaying $t\bar{t}$ events, with leptonic decays of top quarks to taus allowed to occur. The second was the $Z \rightarrow \tau\tau$ sample. For release 12.0.6 the 14 TeV $\mathrm{t\bar{t}}$[1] and $Z \rightarrow \tau\tau$[2] samples used formed part of the 'CSC' production.

[1]Sample trig1_misal1_mc12.005200.T1_McAtNlo_Jimmy.recon.AOD.v12000604_tid007900

[2]Sample trig1_misal1_csc11_V2.005188.A3_Ztautau_filter.recon.AOD.v12000601_tid008566

The equivalent 7 TeV $t\bar{t}$[3] and $Z \rightarrow \tau\tau$[4] samples used in release 15.6.13.7 were taken from the 'mc09' production.

Within ATLAS data (for real and to a lesser extent simulated samples) the LVL1 trigger information can be accessed in a number of different ways. For this study the LVL1 trigger objects within the AOD were used. Details were obtained of LVL1 RoI produced by anything passing the LVL1 EM or tau cluster triggers in an event [5]. These included the η and ϕ values of each RoI produced, plus the values of the various core, cluster and isolation energies (for further details on how these are defined, see 3.4.2). Also used was the 'Monte Carlo' truth information for the events, namely the values for η, ϕ and p_{T} of each truth particle. Information on the parents and daughters of each truth particle was also used to compute the visible p_{T} of the truth taus as described in 4.4.1.

4.3 Truth matching of taus

The analysis used spatial matching between each truth tau particle in each event and its associated RoI should one be present. Whenever a tau was found in the truth particles, an algorithm would loop through the relevant RoI's for the event and compare each to the truth tau, calculating the separations $\triangle\eta$ and $\triangle\phi$ between

[3]Sample mc08.105200.T1_McAtNlo_Jimmy.merge.AOD.e357_s462_r635_t53

[4]Sample mc08.106052.PythiaZtautau.merge.AOD.e347_s462_r635_t53

[5]At the time of the CSC studies, information on LVL1 RoI was to be found, in differing formats, inside two separate objects within the software. These were merged into a single object by the time the later data were analysed

the truth particle and each RoI. The $\triangle R$ in each case was thereby calculated using 4.1.

$$\triangle R = \sqrt{(\triangle\eta^2 + \triangle\phi^2)} \tag{4.1}$$

For each truth tau the best matching RoI was assigned as giving the smallest $\triangle R$. Fig. 4.1 shows the minimum $|\triangle R|$ values corresponding to the closest RoI for each truth tau, inside the region $|\eta|$ <2.5 covered by the L1Calo cluster trigger.

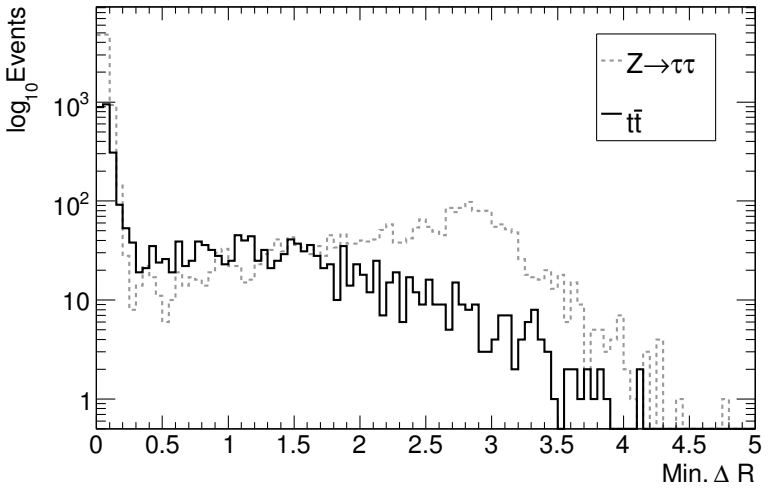

Figure 4.1: Minimum $|\triangle R|$ corresponding to the best matched RoI plotted on a log scale for both $t\bar{t}$ and $Z \rightarrow \tau\ \tau$ events (14 TeV centre of mass energy)

The difference in environment present for the $t\bar{t}$ and $Z \rightarrow \tau\ \tau$ events can be seen in Fig. 4.1. For $Z \rightarrow \tau\ \tau$ events, the τ^+ and τ^- should generally be produced back to back in ϕ. Thus a peak corresponding to the mismatched taus in the $Z \rightarrow \tau\ \tau$ plot occurs at $\triangle R \approx \pi$. For $t\bar{t}$ events containing one or more taus there are a number of other items present in each event which could produce an RoI. Hence the $t\bar{t}$ distribution over $\triangle R$ is continuous for the poorly matched taus rather than being peaked as for $Z \rightarrow \tau\ \tau$.

4.4 Tau Trigger Efficiencies

The LVL1 tau trigger efficiency was examined in a variety of senarios. A value of $\triangle R = 0.3$ was used to determine whether the trigger had fired correctly or not. Truth taus less than $\triangle R = 0.3$ away from the closest RoI were referred to as being well spatially matched to an RoI and considered a trigger success. For truth taus with $\triangle R > 0.3$, the trigger was considered to have failed. The tau cluster threshold, EM isolation threshold and hadronic isolation thresholds were varied, while the EM cluster threshold was not used. Only taus within the real calorimeter coverage of $|\eta| < 2.5$ were considered.

Due to the complex nature of $t\bar{t}$ events, taus can be produced in different ways. It is considered important to trigger with high efficiency those taus which come directly from the W-boson produced by the decay of the top (referred to here-on as 'prompt taus'). For the top sample used, such taus comprised $\sim$82% of the truth taus in the range $|\eta| < 2.5$, as opposed to those from other sources such as B-mesons. Consequently, all aspects of the analysis were carried out initially for just those prompt taus coming from the W from the top and then for all taus within the $t\bar{t}$ sample.

4.4.1 Efficiency without application of isolation

Initially the trigger efficiency, plotted versus the truth tau visible p_{T}, was considered without any isolation conditions being applied.

The truth visible p_{T} represents what the trigger should see in an ideal calorimeter with an ideal cluster. It was calculated by taking the truth tau p_{T} and subtracting from it the p_{T} associated with any muons or neutrinos which are daughter particles of the decaying tau. This was done component by component with the 'visible p_{T}' being reconstructed at the end of the process. In all the samples used, truth taus can be seen to radiate one or more photons before actually decaying. The p_{T} of the tau was taken at the point where it decayed into daughters.

A series of different tau cluster thresholds was applied to the samples with values chosen to resemble an ATLAS LVL1 early trigger menu. Values of 5, 6, 9, 11, 16, 25 and 40 GeV were applied. Fig. 4.2 shows the efficiency as a function of the visible p_{T} for the prompt taus in the 14 TeV and 7 TeV $t\bar{t}$ samples and for a tau cluster threshold of 25 GeV. In Fig. 4.3 the efficiency is shown versus the visible p_{T} for four of the tau cluster thresholds, again for the prompt taus in the 14 TeV $t\bar{t}$ sample. Fig. 4.4 shows the equivalent plots for the 7 TeV $t\bar{t}$ sample.

From Fig. 4.2(a) it can be seen that before isolation cuts are applied the trigger performance appears satisfactory with full efficiency being reached for a truth visible p_{T} value of approximately 30 GeV and an efficiency at threshold of approximately 98%. The turn on is not as sharp as would be expected for an equivalent electron or muon trigger. Fig. 4.3 illustrates this with the turn on curves for the four thresholds overlapping despite comparatively large threshold spacings. Looking at Fig. 4.2(b) it can be seen that for the 7 TeV $t\bar{t}$ sample full efficiency is reached at approximately the same value of the tau visible p_{T} as for the 14 TeV sample, but with a softer

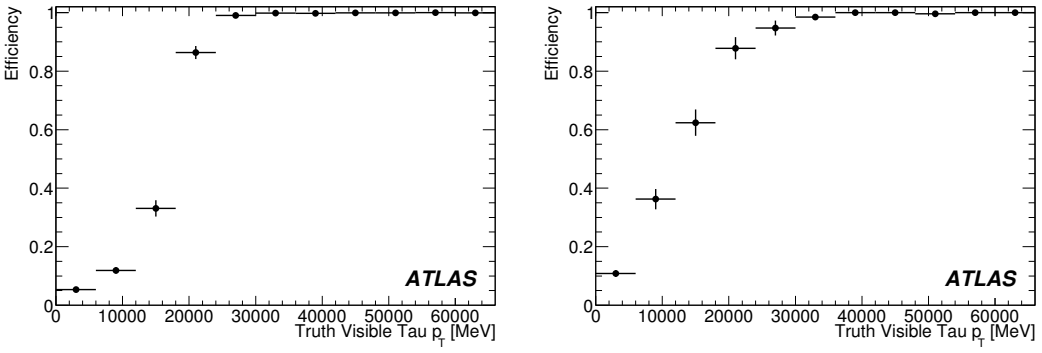

(a) 14 TeV *(b)* 7 TeV

Figure 4.2: Trigger efficiency as a function of the truth visible p_{T} for a tau cluster threshold of 25 GeV. The turn on curve is for prompt taus in $t\bar{t}$ events. No isolation condition is applied

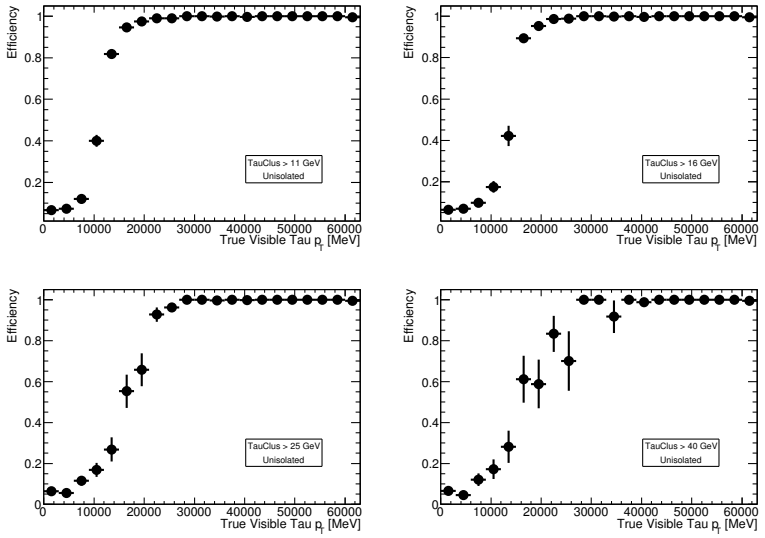

Figure 4.3: Trigger efficiency as a function of the truth visible p_{T} for four tau cluster thresholds. The turn on curves are for prompt taus in $t\bar{t}$ events. No isolation condition is applied (14 TeV centre of mass energy)

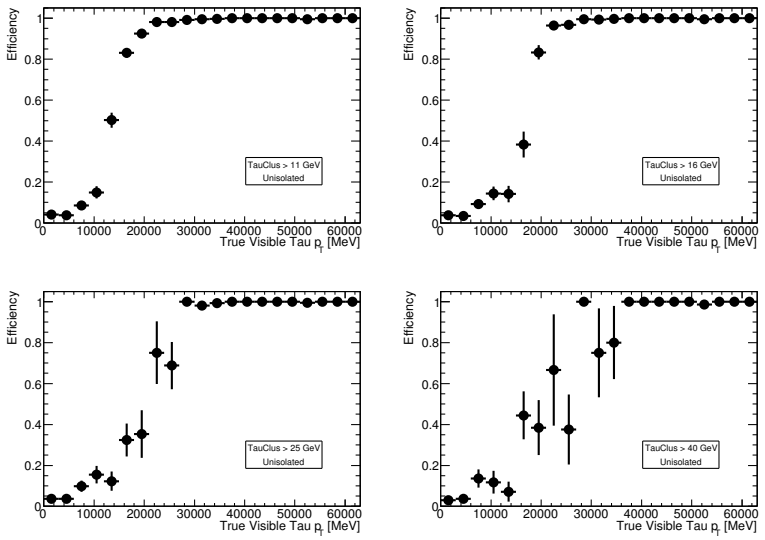

Figure 4.4: Trigger efficiency as a function of the truth visible p_{T} for four tau cluster thresholds. The turn on curves are for prompt taus in $t\bar{t}$ events. No isolation condition is applied (7 TeV centre of mass energy)

turn on for the same tau cluster threshold of 25 GeV. The efficiency at threshold is fractionally smaller for the 7 TeV sample, at approximately 95%. Comparing Fig. 4.3 and Fig. 4.4 it can be seen that this behaviour is common across all four thresholds, with the turn on being softer for the 7 TeV sample in each case but with maximum efficiency reached for approximately the same value of the truth visible p_{T} of the tau.

The difference observed between the 14 TeV and 7 TeV results is largely due to changes made, in the simulated L1Calo trigger calibration and tower noise cuts, between the production of the 14 TeV and 7 TeV samples. In the 14 TeV samples, settings had been used which were intended to represent a finalised tuning of the trigger. The E_{T} calibrations of the trigger towers had been adjusted (by varying the

gains), to partially compensate for the varying amounts of material located in front of the calorimeter (dead material correction). This served to provide as uniform a response (i.e. trigger turn on) as possible as a function of trigger tower η. Gain levels were also set so as to improve the hadronic response in relatively energetic jets, with tower noise cuts kept low to increase sensitivity to small signals. A more realistic trigger configuration was applied for the 7 TeV Monte Carlo production, so as to better describe the detector performance observed during the commissioning of ATLAS. Trigger towers were calibrated by simply matching the E_{T} seen in each tower to the raw E_{T} measured for the corresponding cells in the readout. This 'EM scale' calibration does not correct for the variation in dead material in front of the calorimeter, resulting in slightly lower signals and the trigger efficiency turn on developing a less uniform η dependence (softer where more material is present). When averaged across the whole calorimeter, the overall trigger turn on produced was therefore less sharp than for the older idealised calibration. Furthermore, to match the commissioning data, higher electronic noise threshold cuts and less uniform pedestal subtractions were applied to trigger towers in the 7 TeV samples. All these factors reduce the sensitivity of the trigger to small signals, compared to the 14 TeV Monte Carlo, and so produce a slower turn on for a given trigger threshold.

A check was carried out on the process dependence of the LVL1 tau trigger before the application of any isolation constraints. In Fig. 4.5 the efficiency versus visible tau p_{T} is shown for both $t\bar{t}$ events and $Z \rightarrow \tau\,\tau$ samples for the 25 GeV tau cluster threshold. No clear process dependence is apparent as a function of the tau visible p_{T}.

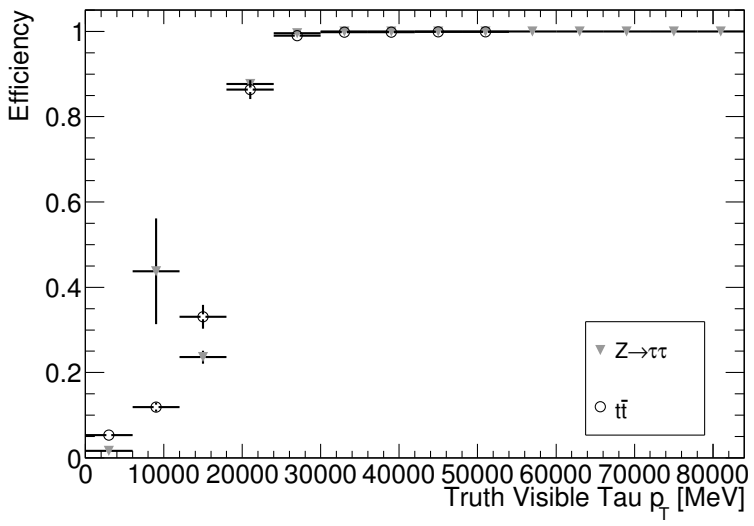

Figure 4.5: Trigger efficiency as a function of the truth visible p_{T} for a 25 GeV tau cluster threshold. The turn on curve is shown for $t\bar{t}$ and $Z \rightarrow \tau\ \tau$ events. No isolation is applied and only prompt taus are included for $t\bar{t}$ events (14 TeV centre of mass energy)

A further comparison was made between the turn on curves for the top sample when considering only the prompt taus, to the turn on curves when all the truth taus were used. Comparison between the two cases as a function of the visible p_{T} of the tau is presented in Fig. 4.6 where no isolation was applied. What is observed for both 14 TeV and 7 TeV centre of mass energies is a softening of the turn on curve when all the taus in the sample are included instead of just the prompt taus. The efficiency turn on also occurs earlier when all taus are considered, with the efficiency in each bin being larger than for the prompt taus until the plateau is reached. This is explained by the fact that the efficiency is plotted as a function of the visible p_{T} of the truth tau. For the prompt case the tau is produced as an isolated object and so the energy seen by the L1 tau cluster is largely due to tau alone. When all the

taus are taken into account, 20% of the truth taus originate from a B-meson and so would be expected to lie either inside, or in close proximity to, a particle jet. If an isolation constraint is not applied, then in the latter case the energy recorded by the L1 tau cluster would include energy from the jet, as opposed to just the tau visible energy. Consequently, taus located within a jet can pass the L1 trigger despite having an energy below the tau threshold, whereas prompt taus cannot. Therefore when the trigger efficiency is plotted as a function of the true visible tau p_{T} the turn on is softer than is seen for the prompt taus alone. As the probability of correctly reconstructing a tau produced from B-meson decay is close to zero, for physics purposes it is the performance of the trigger for the prompt taus that is important.

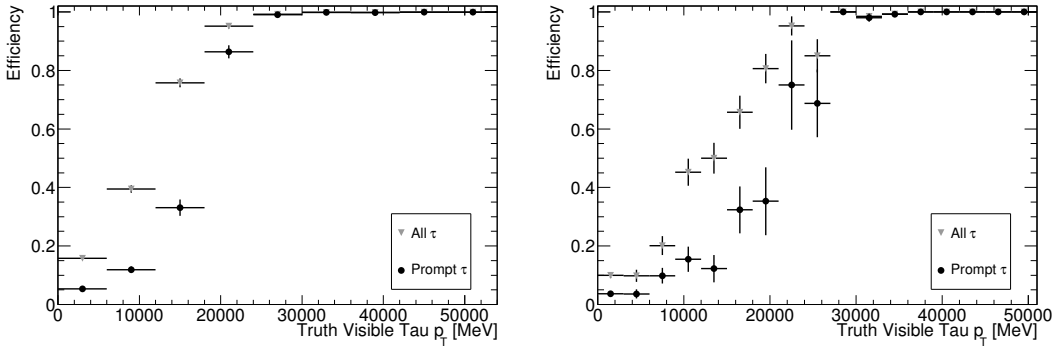

(a) 14 TeV *(b)* 7 TeV

Figure 4.6: Trigger efficiency as a function of the truth visible p_{T} for a tau cluster threshold of 25 GeV. The turn on curve is shown for both the prompt taus alone and for all the taus in the $t\bar{t}$ sample. No isolation condition is applied

4.4.2 Effect of different isolation cuts

The effect of applying a series of EM and hadronic isolation cuts on the trigger efficiency was studied as a function of the truth visible p_{T} of the tau. The same trigger condition and constraints, as discussed in 4.4.1, were retained with a fixed tau cluster threshold of 25 GeV also being added. A series of new cuts were then applied on the energy allowed in the RoI EM and hadronic isolation rings (defined in Fig. 3.2). Cuts were applied separately for the EM and hadronic isolation cases. Refinement of the cuts was carried out in order to focus on the region sensitive to changes in the size of the isolation cut[6]. The final values chosen were:

- EM isolation cuts of 4, 5, 6, 7 and 8 GeV
- Hadronic isolation cuts of 2, 3, 4, 5 and 6 GeV

Results for 14 TeV centre of mass energy

It was seen for a centre of mass energy of 14 TeV that the smaller cuts produced too drastic an effect on the efficiency, but that the larger cuts offered the potential to be used to improve the rejection against fake taus. Fig. 4.7 demonstrates this by showing the results of applying 4 and 6 GeV EM isolation cuts and 2 and 5 GeV hadronic isolation cuts on the trigger efficiencies for the prompt taus in the $t\bar{t}$ sample respectively.

The cuts on the isolation were studied for a fixed cut on the tau cluster p_{T} of

[6]Optimised for the 14TeV sample

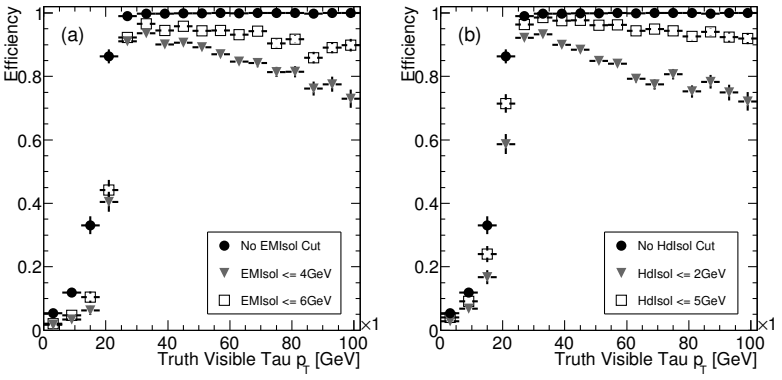

Figure 4.7: Plots of tau trigger efficiency versus truth visible p_{T}, with isolation applied, for prompt taus in the $t\bar{t}$ process for a centre of mass energy of 14 TeV. The left plot shows the effects of 4 and 6 GeV cuts on EM isolation while the right plot shows the effect of 2 and 5 GeV cuts on hadronic isolation

25 GeV. Fig. 4.7 shows how the isolation cuts affect the trigger efficiency as p_{T} increases. Above approximately 30 GeV, as the truth visible p_{T} of the tau increases there is a drop off in the efficiency observed. Tightening the isolation cut causes a more dramatic fall off in efficiency. This occurs because as the tau p_{T} increases, so the level of leakage into the isolation rings increases and more events become liable to fail the isolation condition. In Fig. 4.7 the 4 GeV EM isolation cut and the 2 GeV hadronic isolation cut produced a very dramatic drop in the efficiency above around 40 GeV. By contrast, the 6 GeV EM isolation cut and the 5 GeV hadronic isolation cut have an effect that is much less dramatic for both samples. These isolation cuts do not particularly damage the trigger efficiency up to around 80 GeV. Thus isolation cuts of this magnitude should be useable to reduce the number of events being triggered by fake taus for a collision centre of mass energy of 14 TeV.

The fall off in efficiency observed for values of the tau visible p_{T} notably larger than the cluster threshold means that care must be taken when tuning LVL1 tau trigger menus. It is important to ensure the changeover from one isolated threshold to the next occurs before the lower threshold trigger efficiency starts to fall away from the plateau level. Furthermore, the drop in efficiency seen at high p_{T} for moderate isolation constraints demonstates why it is sensible for a menu to include high p_{T} non-isolated triggers. These maintain higher efficiency triggering where rate reduction is not as critical as for lower p_{T}.

Results for 7 TeV centre of mass energy

Repeating the analysis, with the same cluster threshold and isolation cuts, for a centre of mass energy of 7 TeV produced the results shown in Fig. 4.8. Again the prompt taus in the $t\bar{t}$ sample were used.

Comparison of Fig. 4.8 to Fig. 4.7 reveals a dramatic difference. The softening of the turn on curve was discussed in 4.4.1, however what is immediately apparent is that for the 7 TeV sample the effect of applying the isolation constraint has been significantly reduced. Whilst a slight fall in efficiency is present for the tighter of the EM and hadronic isolation conditions, particularly at large values of the truth visible p_{T} of the tau, the 6 GeV EM isolation cut and the 5 GeV hadronic isolation cuts have very little effect on the trigger efficiency (when compared to the case with no isolation applied) as a function of the visible p_{T}. For EM isolation, the value at which full efficiency is reached is moved to slightly larger p_{T} than for the case

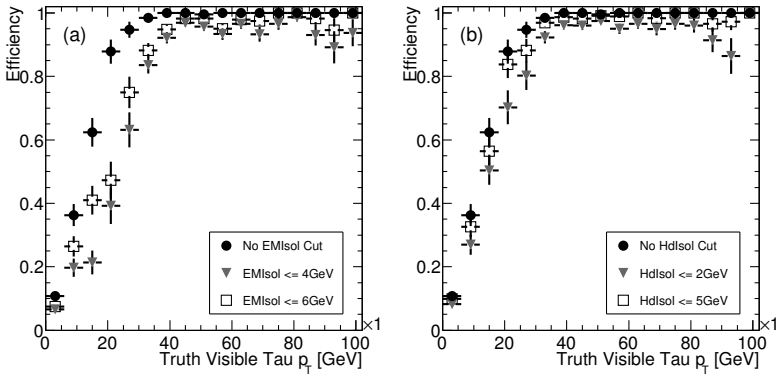

Figure 4.8: Plots of tau trigger efficiency versus truth visible p_{T}, with isolation applied, for prompt taus in the $t\bar{t}$ process for a centre of mass energy of 7 TeV. The left plot shows the effects of 4 and 6 GeV cuts on EM isolation while the right plot shows the effect of 2 and 5 GeV cuts on hadronic isolation

with no isolation applied, but there is then no notable fall-off in efficiency. It is expected that this is again largely due to the lowering of the calibration gains and in particular the increase in the trigger tower noise cuts. Combined, these mean that for a cluster of given energy, the size of the signal observed by the trigger in the isolation region is smaller for the revised settings in the 7 TeV samples. Therefore, a given tau is less likely to fail the same isolation theshold in the 7 TeV case than in the 14 TeV case. Consequently it would appear that for a given tau cluster threshold, it is possible to apply tighter isolation constraints on LVL1 tau trigger for the more recent samples with an LHC centre of mass energy of 7 TeV than was the case for the older samples with a centre of mass energy of 14 TeV. Indeed, as the changes to the trigger configuration will also reduce the isolation ring E_{T} sums for background jets, tighter isolation cuts would therefore be needed to equivalently reject the same

backgrounds in the newer samples.

4.4.3 Comparison of isolation effects for $t\bar{t}$ and $Z \rightarrow \tau\ \tau$ events

An area of particular interest was the comparison of the effect of the isolation cuts on the clean $Z \rightarrow \tau\ \tau$ sample and the complicated $t\bar{t}$ sample. The same isolation cuts given in 4.4.2 were used and applied to both samples in the same way as before. Initially, only the prompt truth taus in the $t\bar{t}$ sample were used. The effect of the five EM isolation and five hadronic isolation cuts when applied to the two samples is shown by Fig. 4.9 for a centre of mass energy of 14 TeV.

Results for 14 TeV centre of mass energy

In order to identify any differences between the samples a cut by cut comparison was carried out. Here the efficiency of the two samples was plotted on the same axes independently for each of the EM and hadronic isolation cuts, thereby permitting the $Z \rightarrow \tau\ \tau$ and $t\bar{t}$ efficiency curves to be compared directly for each cut. The EM isolation cut by cut plots are shown by Fig. 4.10 and the equivalent hadronic isolation plots are shown by Fig. 4.11.

The effect of applying isolation on the trigger efficiency can be seen to be slightly larger for $t\bar{t}$ events than for $Z \rightarrow \tau\ \tau$ events. The difference between the samples is more noticable when considering EM isolation, with the splitting largest in the

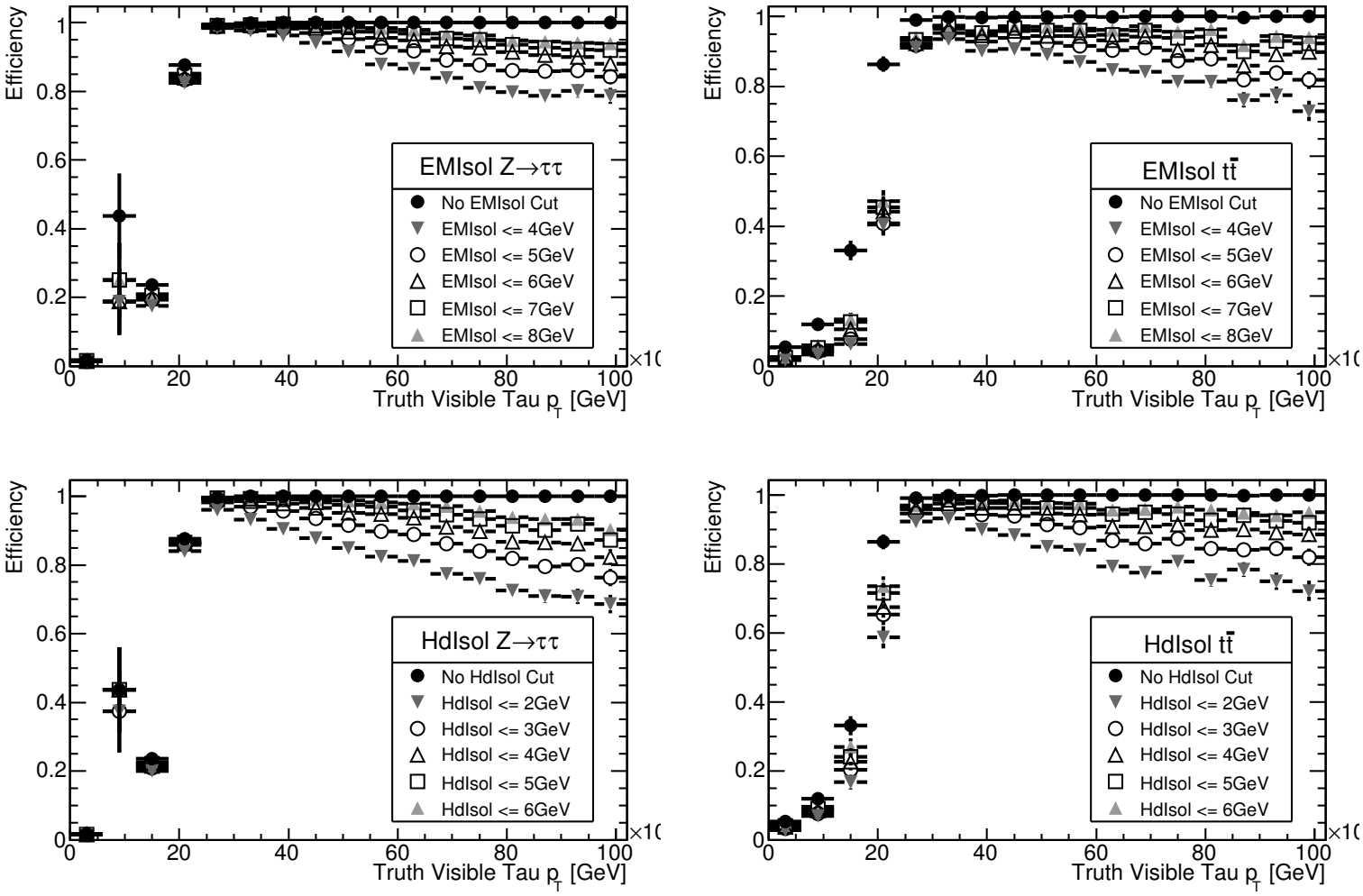

Figure 4.9: Plots of tau trigger efficiency as a function of the truth visible p_{T} with isolation applied for $Z \rightarrow \tau\ \tau$ and $t\bar{t}$ processes. A range of EM and hadronic isolation cuts are shown. The samples used had an LHC centre of mass energy of 14 TeV

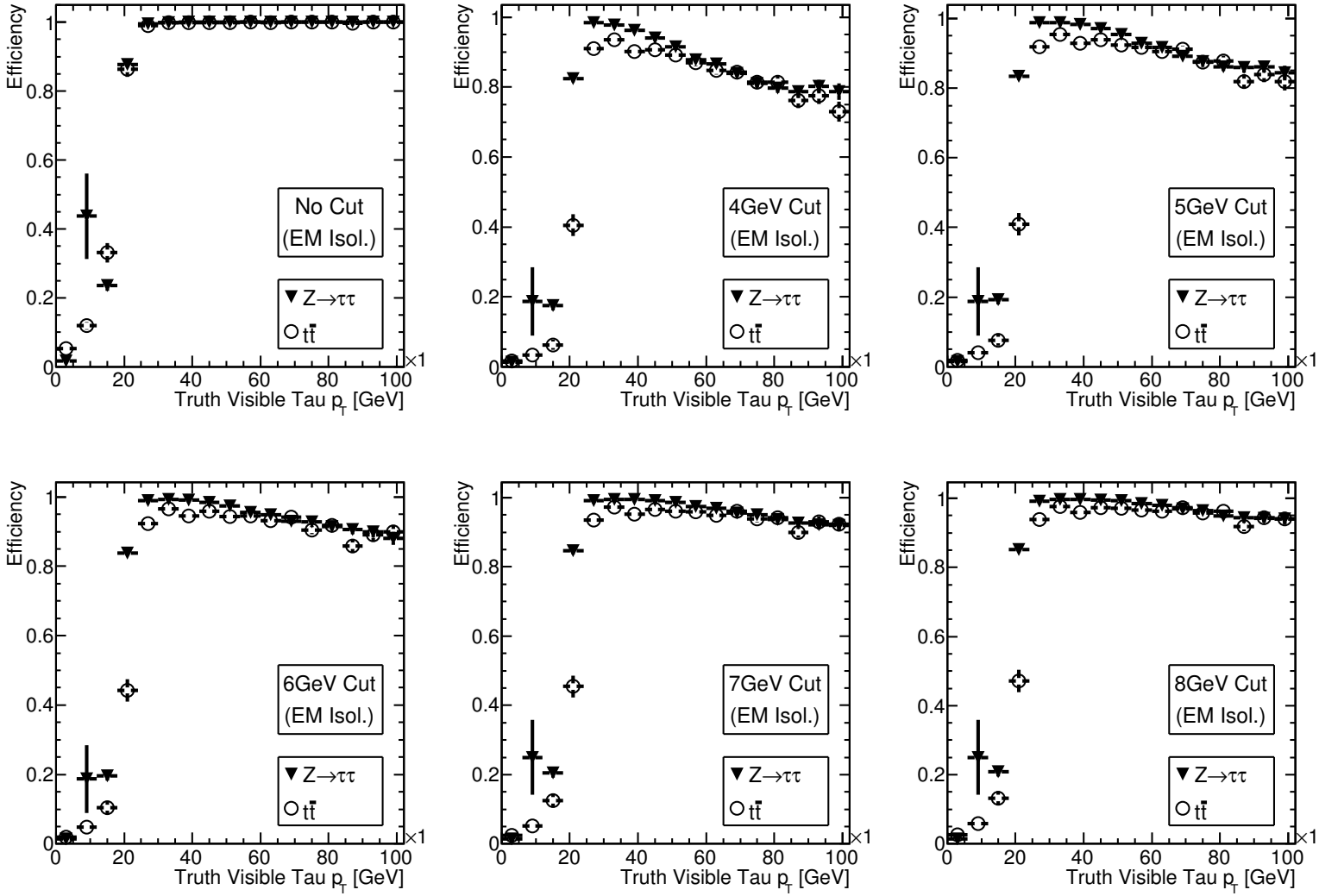

Figure 4.10: Cut by cut comparison of tau trigger efficiency versus truth visible p_{T} with EM isolation applied for the $Z \rightarrow \tau\ \tau$ and $t\bar{t}$ processes (prompt truth taus used for the $t\bar{t}$ sample) for a centre of mass energy of 14 TeV

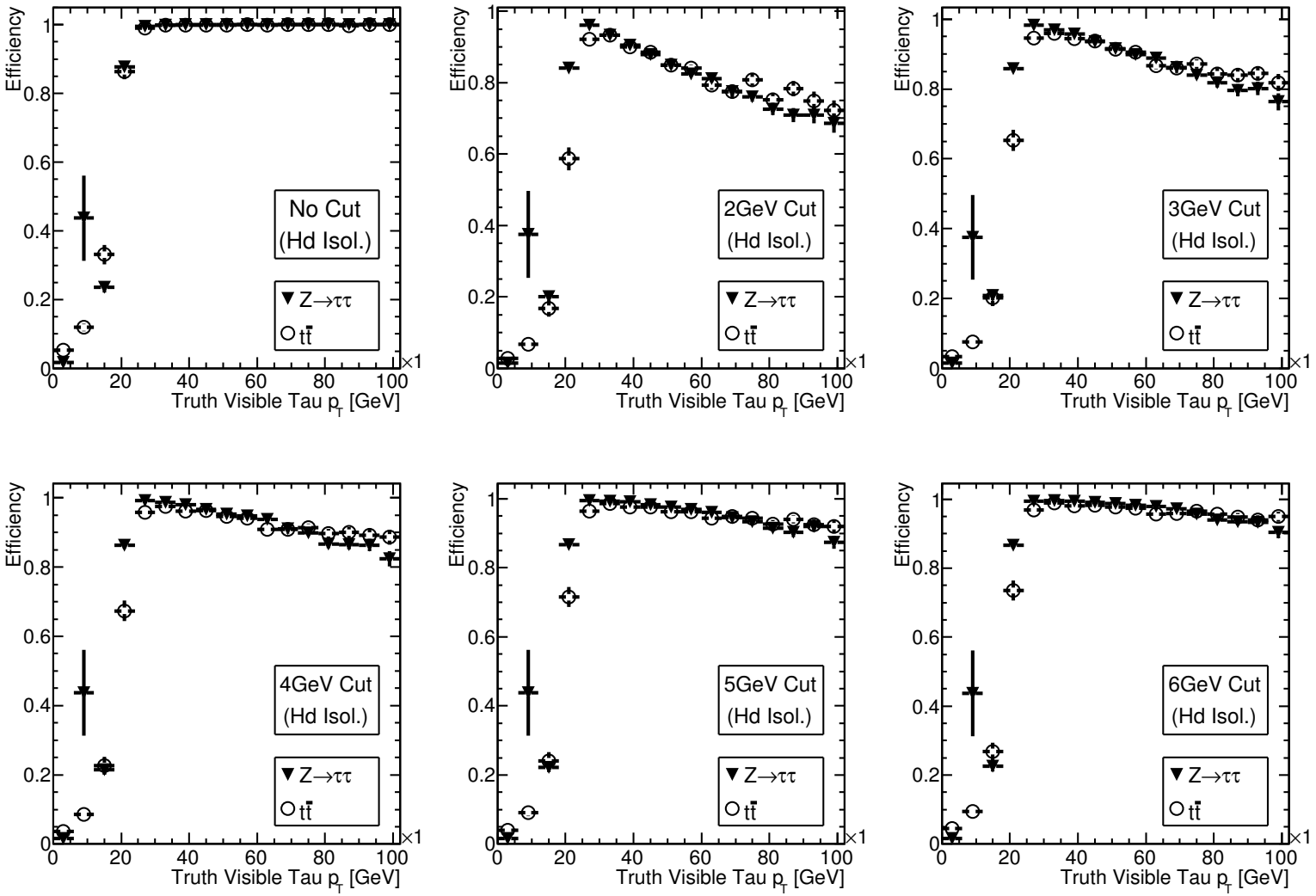

Figure 4.11: Cut by cut comparison of tau trigger efficiency versus truth visible p_{T} with hadronic isolation applied for the $Z \rightarrow \tau\ \tau$ and $t\bar{t}$ processes (prompt truth taus included for the $t\bar{t}$ sample) for a centre of mass energy of 14 TeV

region between approximately 25 and 40 GeV (in the early part of the efficiency plateau region for a fixed tau cluster threshold of 25 GeV). This appears to become smaller as p_{T} is increased above 40 GeV, although the size of the error on the efficiency also starts to grow significantly. Also clearly visible, for both EM and hadronic cases, is that as the size of the isolation cut is increased, loosening the constraint, the separation observed between the $t\bar{t}$ and $Z \rightarrow \tau\ \tau$ efficiency traces is reduced. This is consistent with the fact that when no isolation cuts are applied there is no obvious process dependence of the tau trigger, demonstrated by Fig. 4.5.

As described in 4.4, for the $t\bar{t}$ sample possessed, $\sim$82% of the truth taus in the range $|\eta| < 2.5$ which were well matched to an RoI were prompt taus. The analysis was re-run for the $t\bar{t}$ sample but calculating the trigger efficiency versus truth visible p_{T} for all taus within the sample. The resulting cut by cut plots are shown by Fig. 4.12 and Fig. 4.13 for the EM isolation and hadronic isolation cases respectively.

It is apparent that the act of plotting all the truth taus in the $t\bar{t}$ sample reduces the trigger efficiency observed, further separating the performance from that seen for the $Z \rightarrow \tau\ \tau$ events. This is not entirely surprising as any taus produced from B-mesons in $t\bar{t}$ events would be expected to lie in the centre of a B-jet and as such are therefore unisolated. The reduction observed is more significant for the case of EM isolation as this is where the largest difference was observed previously. As before the discrepancy remains visible between the two samples for EM isolation cuts up to 8GeV. For hadronic isolation, the distinction is also increased between the $Z \rightarrow \tau\ \tau$ and $t\bar{t}$ samples.

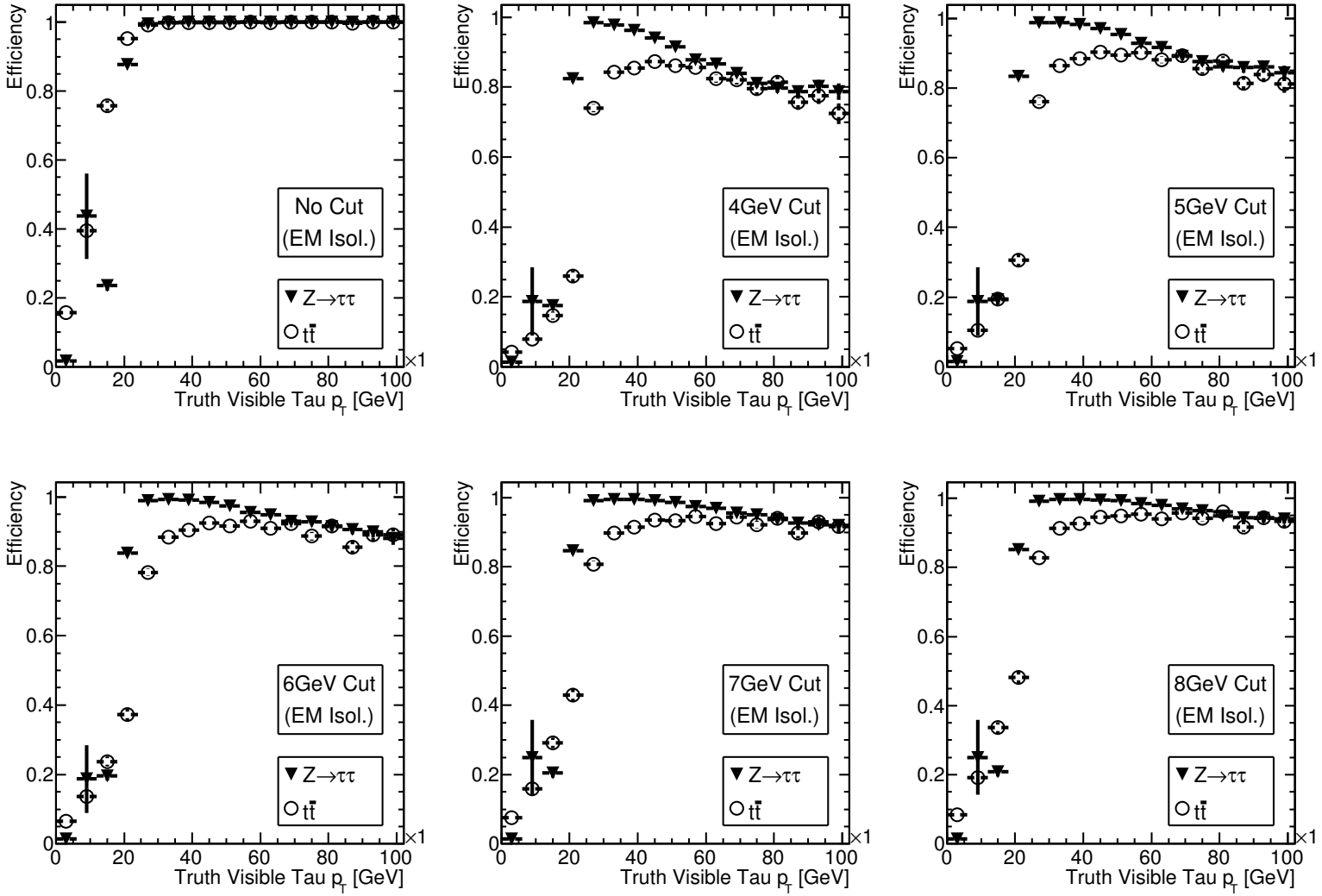

Figure 4.12: Cut by cut comparison of tau trigger efficiency versus truth visible p_{T} with EM isolation applied for the $Z \rightarrow \tau\ \tau$ and $t\bar{t}$ processes (all truth taus included for the $t\bar{t}$ sample) for a centre of mass energy of 14 TeV

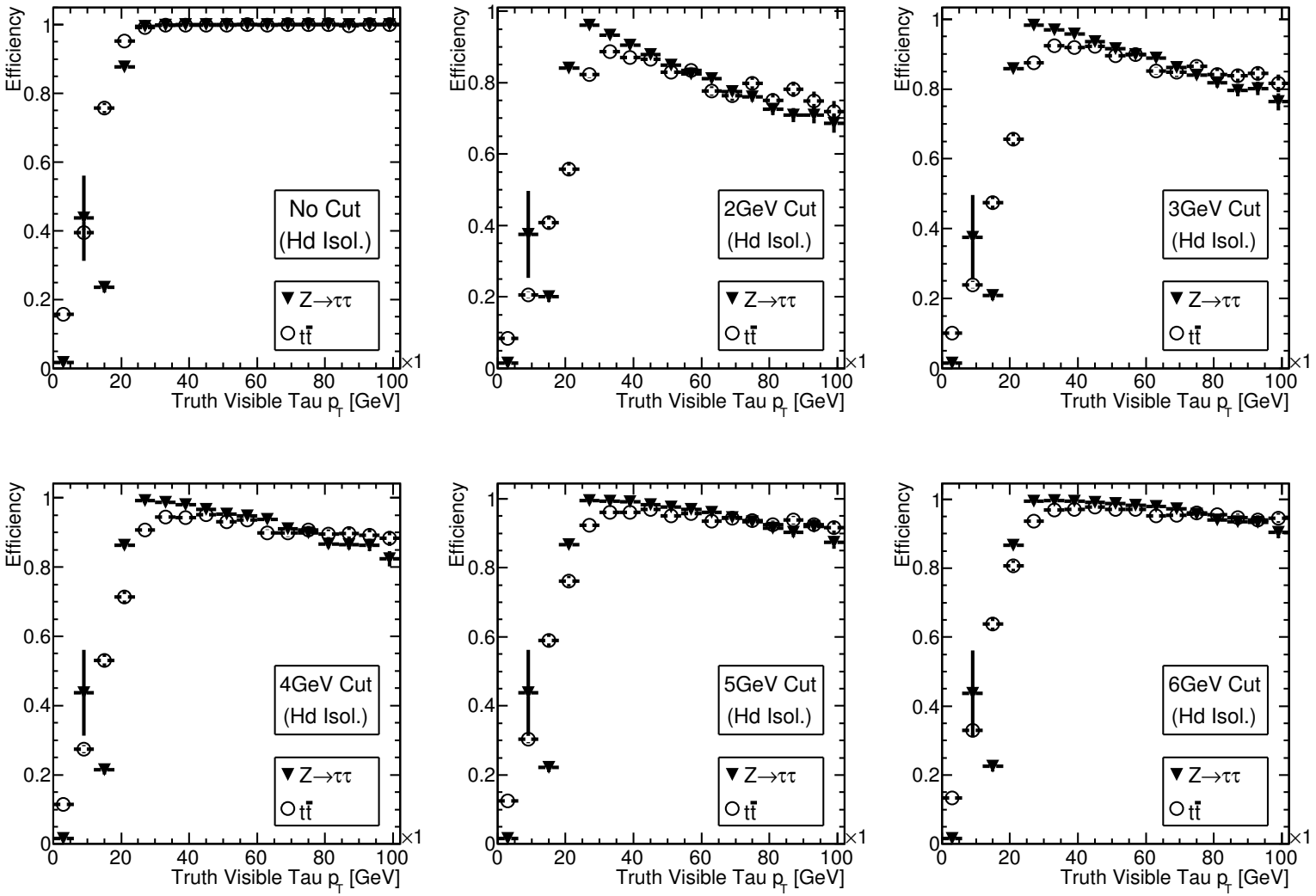

Figure 4.13: Cut by cut comparison of tau trigger efficiency versus truth visible p_{T} with hadronic isolation applied for the $Z \rightarrow \tau\ \tau$ and $t\bar{t}$ processes (all truth taus included for the $t\bar{t}$ sample) for a centre of mass energy of 14 TeV

Results for 7 TeV centre of mass energy

As seen in 4.4.2, the effect of a fixed isolation cut for a given cluster threshold on the 7 TeV samples is significantly reduced compared to the 14 TeV samples. This is reinforced by the cut by cut comparison for the 7 TeV $t\bar{t}$ and $Z \rightarrow \tau\ \tau$ samples shown in Fig. 4.14 and Fig. 4.15 (using the prompt taus in the $t\bar{t}$ case). Compared to the equivalent 14 TeV plots in Fig. 4.10 and Fig. 4.11 what is most striking is that the significant splitting previously seen is no longer observed for all values of the EM and hadronic isolation cuts. While the turn on for the $t\bar{t}$ events remains softer than for $Z \rightarrow \tau\ \tau$, as can be seen for visible p_{T} between 10 and 30 GeV, the efficiency for prompt taus in $t\bar{t}$ events in the plateau region is well modelled by the taus in the $Z \rightarrow \tau\ \tau$ events. Consequently, LVL1 tau trigger efficiencies measured from data for $Z \rightarrow \tau\ \tau$ events (for similar trigger conditions) should provide a good estimate of the trigger efficiency in the plateau region for prompt taus in $t\bar{t}$ events for an LHC collision centre of mass energy of 7 TeV. This applies for both isolated and non-isolated triggers (for the case of 14 TeV samples, tag and probe would allow a good estimate of the non-isolated triggers only). A caveat is that it is likely the reason for the reduced separation is a consequence of the overall reduced effect of the isolation cuts in the 7 TeV samples (as a consequence of the higher noise cuts and adjusted calibration). Therefore, if a tightening of the isolation cuts is required in order to control trigger rates, it is possible that the splitting seen in the 14 TeV samples could return (more likely for very tight isolation cuts).

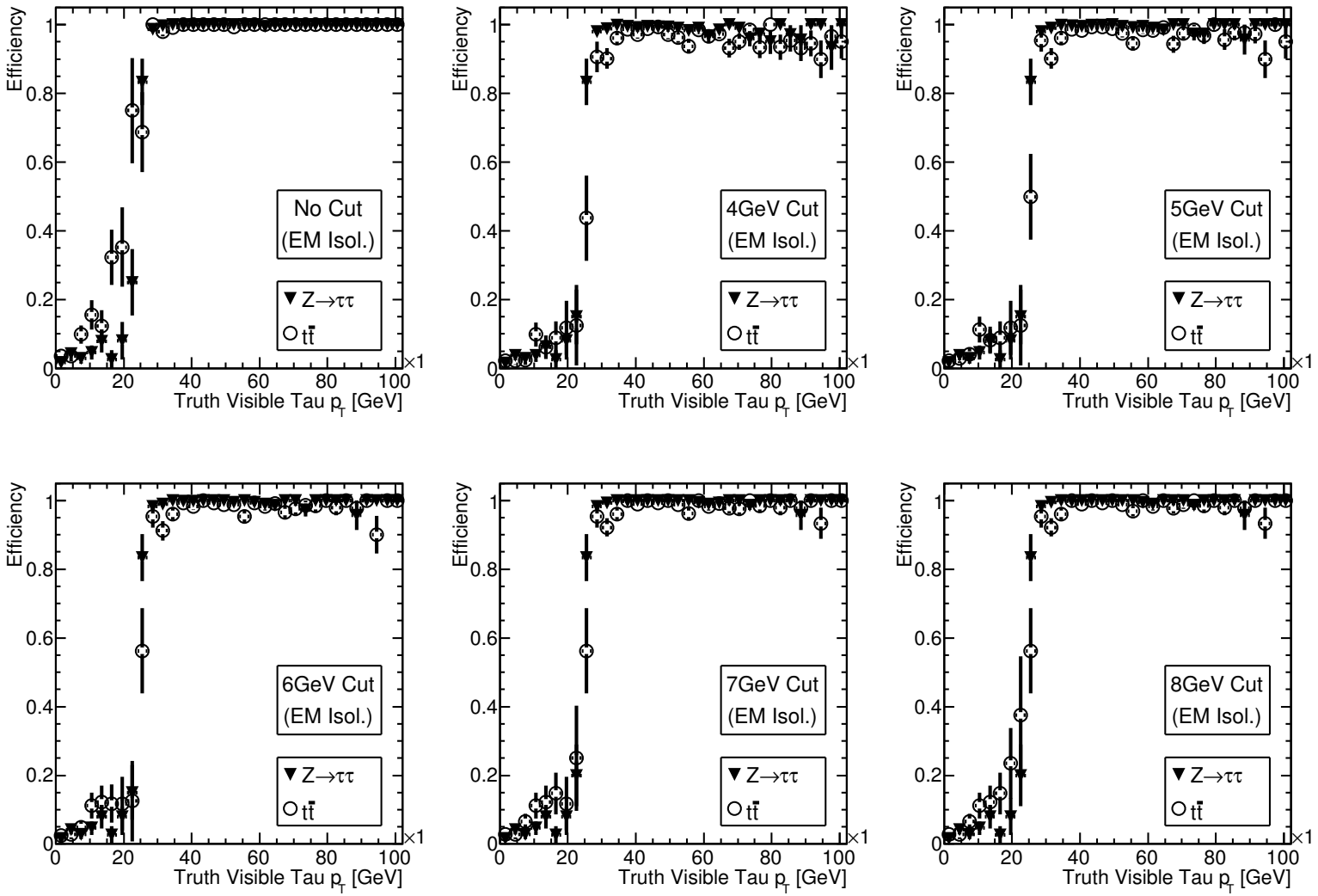

Figure 4.14: Cut by cut comparison of tau trigger efficiency versus truth visible p_{T} with EM isolation applied for the $Z \rightarrow \tau\ \tau$ and $t\bar{t}$ processes (prompt truth taus used for the $t\bar{t}$ sample) for a centre of mass energy of 7 TeV

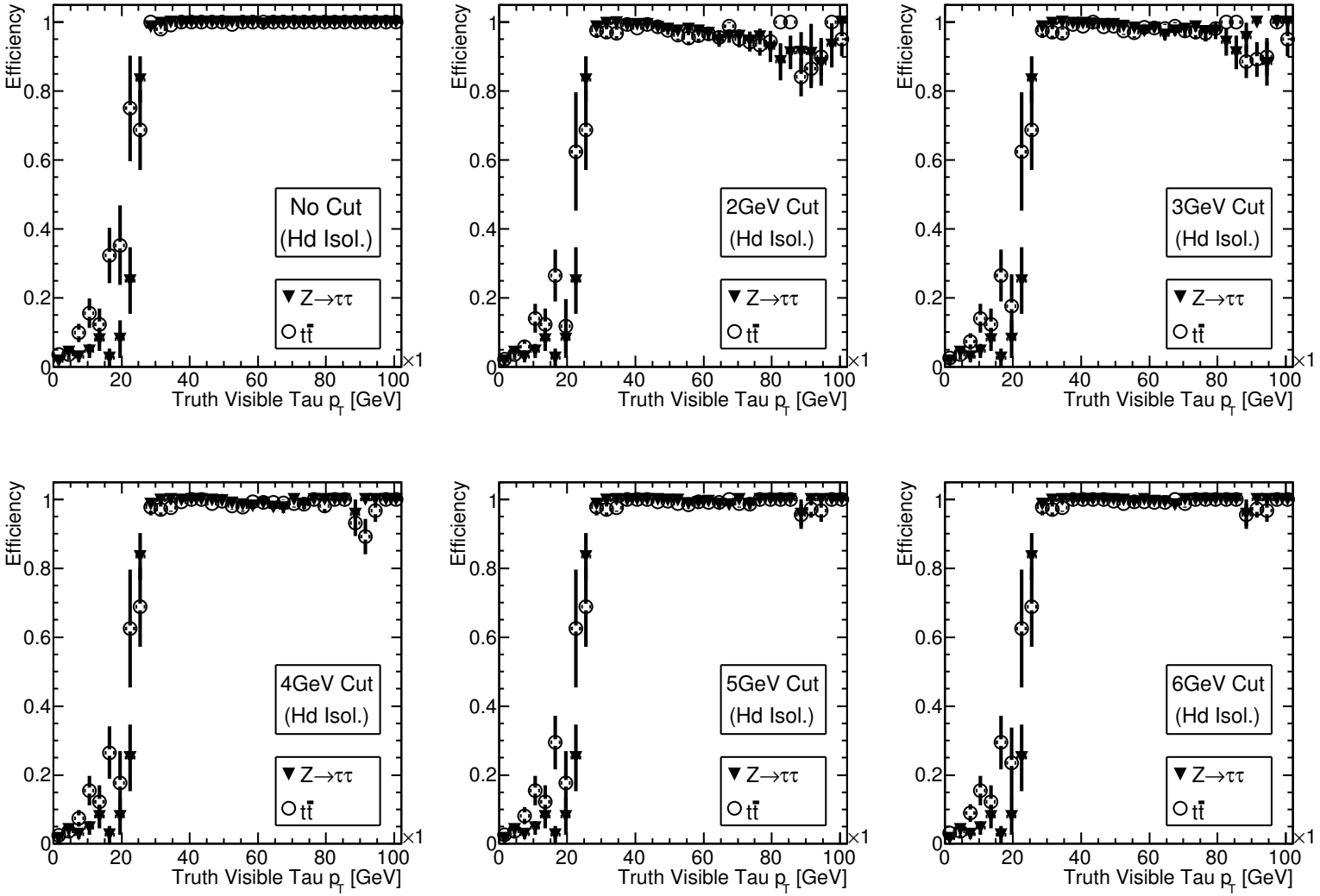

Figure 4.15: Cut by cut comparison of tau trigger efficiency versus truth visible p_{T} with hadronic isolation applied for the $Z \rightarrow \tau\ \tau$ and $t\bar{t}$ processes (prompt truth taus included for the $t\bar{t}$ sample) for a centre of mass energy of 7 TeV

4.4.4 Examining the effect of jets for $t\bar{t}$ events

A check was made on whether the effect of applying isolation has a different effect on the tau trigger efficiency for fully leptonic $t\bar{t}$ events when compared to a mixture of semileptonic and dileptonic $t\bar{t}$ events. The dileptonic events contain two fewer light quark jets than the semileptonic ones. There were two motivations behind this comparison. Firstly, it was intended to check whether overlap of the tau with light quark jets was the reason for the reduced efficiency in $t\bar{t}$ events, compared to $Z \rightarrow \tau$ τ events, when isolation was applied. If this were the case the trigger efficiency would be expected to be higher for the dileptonic only $t\bar{t}$ events when running isolation. Secondly, looking at the difference between the two $t\bar{t}$ event types would test the idea that dileptonic $t\bar{t}$ events could be used to study the tau trigger efficiency in semileptonic events if the differences between the two were to be small. Equivalent efficiency plots were produced using taus coming from dileptonic $t\bar{t}$ events only, both for the case where all the taus were considered and for the case where only the prompt taus were used. Again the equivalent cut by cut comparison plots were produced to examine any differences in the trigger efficiency curves that may have been produced as a result of using the two differing $t\bar{t}$ channels. Fig. 4.16 and Fig. 4.17 show the results produced when the dileptonic $t\bar{t}$ event tau trigger efficiencies were compared to those for mixed semileptonic and dileptonic $t\bar{t}$ events, using the prompt taus only.

No difference was observed, within errors, between the efficiencies produced when only semileptonic $t\bar{t}$ events were used and those produced when only dileptonic $t\bar{t}$

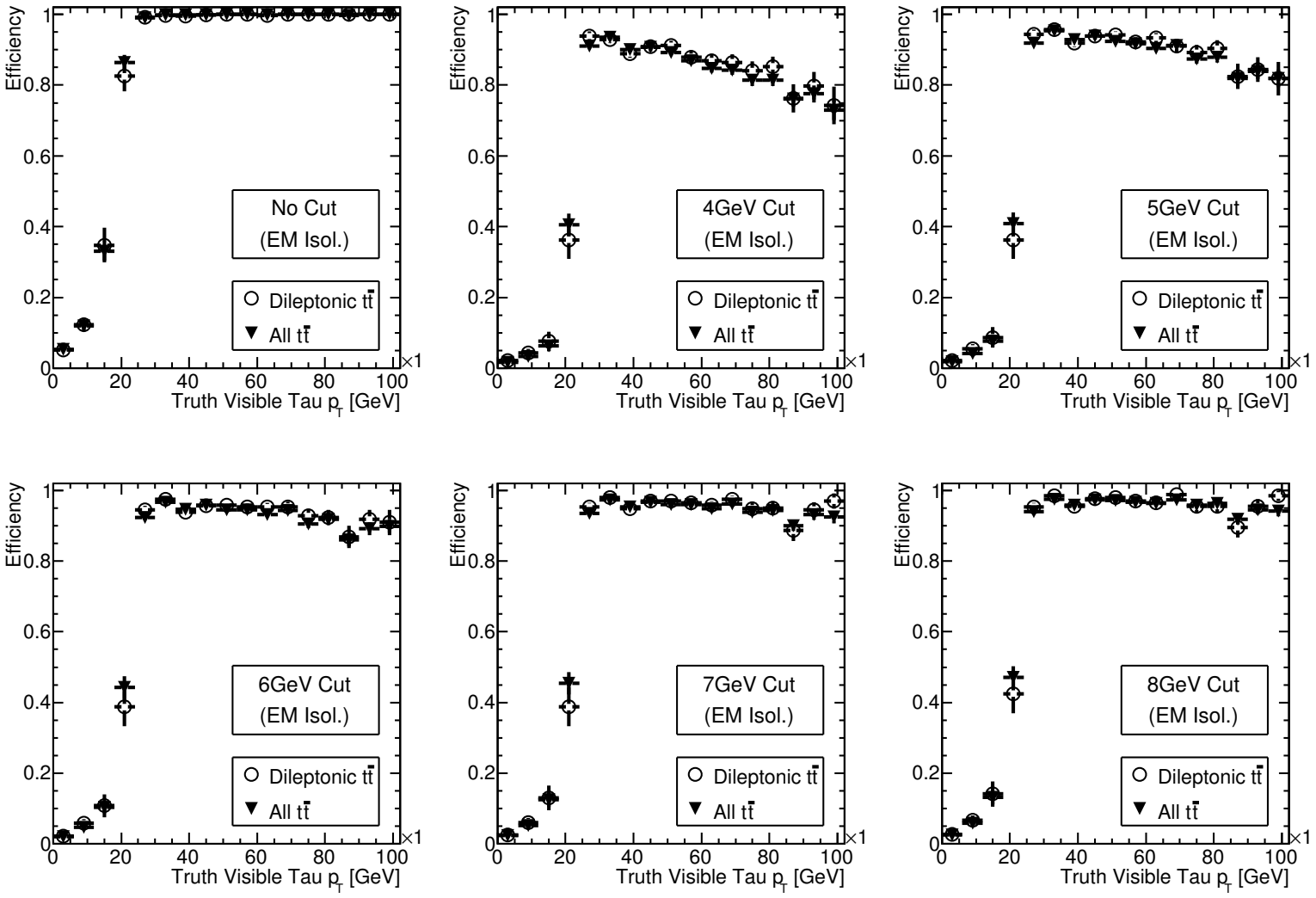

Figure 4.16: Cut by cut comparison of τ trigger efficiency versus truth visible p_{T} with EM isolation applied for dileptonic $t\bar{t}$ events and mixed semileptonic and dileptonic $t\bar{t}$ events (truth prompt taus only used for the $t\bar{t}$ sample). Plots produced for a centre of mass energy of 14 TeV.

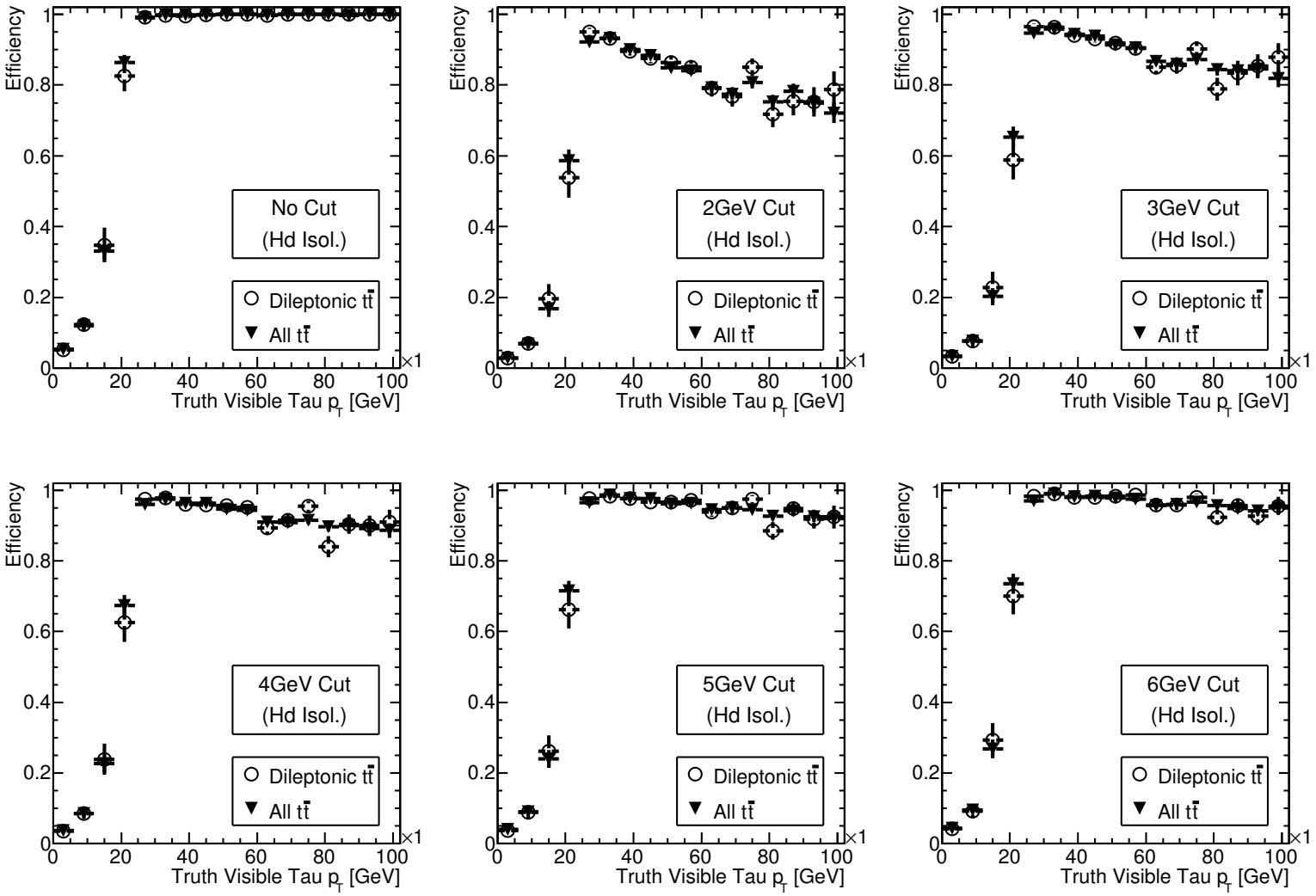

Figure 4.17: Cut by cut comparison of τ trigger efficiency versus truth visible p_{T} with EM isolation applied for dileptonic $t\bar{t}$ events and mixed semileptonic and dileptonic $t\bar{t}$ events (truth prompt taus only used for the $t\bar{t}$ sample). Plots produced for a centre of mass energy of 14 TeV.

events were used. This was the case for all values of the EM and hadronic isolation cuts. Using all the taus produced irrespective of their origin also yielded the same result. Equivalent results were also observed when using the 7 TeV $t\bar{t}$ sample.

4.4.5 Early Tau Trigger Menu

A preliminary study was carried out using the Level 1 section of a proposed 10^{31} cm^{-2} s^{-1} early data-taking trigger menu of ATLAS as it was expected to be during 2008. Only the 21 pure tau trigger items within the menu were examined. Table 4.1 shows the proposed LVL1 tau trigger items together with their corresponding cuts on the tau cluster energy and EM isolation energy where appropriate. No hadronic isolation requirement featured in the menu. Similarly, table 4.2 shows the 21 items for the whole trigger menu that contained pure tau components only at LVL1, together with their LVL1 content and prescale. All the thresholds and prescales used in this menu were based on 14 TeV Monte Carlo.

Using the same $t\bar{t}$ samples as before, the fraction of events passing each of the LVL1 tau trigger thresholds was obtained. This is illustrated in Figure 4.18 for both 14 TeV and 7 TeV, which does not take prescaling into account. As would be reasonably expected, the fractions passing the low energy thresholds are similar for the two different centre of mass energies. The acceptance of L1_TAU25 and L1_TAU40 is notably lower for the 7 TeV sample. As the turn on curves for the different trigger thresholds overlap, this is again likely to be as a result of the softening and shift in the turn on produced by the revised calibration used in the 7 TeV samples. In

Item name	TauClus[GeV]	EmIsol[GeV]
L1_TAU5	>5	Off
L1_TAU6	>6	Off
L1_TAU9I	>9	≤6
L1_TAU11I	>11	≤6
L1_TAU16I	>16	≤6
L1_TAU25	>25	Off
L1_TAU25I	>25	≤6
L1_TAU40	>40	Off

Table 4.1: LVL1 trigger items

the trigger menu used during 2010 running this was accounted for by retaining the lower thresholds studied here (L1_TAU5, L1_TAU6 and L1_TAU11I), whilst replacing L1_TAU25 and L1_TAU40 by L1_TAU20 and L1_TAU30 respectively.

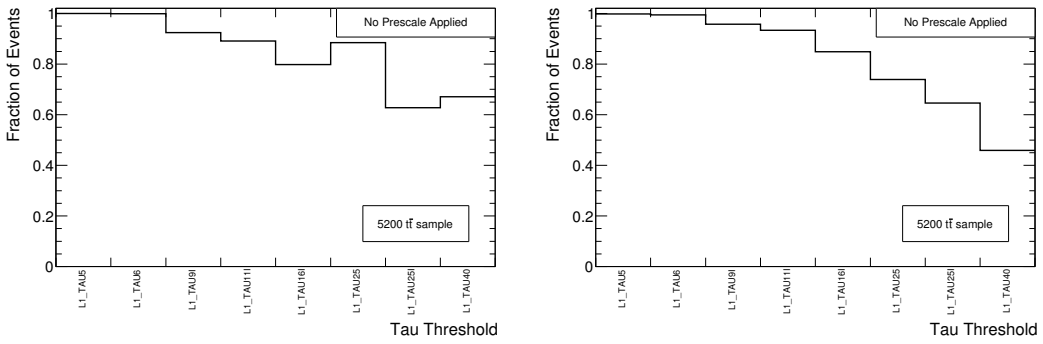

(a) 14 TeV *(b)* 7 TeV

Figure 4.18: Fraction of events passing the eight LVL1 tau thresholds when running over a mixture of dileptonic and semileptonic $t\bar{t}$ events. No prescaling has been applied

Item name	L1 Item content	L1 Prescale
tauNoCut	L1_TAU5	1×10^7
tau10	L1_TAU6	1500
tau10i	L1_TAU6	1500
tau15	L1_TAU6	1500
tau15i	L1_TAU6	1500
tau15i_PT	L1_TAU6	1500
tau20i	L1_TAU9I	1×10^6
tau25i	L1_TAU11I	1500
tau35i	L1_TAU16I	1×10^6
tau45	L1_TAU25	8
tau45i	L1_TAU25I	4
tau60	L1_TAU40	1
tau100	L1_TAU40	1
twotau15i	L1_2TAU6	100
twotau25i	L1_2TAU9I	1
twotau25i_PT	L1_2TAU9I	1
twotau35i	L1_2TAU16I	1
tau15i_tau35i	L1_2TAU6_TAU16I	1
tau15i_tau35i_PT	L1_2TAU6_TAU16I	1
tau10i_tau45	L1_2TAU6_TAU25	1
tau15i_tau45	L1_2TAU6_TAU25	1

Table 4.2: Pure tau trigger items

By looking at the number of RoIs passing each Level 1 threshold for each event, the overall fractional acceptance was deduced for the threshold combination corresponding to the Level 1 part of each tau trigger item. Acceptances were calculated both before and after the application of the appropriate Level 1 prescales, and these two cases are illustrated in Fig. 4.19 and Fig. 4.20 for the 14 and 7 TeV cases respectively. It should be noted that the prescales studied here can only be considered an example of a typical set (with large prescales for the low E_{T} items and prescale factor reducing with increasing E_{T}) as trigger menus are under constant development at ATLAS, with both thresholds and prescales evolving over time.

For both sets of plots it can be seen that when prescales are applied the minimum threshold which still accepts events at Level 1 is tau45. Any triggers which have a single LVL1 tau threshold below 25 GeV are almost completely removed by the LVL1 prescales. This emphasises the need to use combined LVL1 triggers, such as tau + missing E_{T}, when low tau thresholds are required for high luminosities. As would be expected, the items containing the higher LVL1 thresholds are less efficient for the 7 TeV events than for 14 TeV events due to the effect of the tau p_{T} spectrum.

The acceptances shown in Figures 4.18, 4.19 and 4.20 were calculated using RoI produced for all events in the $t\bar{t}$ sample known to contain a truth tau of any origin. Acceptances were also calculated for all events in the $t\bar{t}$ sample regardless of whether a truth tau was actually present. No significant alteration to the acceptance was observed for those thresholds which are unprescaled at Level 1.

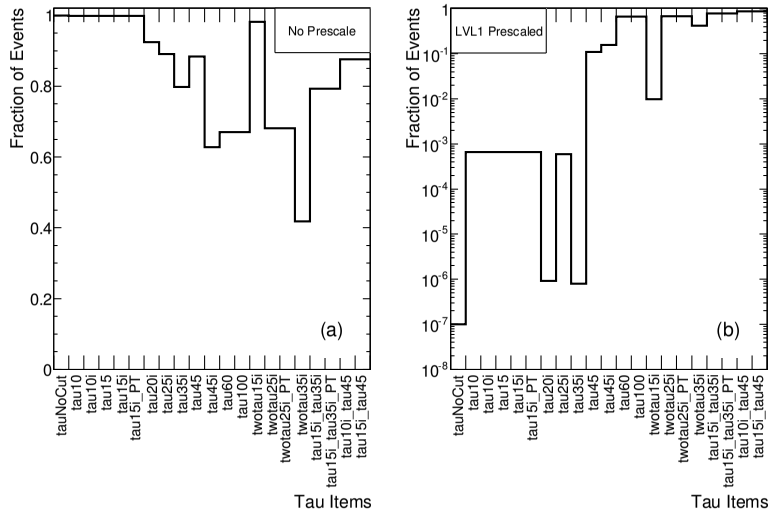

Figure 4.19: Acceptance for the Level 1 items within the proposed ATLAS 10^{31} cm^{-2} s^{-1} tau trigger menu. Plot (a) shows the acceptances before prescaling and (b) the acceptances after the application of the LVL1 prescales for a centre of mass energy of 14TeV.

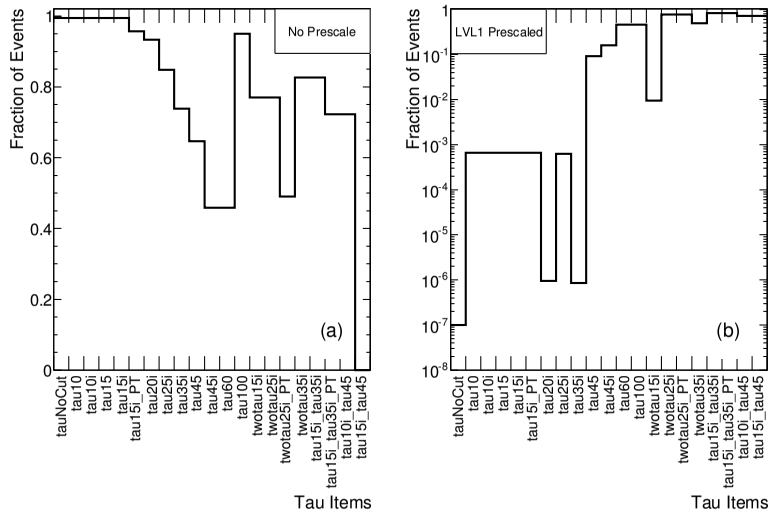

Figure 4.20: Acceptance for the Level 1 items within the proposed ATLAS 10^{31} cm^{-2} s^{-1} tau trigger menu. Plot (a) shows the acceptances before prescaling and (b) the acceptances after the application of the LVL1 prescales for a centre of mass energy of 7TeV.

4.5 Conclusions

A study into the performance of the ATLAS LVL1 tau trigger has been described using Monte Carlo truth information. Two samples were used to allow the performance in the complicated environment of $t\bar{t}$ events to be compared to that seen in clean $Z \rightarrow \tau\ \tau$ events. Performance was compared before and after the application of a series of fixed EM and hadronic isolation cuts. Using 14 TeV centre of mass energy samples produced in Athena release 12.0.6 a process dependence of the tau trigger was observed when isolation was applied. Repeating the analysis for equivalent 7 TeV centre of mass energy samples, containing a more realistic trigger simulation, in Athena release 15.6.13.7 showed this process dependence to have been almost completely removed for the same threshold and isolation settings. It was deduced that in such a scenario a measurement of the tau trigger efficiency from data (via tag and probe techniques) for Z $\rightarrow \tau\ \tau$ events could provide a good estimate of the LVL1 tau trigger efficiency for prompt taus in $t\bar{t}$ events. Similarly, a measure of the efficiency in dileptonic $t\bar{t}$ events, where a tag and probe technique could be used, was seen to provide a way of estimating the LVL1 efficiency for taus in all $t\bar{t}$ events. Finally, an example of a typical ATLAS tau trigger menu was examined for both centre of mass energies, revealing the need to use combined triggers to select low energy taus at LVL1 at the luminosities the LHC is expected to reach in 2011-2012.

Chapter 5

Hadronic Tau Identification for Early ATLAS Data

5.1 Introduction

Contained within this chapter are the details of an investigation into the various possibilities for identification of hadronic tau decays in early ATLAS data. The ATLAS tau physics working group designated a series of approved 'Safe Cuts' intended to identify such taus based on a number of either calorimeter only or combined calorimeter and tracking variables [47]. These cuts had been optimised on a comparatively clean signal sample. The work covered here therefore evaluates the suitability of the cuts for use in complicated top events, and compares their performance to two different single variable cuts.

5.2 Good Tau Selection

Before considering the details of making a tau selection, it is necessary to note which of the tau decays can be realistically expected to be observed as distinct objects with the ATLAS detector. When a tau decays to leptons, the only difference to direct lepton production is the presence of the two neutrinos as detailed in 1.7.2. As the neutrinos leave no signature in the ATLAS detector other than contributing to a level of missing energy, which is expected to be present already in many interesting LHC physics signatures, it is generally considered unrealistic to identify the leptonic tau decay modes. The tau to lepton decay is therefore accounted for as part of the electron and muon branching fractions for a given decay. For example, the decay $t \rightarrow W \rightarrow \tau \rightarrow l$ is included in the case $t \rightarrow W \rightarrow l$ in $t\bar{t}$ cross-section measurements [48].

Tau identification in ATLAS concentrates on identifying the hadronic decay modes. The key is to distinguish jets originating from a hadronically decaying tau from those originating from quarks or QCD. In a practical sense, this relies on identifying taus as narrow jets with a low track multipicity. Jet width is usually determined in two ways. The first involves measuring the spread of the shower the jet produces in the detector calorimeter, either in a particular layer, or by combining different measurements across the various calorimeter layers. Alternatively, jet isolation can be used. Here typically a cone is defined of a chosen width to represent the core region of the jet (where the majority of the energy would be expected to lie). A second isolation cone (or other chosen region) is then defined around the jet core,

as shown in Fig. 5.1. By measuring the ratio of the energy found in the two cones a judgement can be made on the jet width, with wider jets having larger fractions of their total energy found in the isolation cone. Jet track multiplicity comes simply from looking at the number of charged tracks assigned to the jet.

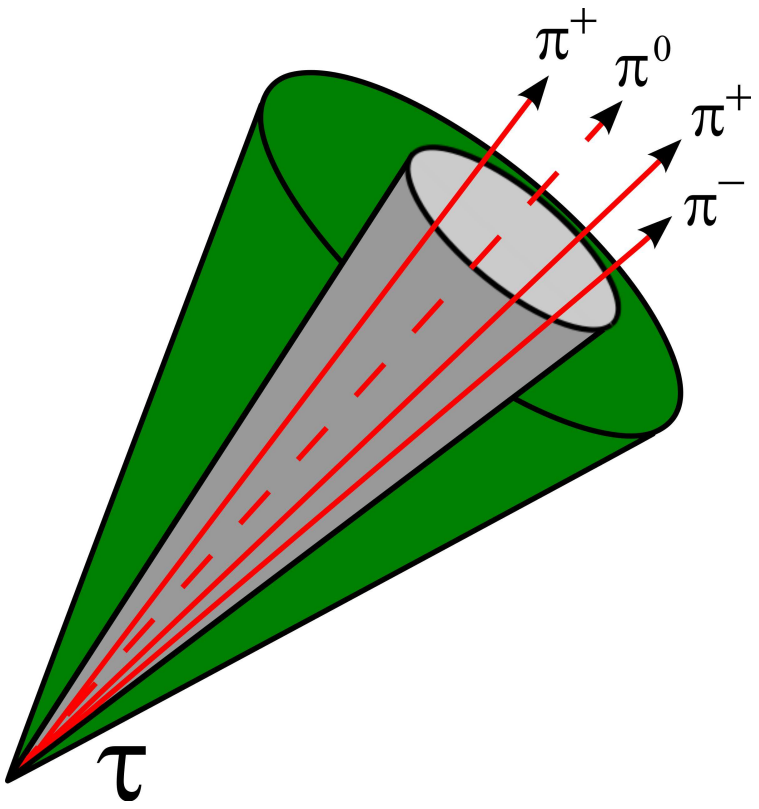

Figure 5.1: Hadronic tau decays produce a jet with an energy cluster which is typically narrower than an equivalent QCD jet. Tau candidates can in principle be distinguished by measuring the width of the shower, the energy in some defined isolation region around the jet, and by the track multiplicity within the jet

The key of such a hadronic tau selection is to ensure a strong rejection against QCD jets, while retaining the maximum number of tau candidates. In order to ensure the best possible separation between taus and background jets, higher multiplicity tau decays of five prongs and above are disregarded. Furthermore, the 1-Prong and

3-Prong modes are also often considered separately, and a wide range of different calorimeter and track variables are usually combined together in each case (often using multivariant techniques) in order to produce the best discrimination between signal taus and background jets.

5.3 Tau Reconstruction in ATLAS

The ATLAS experiment uses two different methods for reconstruction of possible hadronic tau candidates. One algorithm starts from tracking information combined with quality cuts, while the second builds candidates from calorimeter clusters via a cone algorithm [49]. Historically the two tau reconstruction algorithms were distinct from each other, with the possiblity that the same tau could be reconstructed via both algorithms independently. The primarily calorimeter based algorithm was known as TauRec and the lead track based algorithm Tau1P3P [50]. More recently the two tau reconstructions have been combined from release 14.0.0 of the ATLAS reconstruction software [51]. One set of reconstructed tau candidates are therefore now produced, but with each tau candidate flagged as being either 'calo-seeded' (ex. TauRec), 'track-seeded' (ex. Tau1P3P) or 'calo-and-track-seeded'. The 'calo-seeded' candidates are devised from calorimeter topological clusters (these sum neighbouring calorimeter cells, based on the significance of the energy found within each cell [52]) with $E_{\mathrm{T}} > 10$ GeV [47] while the 'track-seeded' candidates originate from a track possessing $p_{\mathrm{T}} > 10$ GeV [49].

5.4 Hadronic Tau Identification by Safe Cuts

5.4.1 Safe Cuts

An assortment of different techniques has been developed for tau identification with the ATLAS detector. Many of these use large numbers of variables combined and tuned via multivariant techniques as summarised in [49]. In early ATLAS comissioning and running it is expected that the inputs into these tools will not be fully optimised, particularly with regards to tracking variables. As such a set of designated 'Safe Cuts' have been developed by the ATLAS tau physics working group for hadronic tau identification. These are based on a small number of so called 'robust variables' [47] which are expected to be comparatively well understood in early LHC running.

The safe cuts were optimised using ATLAS datasets produced by the Pythia event generator with a centre-of-mass energy of 14 TeV [47]. A relatively clean signal sample of taus was used in the form of two datasets combined together, the first being $Z \rightarrow \tau\tau$ and the second $bbA \rightarrow bb\tau\tau$ (with mA =800 GeV) [47], while a background was provided via dijet samples in an approximate equivalent p_{T} region [47].

Two sets of safe cuts were provided by the tau working group. The first used four calorimeter variables only and was considered the more robust approach. The second set used a combination of calorimeter and track variables. In the case of the former, the cuts were applicable to any calorimeter seeded tau candidates, while for the latter the cuts could be applied to the calorimeter and track seeded taus only [47].

5.4.2 Safe Variables

The calorimeter only safe cuts used a combination of the variables given below [53] [54];

- Combined radius in whole EM calorimeter (EmRadius)
- Isolation fraction in whole calorimeter (IsolationFraction)
- Width in the strip layer of calorimeter (stripWidth2)
- Ratio of EM to total calorimeter energy ($E_{\mathrm{T}}(\mathrm{EM})/E_{\mathrm{T}}$)

The combined calorimeter and track selection safe cuts relied on a total of nine variables [53] [54];

- The existing four calorimeter only variables listed above
- Angular spread of tracks, weighted by transverse momentum in multi-track candidates (RWidth2Trk3P)
- Ratio of the (E_{T}) to the (p_{T}) of the lead track in the candidate (etOverPtLeadTrack)
- Ratio of the summed hadronic E_{T} to the summed p_{T} of the (up to three) highest p_{T} tracks (etHadCalib/ptTrack1 + 2 + 3)
- Ratio of the summed EM E_{T} to the summed p_{T} of the (up to three) highest p_{T} tracks (etEMCalib/ptTrack1 + 2 + 3)

- Ratio of the summed p_{T} of the (up to three) highest p_{T} tracks to the total combined calibrated summed EM and hadronic E_{T} (ptTrack1+2+3/(etEMCalib1+2 + 3etHadCalib))

5.4.3 Calorimeter Only Variable Definitions

Depending on the seed of the tau candidate, the variables possessed by the object were defined differently. As the safe cuts were designed for the calo-seeded taus, the calorimeter only safe cut variables were therefore defined in accordance with this. The first three variables were taken directly from the reconstructed AOD container and are given as:

- EmRadius : Uncalibrated E_{T} weighted radius in the Presampler + EM1 + EM2 within dR < 0.4
- IsolationFraction : Ratio of the uncalibrated E_{T} of cells within $0.1 <$ dR < 0.2 and cells within $0 <$ dR < 0.4
- stripWidth2 : Uncalibrated E_{T} weighted width in the strip layer within dR < 0.4

The fourth variable was the ratio of the EM to the total calorimeter energy which was calculated by;

$$\text{Energy Ratio} = \frac{\text{etEMCalib}}{\text{etEMCalib} + \text{etHadCalib}} \tag{5.1}$$

where etEMCalib and etHadCalib are the calibrated EM E_{T} and hadronic E_{T} respectively. Fig. 5.2 illustrates the distributions produced for these four variables in $t\bar{t}$ events, plotted for both reconstruced tau candidates matched to (1-Prong and 3-Prong) Monte Carlo truth taus (black) and fake candidates which are therefore not matched to truth (in red). The matching definition used to make the plots is described in 5.4.4. As can be seen, the separation between the good and fake distributions is limited, with EmRadius and IsolationFraction appearing the better discriminators.

5.4.4 Safe Cut Optimisation

Development of the two sets of safe cuts has been fully described elsewhere [53] [54] and so will not be described here. For both the calo. only and the calorimeter plus track scenarios the same basic technique was used. Using a generic algorithm to separate the signal and the background distributions [53], cuts were produced separately for one and three prong taus and in 5 discrete p_{T} bins of 10-25 GeV, 25-45 GeV, 45-70 GeV, 70-100 GeV and >100 GeV [47]. Loose, medium and tight tau selections were defined as producing signal selection efficiencies of 30%, 50% and 70% respectively, where the signal selection efficiency was defined as in equation 5.2 [47], with $N^{\mathrm{Pass}}_{\mathrm{Matched}}$ being the number of matched reconstructed n-prong tau candidates passing the cuts and $N^{\mathrm{Total}}_{\mathrm{MC}}$ the number of n-prong Monte Carlo tau leptons within the p_{T} range with stable daughters.

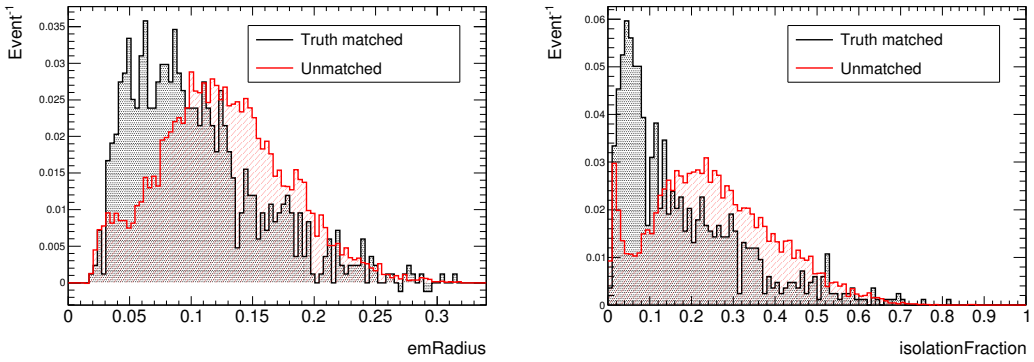

(a) EmRadius

(b) IsolationFraction

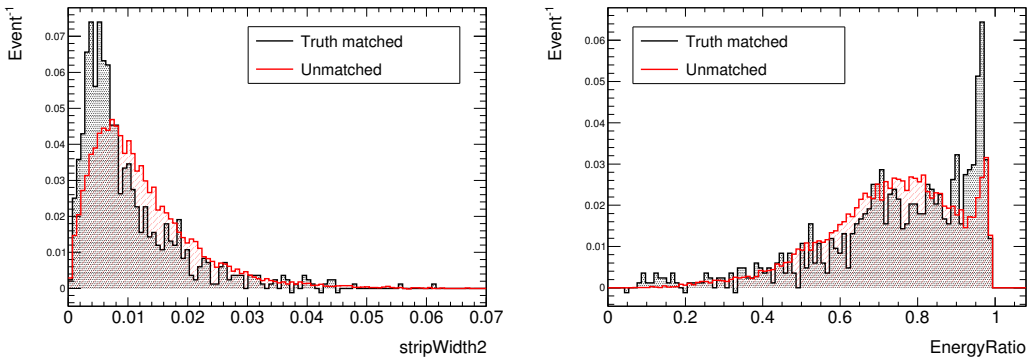

(c) StripWidth2

(d) Energy Ratio

Figure 5.2: Distribution of good and fake hadronic taus, normalised to unit area, for the four variables of the calorimeter only 'safe cuts'. In these plots good taus are matched to truth with dR < 0.2, fakes have dR > 0.5 from the nearest truth tau

$$\epsilon_{\tau}^{\mathrm{n-prong}} = \frac{N_{\mathrm{Matched}}^{\mathrm{Pass}}}{N_{\mathrm{MC}}^{\mathrm{Total}}} \tag{5.2}$$

Here 'matched' means that the separation between the reconstructed tau candidate and the true hadronic tau has a ΔR value smaller than 0.2, while the hadronic Monte Carlo tau definition excluded those decaying to final state kaons (although the effect of these being allowed was checked and seen to be tiny). The set of calo. only safe cuts evaluated within this chapter are given in Appendix A, with tables A.1 and A.2 showing the cut values applied for one prong and three prong selections respectively.

5.5 Evaluation of Calo. Only Safe Cut Efficiencies in $t\bar{t}$ Events

The remainder of this chapter will concentrate on an evaluation of the performance of the calorimeter only safe cuts with respect to the selection of hadronic 1 and 3 prong taus in $t\bar{t}$ semileptonic and dileptonic events for an LHC centre-of-mass energy of 10 TeV. The study was carried out using release 14.5.0 of the ATLAS Athena software and Monte Carlo simulated data samples produced in release 14.2.25.6 as part of the mc08 collection of 10 TeV samples. Calorimeter only cuts were considered for two reasons. Firstly, cuts were being examined with the intention to use them in the top physics area for the first year of ATLAS data taking. Consequently, the extra simplicity of the calorimeter only cuts was preferable. Secondly, with the merging of the two tau reconstruction types as discussed in section 5.3, some of the

tracking variables used in the calorimeter and track safe cuts were to be replaced from release 15 of the ATLAS software [54]. Although this analysis was carried out in an earlier software release, as the first ATLAS collision data was to be produced in release 15 it was sensible to only consider a selection that could be carried forwards unchanged.

5.5.1 Efficiency with respect to Monte Carlo

The first stage of the study focused on a direct comparison of the signal selection efficiency for the safe cuts in $t\bar{t}$ [1] events relative to that produced for a combination of $Z \rightarrow \tau\tau$ [2] and $bbA \rightarrow bb\tau\tau$ (mA =800 GeV) [3] events. The purpose of this was to evaluate how the hadronic tau selection efficiency was affected by the move to a more jet dominated environment and to establish whether it would be realistic to use the safe cuts for tau identification in $t\bar{t}$ events. The combination of the latter two datasets was intended to match as far as possible for 10 TeV samples the signal datasets used at 14 TeV to optimise the safe cuts [47]. At all stages each set of cuts was applied manually by hand for each of the safe cut p_{T} bins, while for all three samples sufficient dataset sizes were used to give negligible errors on the selection efficiencies. For the $t\bar{t}$ and $Z \rightarrow \tau\tau$ samples 400,000 events of each were used, while for the $bbA \rightarrow bb\tau\tau$ case the entire available dataset was processed comprising a total of 90,400 events.

[1] Sample mc08.105200.T1_McAtNlo_Jimmy.merge.AOD.e357_s462_r635_t53

[2] Sample mc08.106052.PythiaZtautau.merge.AOD.e347_s462_r635_t53

[3] Sample mc08.106573.PythiabbAtautauMA800TB35.merge.AOD.e347_s462_r635_t53

As an initial comparison, the tau selection efficiency in the samples was calculated as per that given in equation 5.2 as used to optimise the safe cuts. Tau candidates were considered to be well matched to truth hadronic taus if they produced a ΔR value less than 0.2. For combining the $Z \rightarrow \tau\tau$ and $bbA \rightarrow bb\tau\tau$ results the efficiency was formed by requiring both the denominator and numerator of the calculation to be the sum of the number of events from the two samples. Fig. 5.3 shows the resulting tau selection efficiency for the $t\bar{t}$ sample and mixed $Z \rightarrow \tau\tau$ and $bbA \rightarrow bb\tau\tau$ sample. The efficiency was calculated separately for each of the five p_{T} bins (with the bins defined in term of the truth visible p_{T}) and is shown independently for 1-Prong and 3-Prong taus as well as being divided into loose, medium and tight selections.

By examining the plots it can be seen that for the efficiency definition used the values produced for the $t\bar{t}$ sample are slightly smaller (typically 5-10%) than for the combined $Z \rightarrow \tau\tau$ and $bbA \rightarrow bb\tau\tau$ sample. An exception is the >100 GeV bin for the medium and tight cases, where the control sample efficiency is noteably larger, however this is the region where the $bbA \rightarrow bb\tau\tau$ events start to dominate the combined sample. There will be very few taus produced in this bin by $t\bar{t}$ events in early 7 TeV ATLAS data, and those that are can only be produced by highly boosted top quarks. This aside, the patterns match well for the two samples thoughout for both 1-Prong and 3-Prong taus and for each of the cut levels. The cut hierarchy also remains correct for the $t\bar{t}$ sample with the loose cut efficiency higher than the medium, which is in turn larger than for the loose selection. This is true for all the p_{T} bins in both 1-Prong and 3-Prong cases.

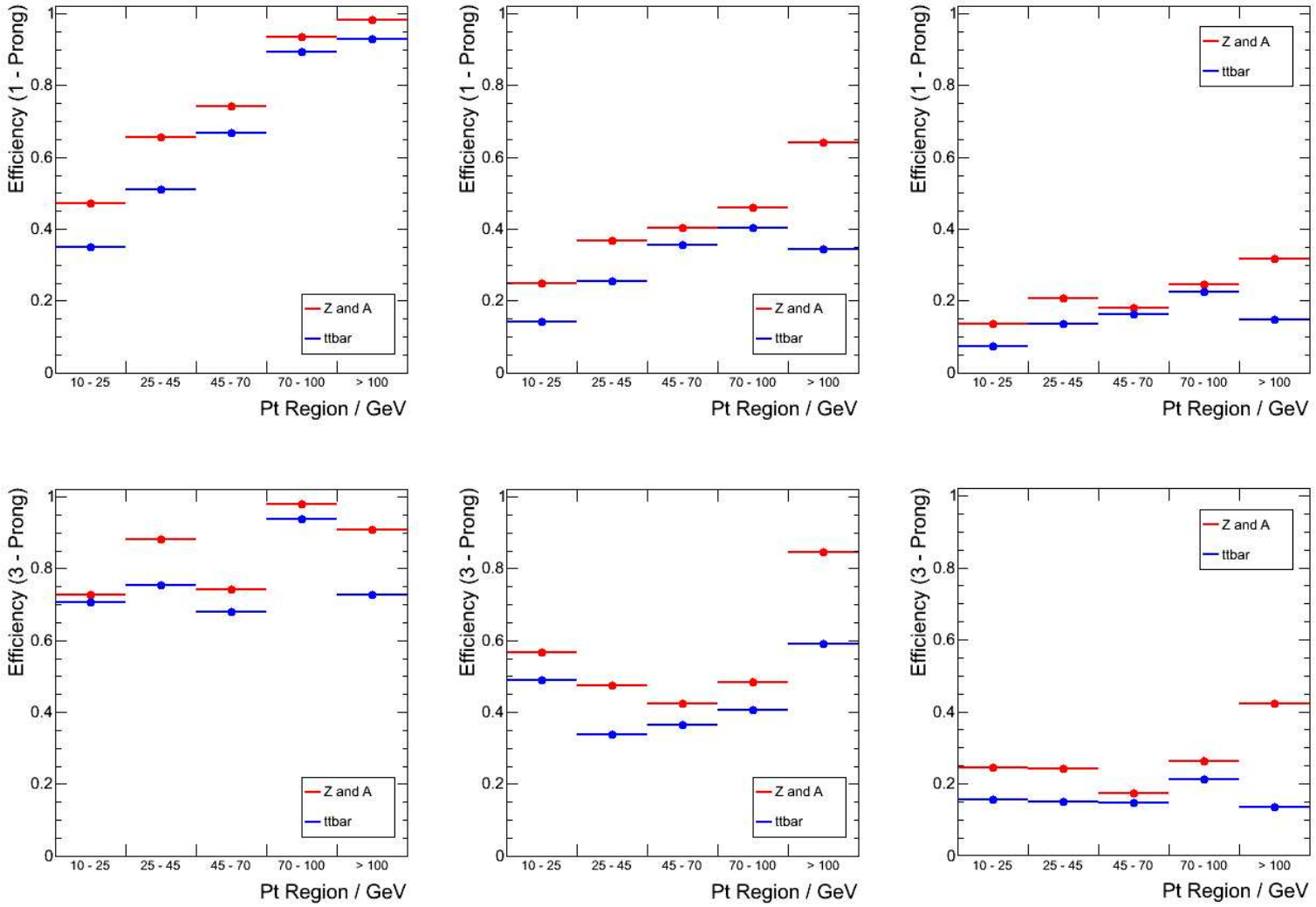

Figure 5.3: Selection efficiency comparison between $t\bar{t}$ and combined $Z \rightarrow \tau\ \tau$ and $A \rightarrow \tau\ \tau$ events for the calorimeter only tau safe cuts. Comparisons are split into loose medium and tight cuts (shown by columns running from left to right), and 1-Prong and 3-Prong hadronic taus

5.5.2 Efficiency with respect to Reconstructed Taus

While defining the efficiency as per 5.5.1 is interesting because it shows how the overall tau selection performs, it is not necessarily the best way of examining the performance of the tau selection cuts themselves. This is because the cut efficiency and the reconstruction efficiency are folded in together (the reconstruction efficiency being the probability for a real tau to pass the loose criteria used to define a tau candidate and so be found in the tau container for the event). To examine the cut efficiency alone (which also allows for easier comparison with other techniques as discussed in section 5.7) it is possible to define the signal selection efficiency in a different way, via equation 5.3. Here $N^{\text{Pass}}_{\text{Matched}}$ is the number of matched reconstructed n-prong tau candidates passing the cuts (as before), while $N^{\text{Total}}_{\text{Matched}}$ is the number of matched reconstructed n-prong tau candidates present before the cuts.

$$\epsilon_{\tau}^{\text{n-prong}} = \frac{N^{\text{Pass}}_{\text{Matched}}}{N^{\text{Total}}_{\text{Matched}}} \tag{5.3}$$

The same procedure as in section 5.5.1 was followed to compare the $t\bar{t}$ signal selection efficiency to that for the combined $Z \rightarrow \tau\tau$ and $bbA \rightarrow bb\tau\tau$ sample separately for 1-Prong and 3-Prong taus for the same five p_{T} bins, but where the efficiency was now as defined in 5.3. In addition, while the matched Monte Carlo truth taus were still used to define the prong of the candidate, the p_{T} binning was now based on the reconstructed p_{T} of the tau candidates. Table 5.1 shows the resulting values for 1-Prong taus whilst table 5.2 shows the equivalent results for 3-Prong taus.

Examining the two tables and comparing to Fig. 5.3, it can be seen that in certain p_{T} bins the safe cuts are actually carrying out little of the discrimination between the actual and fake taus; for example the 1-Prong >100 GeV bin where the loose efficiency is 0.99 and 0.98 for the two samples respectively (although the combined cut and reconstruction efficiency is also very high). In other areas the cut efficiencies relative to the reconstruction are much lower and so the safe cuts are providing a larger proportion of the discrimination, as demonstrated by the 1-Prong 10-25 GeV medium values.

Comparing the efficiencies, with respect to the reconstructed taus, for $t\bar{t}$ events versus those for the combined samples a similar pattern is present to that observed in 5.5.1. For the 45-70 and 70-100 GeV bins the $t\bar{t}$ selection efficiency is seen to be approximately 10% lower than for the combined control sample for all cut levels and for both for 1-Prong and 3-Prong taus. In the other p_{T} regions the performance is not quite as stable. As would be expected the efficiencies for $t\bar{t}$ most closely compare with those for the cleaner sample in the loose cuts, with the $t\bar{t}$ performance dropping as the cut level is tightened. Looking at the 10-25, 25-45 and >100 GeV bins for the 3-Prong case in table 5.2, it can be seen that the efficiency for the tight selection is approximately 10-15% lower than for the medium selection, which is then lower than for the loose selection by approximately the same amount. The loose selection for the two low p_{T} bins is again seen to be approximately 5-10% lower for $t\bar{t}$ than for the clean sample, which increases to around 15% for the >100 GeV bin. By contrast the 1-Prong case does not behave in such a predictable manner. Examining the 25-45 GeV bin the loose cut efficiency for the $t\bar{t}$ sample is only

approximately 15% lower than for the control sample. Performance for the medium and tight efficiencies is then approximately a further 10% worse for the $t\bar{t}$ compared to the combined $Z \rightarrow \tau\tau$ and $bbA \rightarrow bb\tau\tau$ sample. The same pattern is repeated for the 10-25 GeV bin but with the starting point for the loose selection having the $t\bar{t}$ efficiency 30% lower than for $Z \rightarrow \tau\tau$ and $bbA \rightarrow bb\tau\tau$. In the >100 GeV bin the performance is practically identical for the two samples when looking at the loose selection, with the $t\bar{t}$ falling away to 60% and 50% of the $Z \rightarrow \tau\tau$ and $bbA \rightarrow bb\tau\tau$ effciency for the medium and tight cases.

For the purpose of top physics, the bins which are the most important are those covering the p_{T} range from 25-100 GeV. Taking the figures in the two tables as a whole, it can be seen that the performance of the safe cut efficiency with respect to the reconstruction for the $t\bar{t}$ sample holds up well compared to the $Z \rightarrow \tau\tau$ and $bbA \rightarrow bb\tau\tau$ sample in this region.

p_T[GeV]	CutLevel	Tau efficiency for Z and A	Tau efficiency for $t\bar{t}$	Efficiency Ratio
		TauRec Before/After	TauRec Before/After	
10-25	Loose	0.69	0.48	0.70
	Medium	0.36	0.19	0.53
	Tight	0.20	0.10	0.50
25-45	Loose	0.73	0.60	0.82
	Medium	0.41	0.30	0.73
	Tight	0.23	0.16	0.69
45-70	Loose	0.78	0.73	0.93
	Medium	0.43	0.39	0.91
	Tight	0.19	0.18	0.93
70-100	Loose	0.96	0.95	0.98
	Medium	0.48	0.43	0.90
	Tight	0.25	0.24	0.94
>100	Loose	0.99	0.98	0.99
	Medium	0.63	0.36	0.58
	Tight	0.32	0.16	0.49

Table 5.1: Hadronic 1-Prong tau selection efficiency with respect to reconstructed taus. Efficiencies are shown for a combined sample of Z $\rightarrow \tau\ \tau$ and A $\rightarrow \tau\ \tau$ events and for $t\bar{t}$ events

p_T[GeV]	CutLevel	Tau efficiency for Z and A	Tau efficiency for $t\bar{t}$	Efficiency Ratio
		TauRec Before/After	TauRec Before/After	
10-25	Loose	0.95	0.92	0.97
	Medium	0.74	0.64	0.86
	Tight	0.32	0.20	0.64
25-45	Loose	0.89	0.84	0.93
	Medium	0.48	0.37	0.77
	Tight	0.26	0.17	0.64
45-70	Loose	0.75	0.72	0.96
	Medium	0.43	0.39	0.90
	Tight	0.18	0.16	0.89
70-100	Loose	0.99	0.97	0.99
	Medium	0.49	0.42	0.86
	Tight	0.27	0.22	0.82
>100	Loose	0.91	0.75	0.83
	Medium	0.85	0.61	0.72
	Tight	0.36	0.14	0.39

Table 5.2: Hadronic 3-Prong tau selection efficiency with respect to reconstructed taus. Efficiencies are shown for a combined sample of $Z \rightarrow \tau\ \tau$ and $A \rightarrow \tau\ \tau$ events and for $t\bar{t}$ events

Background Rejection Factor

When considering the cut performance relative to the reconstruction, it is also possible to obtain a measure of the rejection of the fake taus contained within a given sample. A rejection efficiency can be defined as per equation 5.4, from which a rejection factor can then be calculated by equation 5.5. In the former, $N^{\text{Pass}}_{\text{Unmatched}}$ is the number of reconstructed candidates not matched to an n-prong Monte Carlo tau remaining after the cuts, whereas $N^{\text{Total}}_{\text{Unmatched}}$ is the number of reconstructed n-prong candiates not matched to an n-prong Monte Carlo tau present before the cuts were applied.

$$\epsilon^{\text{n-prong}}_{\text{Fake }\tau} = \frac{N^{\text{Pass}}_{\text{Unmatched}}}{N^{\text{Total}}_{\text{Unmatched}}} \tag{5.4}$$

$$\text{RejectionFactor} = \frac{1}{\epsilon^{\text{n-prong}}_{\text{Fake }\tau}} \tag{5.5}$$

It is possible to calculate the rejection for any number of different samples providing a source of fake taus. For the purpose of this study, where the aim was identifying taus in $t\bar{t}$ events, the internal fakes within the $t\bar{t}$ sample were used as background. Again using the calorimeter only safe cuts, rejection factors were calculated for the $t\bar{t}$ sample. The same five p_{T} bins were used as in 5.5.2 with numbers produced separately for 1-Prong and 3-Prong taus for the loose, medium and tight selections. The resulting rejection factors are shown in table 5.3 for both the 1-Prong and 3-Prong taus.

Examining the table, it can be seen that in general the rejection achieved is higher in

the 1-Prong case than in the 3-Prong case. Moving through the cut levels from loose to medium to tight, the rejection increases as would be expected for both prongs. In addition, as the cuts are tightened, the rejection for the 1-Prong $t\bar{t}$ events increases slightly relative to that for the 3-Prong.

p_T[GeV]	Cut Level	Rejection for $t\bar{t}$	
		1-Prong Before/After	3-Prong Before/After
10-25	Loose	2.86	1.15
	Medium	7.92	1.64
	Tight	14.57	3.77
25-45	Loose	5.21	1.65
	Medium	15.88	4.97
	Tight	26.41	9.69
45-70	Loose	6.68	2.78
	Medium	24.27	9.82
	Tight	42.01	21.05
70-100	Loose	1.68	1.23
	Medium	32.90	14.56
	Tight	44.68	26.16
>100	Loose	1.11	8.76
	Medium	51.48	13.74
	Tight	77.55	62.08

Table 5.3: Hadronic 1-Prong and 3-Prong jet rejection factors for inter sample background events in $t\bar{t}$ events

Significance in Top Events

A further examination of the performance of the safe cuts in the $t\bar{t}$ sample can be made by defining a significance. This was calculated via equation 5.6 where $N^{\text{Pass}}_{\text{Matched}}$ and $N^{\text{Pass}}_{\text{Unmatched}}$ were as defined previously.

$$\text{Significance} = \frac{N^{\text{Pass}}_{\text{Matched}}}{\sqrt{(N^{\text{Pass}}_{\text{Matched}}) + (N^{\text{Pass}}_{\text{Unmatched}})}} \tag{5.6}$$

The significance was calculated for the arbitrary sample size of 400,000 events and considered only the 'in sample' background provided by the possible fake taus within the $t\bar{t}$ events. Nevertheless, examining the values shown in table 5.4 it can be seen that, whilst tightening the safe cut level increases the background jet rejection as described in 5.5.2, the corresponding drop in the tau selection efficiency is sufficienctly large that proportion of signal to background in the sample drops. The only exception is the medium cut for 1 and 3-Prong taus in the 70-100 GeV bin, which has a higher significance than the loose cut. Significance remains lower for the tight cut than for the medium cut in this bin however. As an overall consequence, depending on the size of the data sample available, it may be preferable to run a looser selection than may be optimal for background rejection in order to retain a greater proportion of the real taus in $t\bar{t}$ events.

p_{T}[GeV]	Cut Level	Significance	
		1-Prong	3-Prong
10-25	Loose	36.60	24.59
	Medium	24.43	20.34
	Tight	17.21	10.00
25-45	Loose	69.01	33.64
	Medium	54.91	25.17
	Tight	38.72	15.99
45-70	Loose	78.33	31.69
	Medium	65.94	28.56
	Tight	42.67	17.45
70-100	Loose	45.45	22.44
	Medium	53.32	25.02
	Tight	38.32	17.71
>100	Loose	31.86	26.62
	Medium	41.05	25.21
	Tight	25.27	12.19

Table 5.4: Significance values in $t\bar{t}$ events of the 1-Prong and 3-Prong hadronic safe cut selections

5.6 Calorimeter Only Safe Cut Correlations (Top Events)

As was described in 5.4.1 the calorimeter only safe cuts used four variables, of which EmRadius, IsolationFraction and stripWidth2 each provide a measurement of the width of the calorimeter cluster. The correlations between the four variables of the calorimeter only safe cuts were examined for both real and fake taus in the $t\bar{t}$ sample.

As previously, good taus were identified by requiring that they were matched to a truth 1-Prong or 3-Prong hadronic tau with a ΔR value smaller than 0.2, with the prong being allocated based on the truth tau. Correlations were examined for all six combinations of the four variables and separately for the 1-Prong good taus, 3-Prong good taus and the inter-sample background fakes. The resulting distributions are shown by figures 5.4, 5.5 and 5.6 respectively. From examining the plots it is apparent that there is a significant correlation between EmRadius and IsolationFraction for both good and fake taus. Clear correlations are also visible between EmRadius and StripWidth2, and likewise IsolationFraction and StripWidth2. Although it is not possible to observe a clear correlation in the plots which contain the EnergyRatio, it is apparent that the distribution is principally enhanced for values of the energy ratio close to 1 and small values of the other variable.

Considering the 1-Prong and 3-Prong 'signal' tau plots, the distributions are seen to take a similar shape, but with events concentrated at smaller values of EmRadius and IsolationFraction in the case of the 1-Prong taus. When these are compared

to the plots for the fake taus, for the EmRadius versus IsolationFraction plot the fake taus are seen to be concentrated at much larger values than for the 1-Prong good taus, with the 3-Prong good taus in between. Such a clear trend is not seen in the other distributions, therefore loosely suggesting that EmRadius and, to a lesser extent, IsolationFraction are the two strongest discriminants of the four variables.

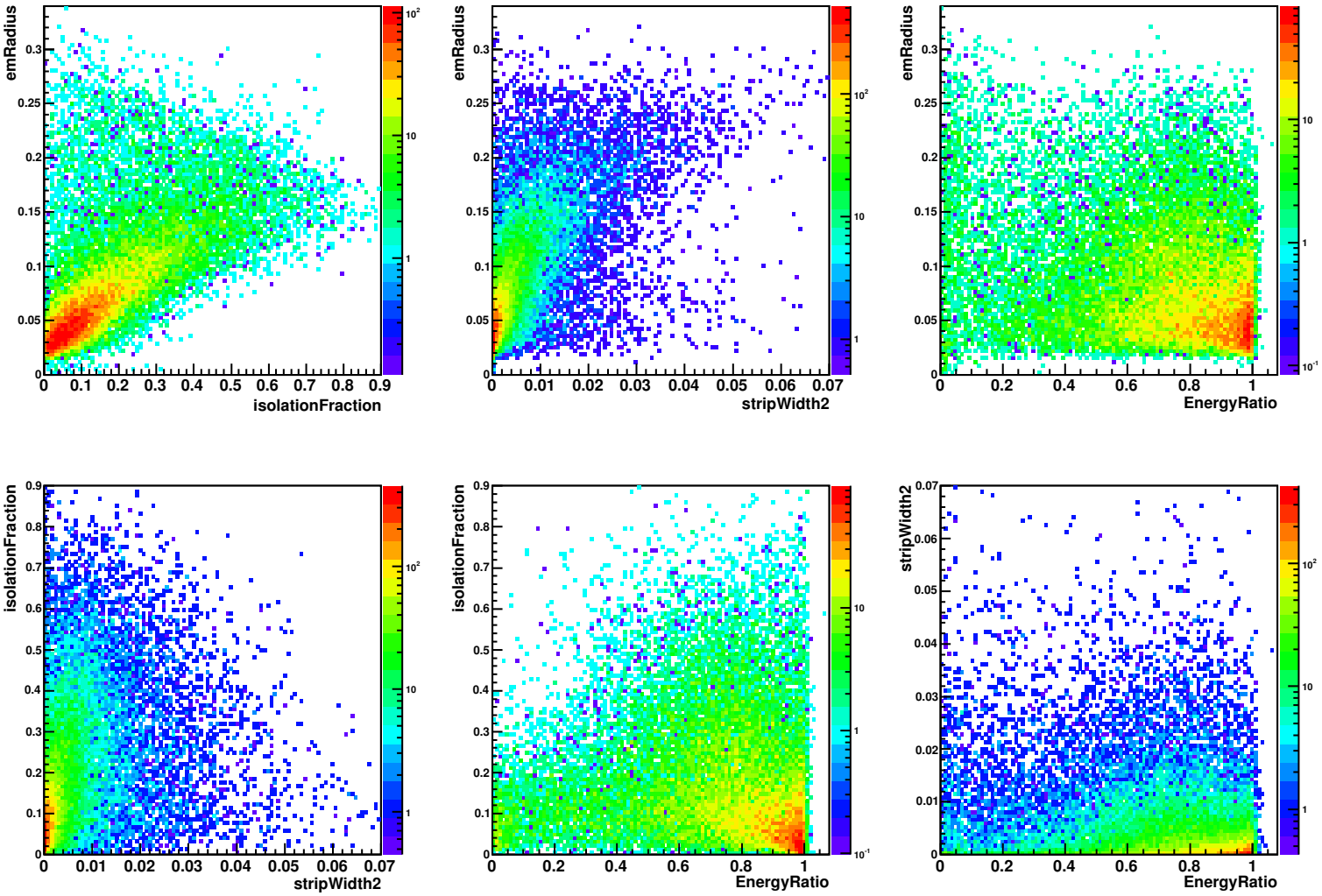

Figure 5.4: Correlations between the calorimeter only safe cut variables for reconstructed taus matched to 1-Prong hadronic MC taus (with $\triangle R < 0.2$) for the $t\bar{t}$ sample

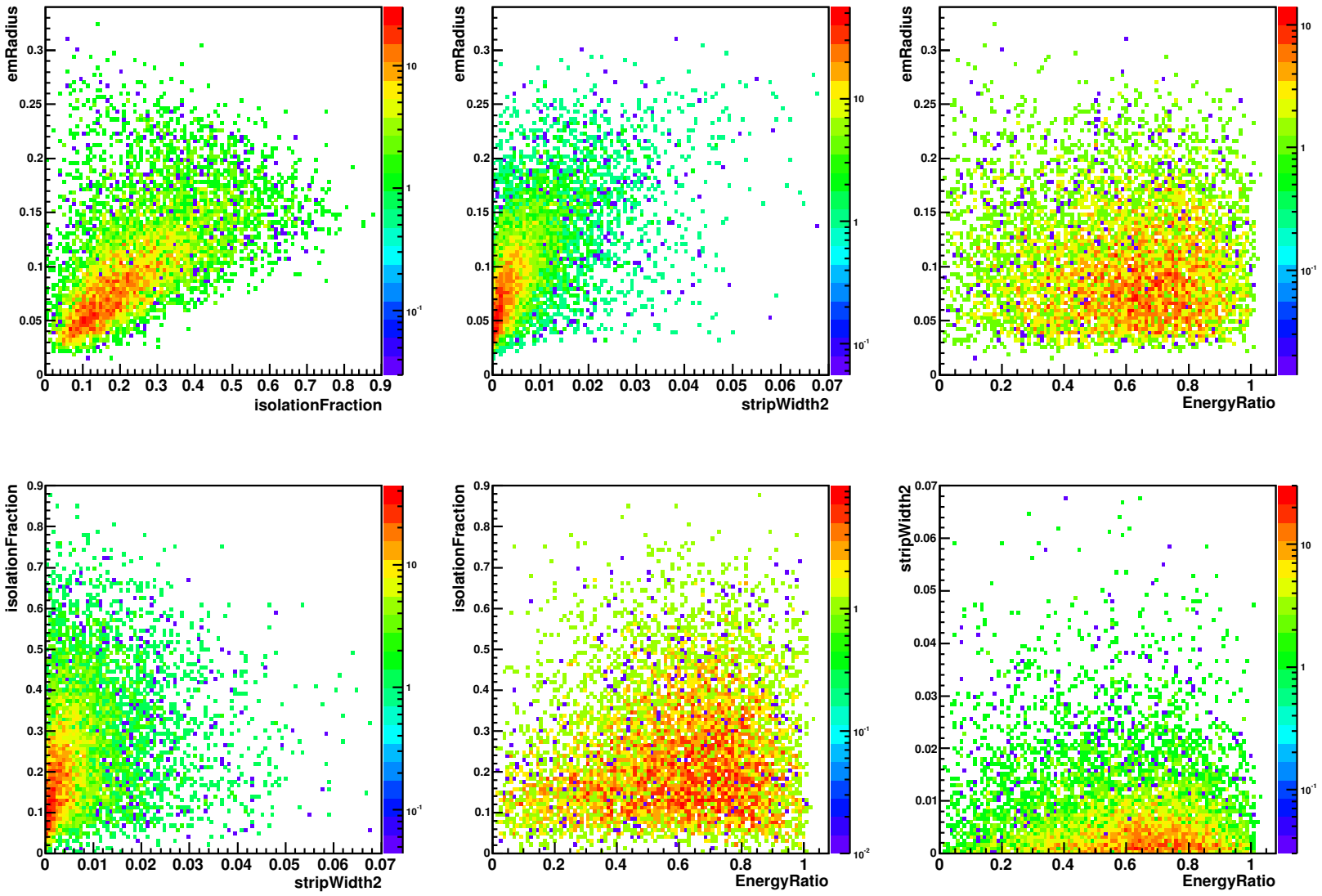

Figure 5.5: Correlations between the calorimeter only safe cut variables for reconstructed taus matched to 3-Prong hadronic MC taus (with $\triangle R < 0.2$) for the $t\bar{t}$ sample

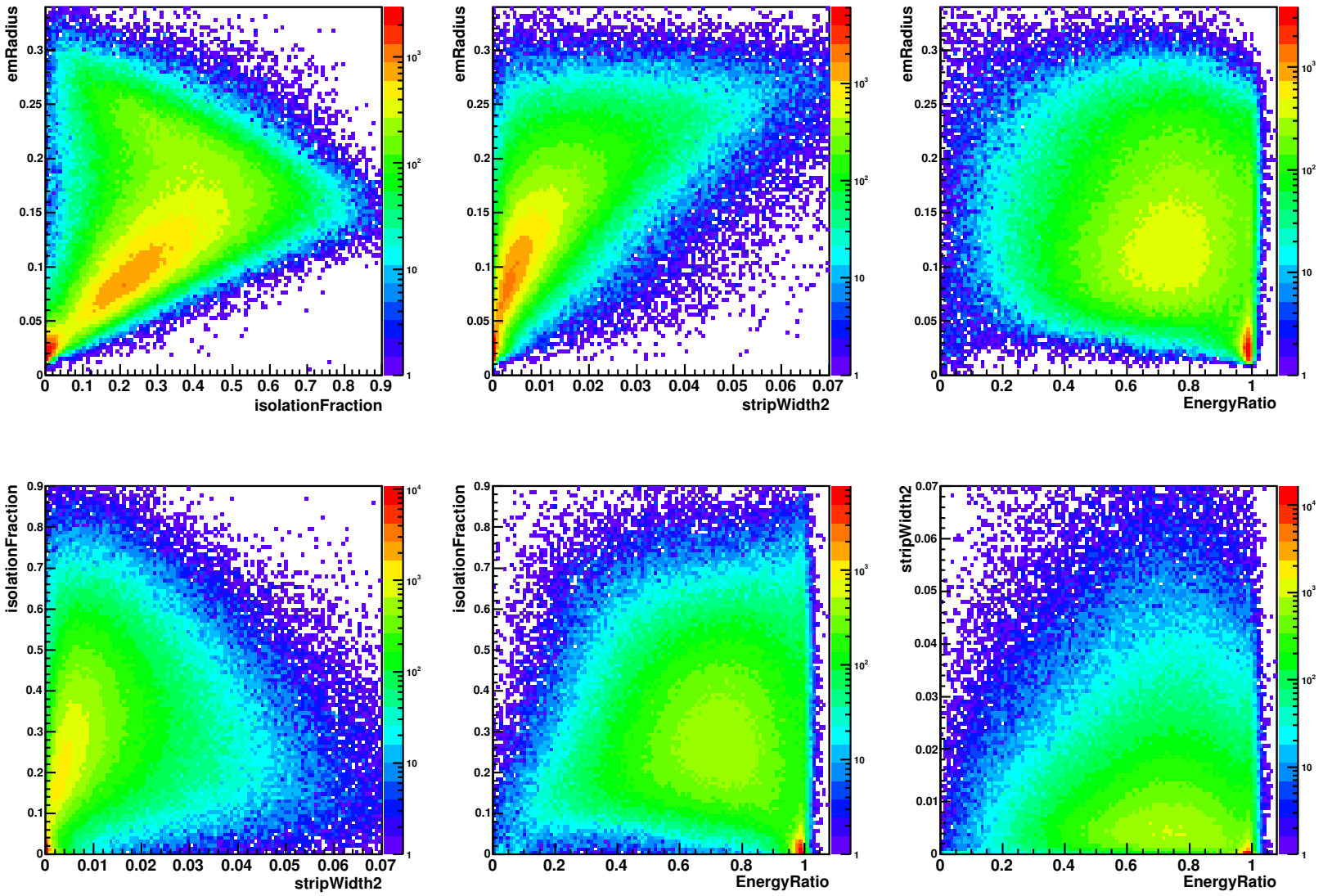

Figure 5.6: Correlations between the calorimeter only safe cut variables for reconstructed taus not matched to 1 or 3-Prong hadronic MC taus (with $\triangle R < 0.2$) for the $t\bar{t}$ sample. This therefore represents the correlations for the background fake taus within the sample

5.7 Performance Evaluation of a Single Cut Selection

5.7.1 Motivation

Having evaluated the performance of the calorimeter only safe cuts for $t\bar{t}$ events, and compared the safe cut performance for top events to cleaner environments, the study was extended by considering whether it would be possible to produce an equivalent simpler tau selection via the use of only one variable. As seen, the safe cuts use four variables, of which three are relatively well correlated as per section 5.6, which are combined in varying ways for the different p_{T} bins. For any given set of the safe cuts three of the variables are doing little with regards enhancing the fake tau discrimination.

It was hypothesized that one of these variables alone could be used to replace the safe cut combination. To test this, the study was evolved to look at how the safe cut performance compared to a cut on a single variable optimised for selection of 1-Prong or 3-Prong hadronic taus in the top sample. As per section 5.5.2, the fake taus produced by the extra jets within the top sample were used to provide the background fakes for both sets of cuts (i.e. allowing a direct comparison to be made between the safe cuts and the proposed single cut).

Two different single variable cuts were evaluated. The first used the variable IsolationFraction as the discriminant as it was considered to be the simplest of the four

variables, essentially being a variation on the isolation regions already used at the trigger level. Secondly, a single variable selection was produced based on EmRadius as this was considered to be the single variable that offered the best potential separation between the good and fake tau candidates.

5.7.2 Production of cut values

In order to produce the single cut values 1-Prong and 3-Prong hadronic taus were considered separately as for the safe cuts. For each variable two separate selections were produced, a first which was optimised in the same five p_{T} bins used by the safe cuts, and a second which had a single cut for the whole p_{T} range. Again the p_{T} region used was that of the reconstructed candidate. The selected variable was plotted in the required p_{T} region, with the distributions produced separately for those reconstructed taus matched (with $\triangle R < 0.2$) to Monte Carlo truth hadronic taus with the chosen prong (signal) and for those not matched to any Monte Carlo tau.

Starting at the plot origin, the cut location was moved across the distribution bin-by-bin from low to high values of the cut, with the signal selection efficiency and background rejection efficiency (and hence rejection factor) calculated for each bin. Selected taus were taken to be those with a value less than the cut value. The signal selection efficiency was defined as per equation 5.3 as previously. The rejection efficiency was defined as in equation 5.7, where the variables $N^{\mathrm{Total}}_{\mathrm{Unmatched}}$ and $N^{\mathrm{Pass}}_{\mathrm{Unmatched}}$ are as defined previously, with the rejection factor subsequently calculated as per

equation 5.8.

$$\epsilon^{\text{Rejection}}_{\text{Fake }\tau} = \frac{N^{\text{Total}}_{\text{Unmatched}} - N^{\text{Pass}}_{\text{Unmatched}}}{N^{\text{Total}}_{\text{Unmatched}}} \tag{5.7}$$

$$\text{RejectionFactor} = \frac{1}{\epsilon^{\text{n-prong}}_{\text{Fake }\tau}} = \frac{1}{1 - \epsilon^{\text{Rejection}}_{\text{Fake }\tau}} \tag{5.8}$$

As per the background rejection factors shown earlier in this chapter, only the inter-signal background was considered. For $t\bar{t}$ events this is effectively an n-jet background, comprising at least two b-jets for the dileptonic channel.

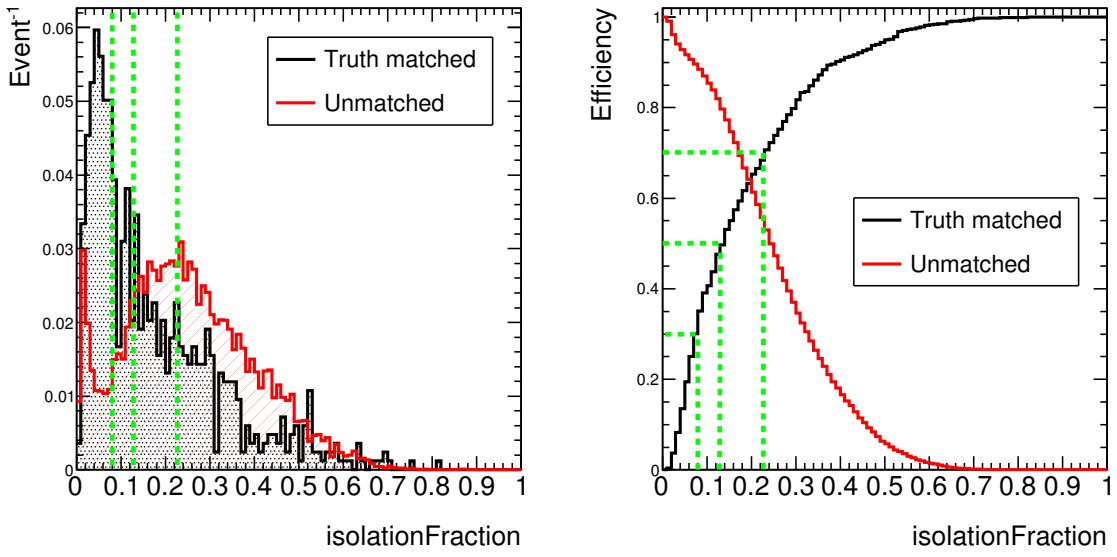

Figure 5.7: Illustration of setting the single variable cuts. Selection efficiencies are chosen and then background rejection factors calculated for the same bin. The right hand plot shows how the bin is selected based on given signal selection values while the left hand plot shows where the resulting cut appear on the signal and background distribtions

Efficiency definition

The three tau safe cut levels, loose medium and tight, had been chosen by their authors to give nominal selection efficiencies of 70%, 50% and 30% respectively, as stated in 5.4.4. These were defined relative to the Monte Carlo and not relative to the reconstruction (as was to be the case here), while the measured efficiencies were also seen to fluctuate slightly from the expected values for the $t\bar{t}$ sample. Therefore, to allow fair comparison between the safe cuts and a single cut selection, two different sets of cut values were produced.

Real cut values

Signal selection efficiencies of 70% (loose), 50% (medium) and 30% (tight) were chosen. The background rejection factors for the allocated bins were then calculated. Figure 5.7 shows an illustration of how this was carried out. The left hand plot shows the IsolationFraction distributions for the well matched (signal) and poorly matched (fake) tau candidates respectively. In the right hand plot can be seen the signal selection and background rejection efficiencies produced when the cut location is moved bin-by-bin from 0 to 1. Marked on the plots are the locations of cuts producing signal efficiencies of 70%, 50% and 30%. The background rejection is then calculated from the background efficiency seen in the same bin, which can simply be read off.

Equivalent cut values

To allow direct comparison to the safe cuts, the location of the loose, medium

and tight cuts was arranged so that the signal selection efficiency was matched to that seen for the equivalent safe cut with respect to the tau reconstruction. The background rejection efficiencies were then read off and converted into rejection factors which could be compared directly with those in section 5.5.2 for the safe cuts.

In the case of the 'real cuts', both p_{T} binned and global selections were produced for each of the two variables. In the case of the relative efficiencies only p_{T} binned values were produced.

5.7.3 Isolation Fraction Single Cut

The distributions used to produce the p_{T} binned single IsolationFraction cuts for 1-Prong and 3-Prong hadronic taus are shown in figures 5.8 and 5.9 respectively. The two figures are each divided into five sub-figures corresponding to the five p_{T} bins, with each sub-figure showing on the left the IsolationFraction distributions for matched and fake taus, and on the right the good tau selection and fake tau rejection efficiencies. The IsolationFraction distributions are normalised to unit area. For both hadronic tau prongs, it can be seen that as the p_{T} is increased (moving from (a) through to (e)) the discrimination between the good and fake taus is increased. This occurs by the signal distribution becoming narrower, with the upper edge moving towards smaller values of the IsolationFraction. The fake tau distribution shape remains approximately constant throughout. A potential negative effect of this is that the selection efficiency turn on curve becomes very

sharp at high p_{T}, and hence the efficiency values can become very bin dependent. As a consequence the value will become stongly sensitive to the modeling of both the detector and the tau itself.

Reading off the selection efficiencies and calculating the rejection factors as described previously produced the results shown in tables 5.6 to 5.9. The cut values themselves are shown in table 5.5. Tables 5.6 and 5.7 compare the IsolationFraction assigned efficiencies to the safe cut efficiencies for the 1-Prong and 3-Prong cases. What can be seen from the tables is that the IsolationFraction single cut only appears to perform better than the safe cuts, with respect to background rejection, when the safe cut selection efficiency is noteably looser than that of the single cut. When the selection efficiency of the two sets of cuts is approximately equal, as for the 1-Prong or 3-Prong loose cuts in the 45-70 GeV bin, the rejection for the safe cuts is seen to be slightly superior. This is backed up by the equivalent efficiency results for the two prongs shown in tables 5.8 and 5.9. Here it can be seen that the safe cuts perform better than the IsolationFraction almost exclusively for the same signal selection efficiency value, with the exception of the 70-100 GeV loose cuts. Furthermore, it can be seen that for the loose selections the background rejection of the single cut is approximately equivalent to that for the safe cuts. As the cut level is moved from loose to medium to tight the performance of the single cut degrades when compared to the safe cuts. In addition, the discrepancy between the two sets of rejection figures for the medium and tight cuts increases as the p_{T} of the bin increases.

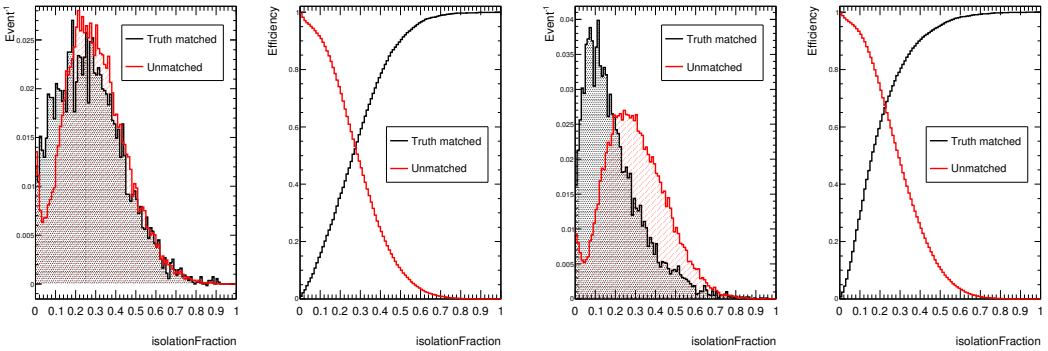

(a) 10-25 GeV

(b) 25-45 GeV

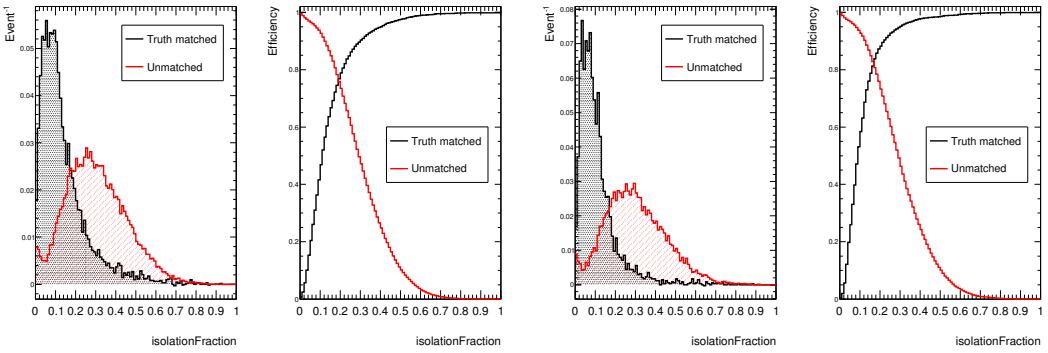

(c) 45-70 GeV

(d) 70-100 GeV

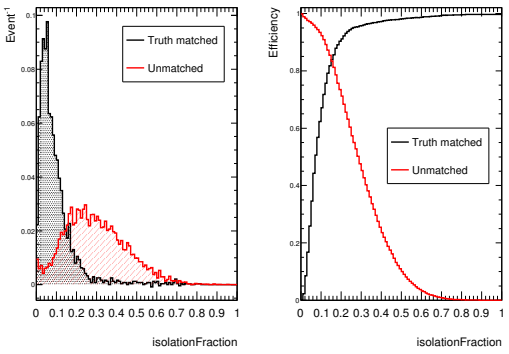

(e) >100 GeV

Figure 5.8: IsolationFraction : Signal and background (fake tau) distributions and efficiencies for 1-Prong taus in different p_{T} regions

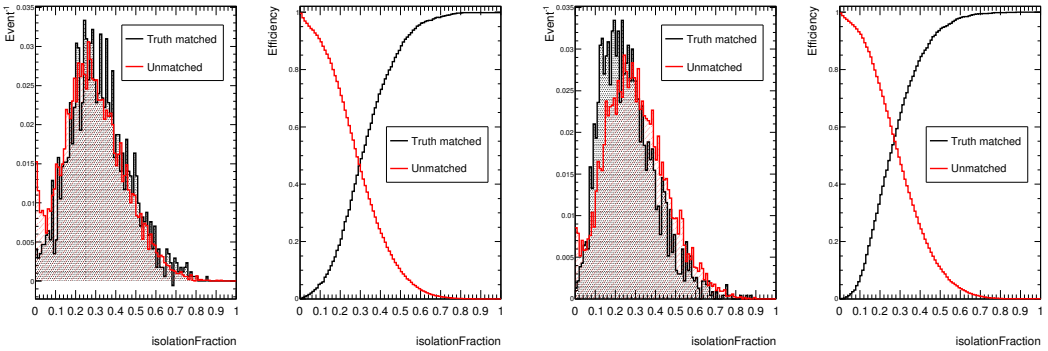

(a) 10-25 GeV *(b)* 25-45 GeV

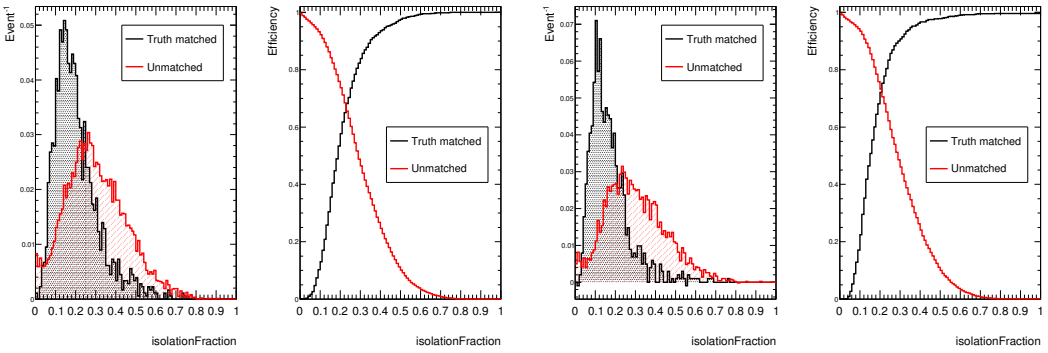

(c) 45-70 GeV *(d)* 70-100 GeV

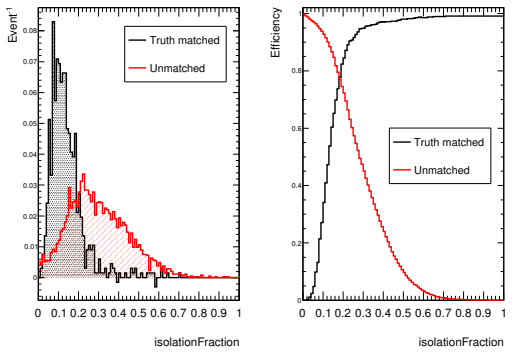

(e) >100 GeV

Figure 5.9: IsolationFraction : Signal and background (fake tau) distributions and efficiencies for 3-Prong taus in different p_{T} regions

p_T[GeV]	CutLevel	1-Prong		3-Prong	
		Real Cut Value	Equivalent Cut Value	Real Cut Value	Equivalent Cut Value
10-25	Loose	0.355	0.255	0.385	0.545
	Medium	0.255	0.115	0.305	0.365
	Tight	0.165	0.075	0.235	0.205
25-45	Loose	0.235	0.195	0.325	0.405
	Medium	0.155	0.105	0.255	0.205
	Tight	0.095	0.065	0.185	0.145
45-70	Loose	0.165	0.175	0.245	0.255
	Medium	0.105	0.095	0.185	0.165
	Tight	0.065	0.055	0.145	0.115
70-100	Loose	0.125	0.305	0.195	0.405
	Medium	0.085	0.075	0.155	0.135
	Tight	0.055	0.055	0.115	0.105
>100	Loose	0.105	0.495	0.165	0.175
	Medium	0.065	0.055	0.125	0.145
	Tight	0.045	0.035	0.095	0.075

Table 5.5: IsolationFraction p_T binned cut values used to select 1-Prong and 3-Prong hadronic taus in $t\bar{t}$ events. Real cuts give pre-set signal selection efficiencies, equivalent cut values match the signal selection efficiency to that for the calorimeter only safe cuts

p_T[GeV]	CutLevel	Efficiency (Safe cuts)	Efficiency (IsolFrac cut)	Rejection	
		TauRec Before/After	TauRec Before/After	Safe Cuts	IsolFrac Cut
10-25	Loose	0.48	0.70	2.86	1.46
	Medium	0.19	0.48	7.92	2.26
	Tight	0.10	0.28	14.57	4.67
25-45	Loose	0.60	0.69	5.21	2.66
	Medium	0.30	0.48	15.88	5.60
	Tight	0.16	0.28	26.41	12.98
45-70	Loose	0.73	0.69	6.68	5.18
	Medium	0.39	0.47	24.27	11.56
	Tight	0.18	0.26	42.01	21.57
70-100	Loose	0.95	0.69	1.68	8.73
	Medium	0.43	0.47	32.90	15.97
	Tight	0.24	0.26	44.68	25.39
>100	Loose	0.98	0.67	1.11	10.98
	Medium	0.36	0.44	51.48	20.52
	Tight	0.16	0.26	77.55	29.12

Table 5.6: Hadronic 1-Prong tau selection efficiency and rejection factors with respect to reconstructed taus. Values are shown for a single cut on IsolationFraction and for the tau calorimeter only safe cuts for $t\bar{t}$ events. Real IsolationFraction cuts are shown intended to give selection efficiencies of 70%, 50% and 30%

p_T[GeV]	CutLevel	Efficiency (Safe cuts)	Efficiency (IsolFrac cut)	Rejection	
		TauRec Before/After	TauRec Before/After	Safe Cuts	IsolFrac Cut
10-25	Loose	0.92	0.69	1.15	1.36
	Medium	0.64	0.49	1.64	1.80
	Tight	0.20	0.29	3.77	2.72
25-45	Loose	0.84	0.70	1.65	1.72
	Medium	0.37	0.51	4.97	2.51
	Tight	0.17	0.30	9.69	4.45
45-70	Loose	0.72	0.70	2.78	2.71
	Medium	0.39	0.49	9.82	4.60
	Tight	0.16	0.30	21.05	7.29
70-100	Loose	0.97	0.68	1.23	4.14
	Medium	0.42	0.51	14.56	6.91
	Tight	0.22	0.30	26.16	12.97
>100	Loose	0.75	0.70	8.76	5.48
	Medium	0.61	0.47	13.74	10.05
	Tight	0.14	0.27	62.08	16.27

Table 5.7: Hadronic 3-Prong tau selection efficiency and rejection factors with respect to reconstructed taus. Values are shown for a single cut on IsolationFraction and for the tau calorimeter only safe cuts for $t\bar{t}$ events. Real IsolationFraction cuts are shown intended to give selection efficiencies of 70%, 50% and 30%

p_T[GeV]	CutLevel	Efficiency (Safe cuts)	Efficiency (IsolFrac cut)	Rejection	
		TauRec Before/After	TauRec Before/After	Safe Cuts	IsolFrac Cut
10-25	Loose	0.48	0.48	2.86	2.26
	Medium	0.19	0.18	7.92	8.39
	Tight	0.10	0.11	14.57	13.74
25-45	Loose	0.60	0.59	5.21	3.67
	Medium	0.30	0.31	15.88	11.09
	Tight	0.16	0.17	26.41	20.32
45-70	Loose	0.73	0.72	6.68	4.60
	Medium	0.39	0.42	24.27	13.60
	Tight	0.18	0.20	42.01	25.21
70-100	Loose	0.95	0.95	1.68	1.77
	Medium	0.43	0.40	32.90	18.82
	Tight	0.24	0.26	44.68	25.39
>100	Loose	0.98	0.98	1.11	1.11
	Medium	0.36	0.35	51.48	24.49
	Tight	0.16	0.17	77.55	35.37

Table 5.8: Hadronic 1-Prong tau selection efficiency and rejection factors with respect to reconstructed taus. Values are shown for a single cut on IsolationFraction and for the tau calorimeter only safe cuts for $t\bar{t}$ events with the IsolationFraction selection efficiencies matched to those of the equivalent safe cuts

p_T[GeV]	CutLevel	Efficiency (Safe cuts)	Efficiency (IsolFrac cut)	Rejection	
		TauRec Before/After	TauRec Before/After	Safe Cuts	IsolFrac Cut
10-25	Loose	0.92	0.92	1.15	1.07
	Medium	0.64	0.64	1.64	1.44
	Tight	0.20	0.21	3.77	3.44
25-45	Loose	0.84	0.85	1.65	1.32
	Medium	0.37	0.36	4.97	3.68
	Tight	0.17	0.19	9.69	7.28
45-70	Loose	0.72	0.74	2.78	2.51
	Medium	0.39	0.40	9.82	5.67
	Tight	0.16	0.17	21.05	11.01
70-100	Loose	0.97	0.97	1.23	1.26
	Medium	0.42	0.42	14.56	9.32
	Tight	0.22	0.22	26.16	15.15
>100	Loose	0.75	0.74	8.76	4.88
	Medium	0.61	0.60	13.74	7.50
	Tight	0.14	0.13	62.08	22.80

Table 5.9: Hadronic 3-Prong tau selection efficiency and rejection factors with respect to reconstructed taus. Values are shown for a single cut on IsolationFraction and for the tau calorimeter only safe cuts for $t\bar{t}$ events with the IsolationFraction selection efficiencies matched to those of the equivalent safe cuts

Global Pt Cut

Having noted that the performance of a p_{T} binned single cut is in general worse, and at best equivalent to, the safe cuts, the global 1-Prong and 3-Prong IsolationFraction cuts were also produced. The advantage of producing a global cut of this nature is that the performance of the cut will vary more smoothly with p_{T} than will be the case for a discretely binned set of cuts. Figure 5.10 shows the IsolationFraction and corresponding efficiency distributions for the 1-Prong (a) and 3-Prong (b) hadronic taus. The resulting assigned signal selection efficiencies and background rejection factors are shown in table 5.10 for both 1-Prong and 3-Prong taus. Looking at table 5.6 for the 1-Prong case binned cut values and at table 5.7 for the 3-Prong case it can be seen that the global p_{T} cut is seen to offer a rejection value on a par with the binned cut for the 25-45 GeV region. At higher p_{T}, the global p_{T} cut is looser than the binned cuts, and so as a consequence the rejection is less powerful for the global cut (although the efficiency would also be expecter to be higher).

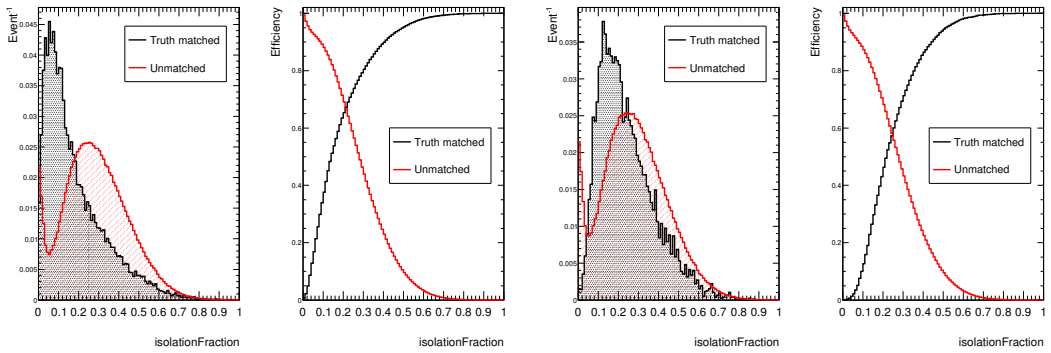

(a) 1-Prong *(b)* 3-Prong

Figure 5.10: IsolationFraction : Signal and background (fake tau) distributions and efficiencies for hadronic taus over the entire p_{T} range

Decay type	Cut Level	Cut Value	Efficiency (IsolFrac) TauRec Before/After	IsolFrac Rejection
1-Prong	Loose	0.235	0.71	2.44
	Medium	0.145	0.51	5.06
	Tight	0.085	0.30	9.29
3-Prong	Loose	0.295	0.69	1.84
	Medium	0.215	0.49	2.92
	Tight	0.155	0.29	4.82

Table 5.10: Hadronic tau selection efficiency and rejection factors with respect to reconstructed taus. Values are shown for a single cut on IsolationFraction for $t\bar{t}$ events. Single cuts are produced for one bin covering the whole tau p_{T} range

5.7.4 IsolationFraction Summary

It has been seen that for a single cut on the IsolationFraction of the tau, the discrimination power for distinguishing good taus from fakes increases as p_{T} increases. Although it is difficult to make an exact comparison between the p_{T} binned IsolationFraction cut and the calorimeter only safe cuts due to the variation in the selection efficiencies of the latter, it has been seen that the safe cuts generally give better rejection for equivalent efficiency values. The IsolationFraction single cut was seen to perform better only when the safe cut efficiency is excessively large (relative to the target efficiency). An IsolationFraction p_{T} a global p_{T} cut (in general) was seen to give a performance akin to that for the binned single variable cut in the 25-45 GeV p_{T} region.

5.7.5 EmRadius Single Cut

It was seen in 5.7.3 that in general a single cut, either p_{T} dependent or for global p_{T}, on the IsolationFraction does not give better hadronic tau identification than the four variable calorimeter only safe cuts. However, although IsolationFraction can be considered the simplest of the four safe cut variables, EmRadius is potentially the better discriminant. Therefore the process followed in 5.7.3 was repeated to examine a single cut on the EmRadius. The p_{T} binned EmRadius good and fake tau distributions for $t\bar{t}$ events, together with their equivalent signal selection and background rejection efficiencies, are shown by figures 5.11 and 5.12 for the 1-Prong and 3-Prong hadronic taus respectively. As for IsolationFraction, the figures show

that the distinction between the taus well matched to the Monte Carlo truth and the fakes improves with increasing p_{T}. Likewise, as for IsolationFraction the signal selection efficiency turn-on curve becomes steep at high p_{T}. This is again the case for both prongs. As before, the background rejection factors were calculated for assigned signal selection efficiencies, with respect to reconstructed taus, of 70%, 50% and 30%. These are compared to the safe cuts in tables 5.12 and 5.13 with the cut values shown in table 5.11. It is difficult to make a direct comparison with the safe cuts for the EmRadius assigned efficiencies due to variance of the safe cut signal efficiencies, but where they are similar in the 3-Prong 45-70 GeV loose case, the EmRadius cut performs better than the safe cuts. However, the EmRadius assigned efficiencies can be compared directly to the IsolationFraction assigned efficiencies in tables 5.6 and 5.7. Making this direct comparison of the two single variable p_{T} binned cuts, it can be seen that the EmRadius cut performs better in almost every case except the tight 1-Prong 10-25 GeV cut, where the rejection for the two variables is almost identical. The advantage of using the EmRadius cut over the IsolationFraction cut also becomes more beneficial with increasing p_{T}. This conclusively supported the hypothesis that EmRadius is a better good tau distinguishing variable for $t\bar{t}$ events. Furthermore, it suggested that EmRadius would perform better in an equivalent efficiency comparison with the safe cuts.

To allow better examination of the performance, equivalent EmRadius efficiencies were again produced and are shown in tables 5.14 and 5.15. The cuts themselves are again shown in table 5.11. From examining these, it can be seen that for all cut levels, in all p_{T} bins, and for both prongs the EmRadius single cuts perform as well

or better than the safe cuts with regards to background rejection for an equivalent good tau selection efficiency. Consequently, it is possible to conclude that it is possible to produce a hadronic tau selection that for $t\bar{t}$ events performs as well as the calorimeter only safe cuts, using only the variable EmRadius for calorimeter seeded tau candidates.

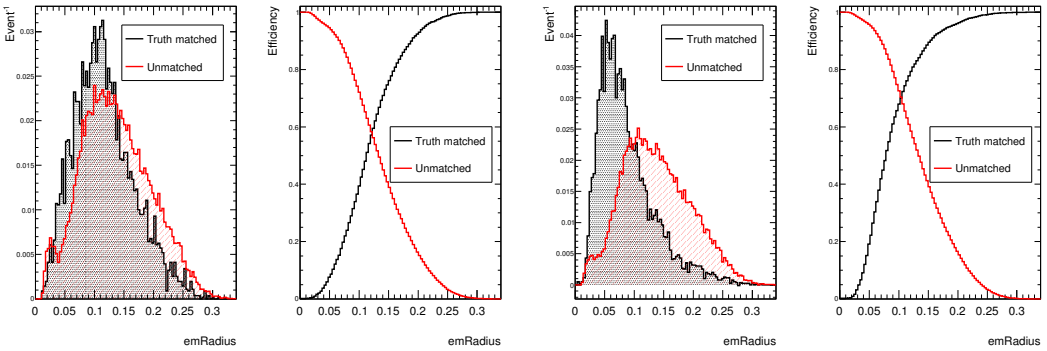

(a) 10-25 GeV

(b) 25-45 GeV

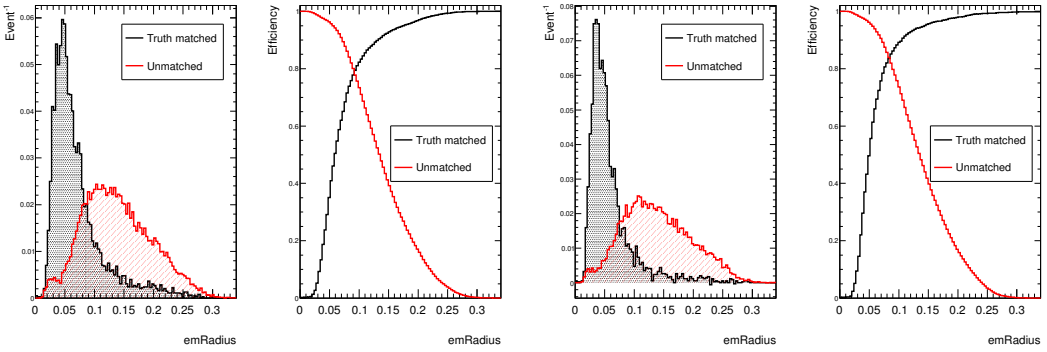

(c) 45-70 GeV

(d) 70-100 GeV

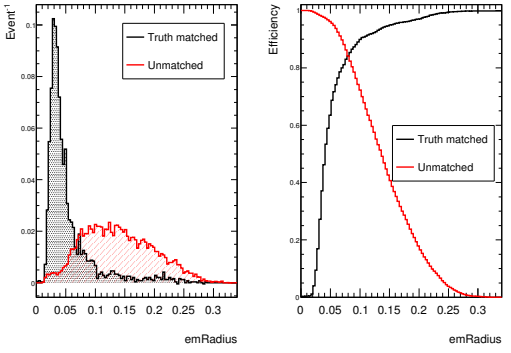

(e) >100 GeV

Figure 5.11: EmRadius : Signal and background (fake tau) distributions and efficiencies for 1-Prong taus in different p_{T} regions

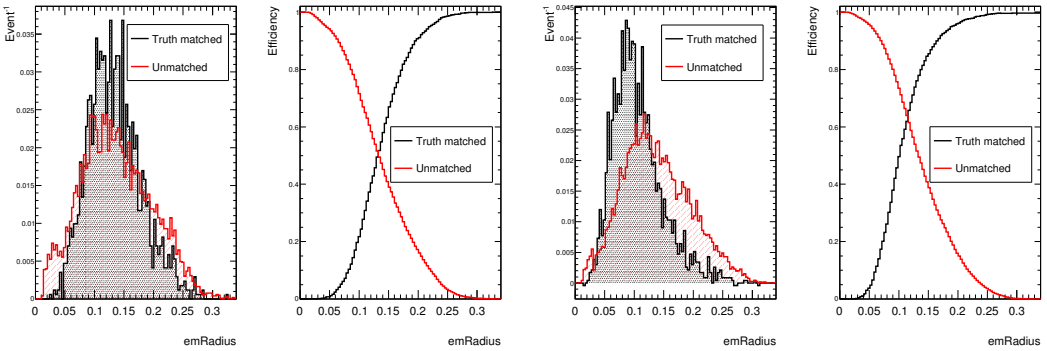

(a) 10-25 GeV

(b) 25-45 GeV

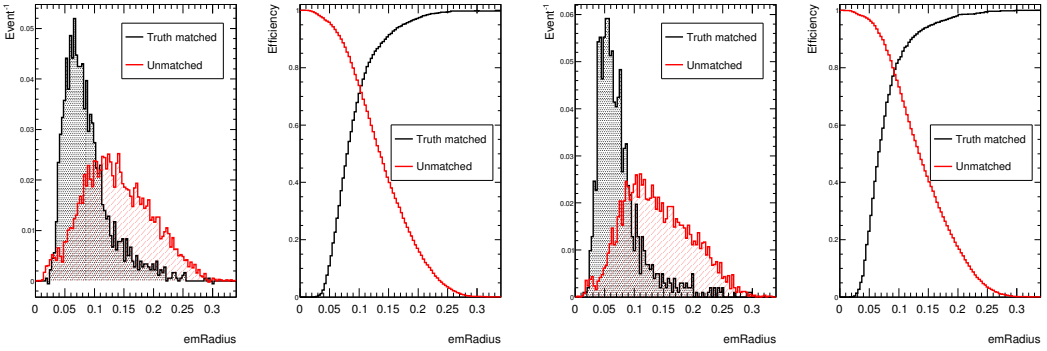

(c) 45-70 GeV

(d) 70-100 GeV

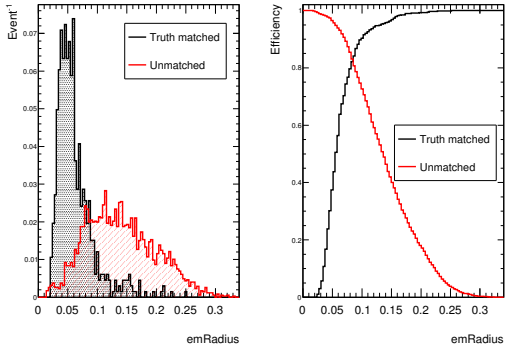

(e) >100 GeV

Figure 5.12: EmRadius : Signal and background (fake tau) distributions and efficiencies for 3-Prong taus in different p_{T} regions

p_T[GeV]	CutLevel	1-Prong		3-Prong	
		Real Cut Value	Equivalent Cut Value	Real Cut Value	Equivalent Cut Value
10-25	Loose	0.1377	0.1105	0.1547	0.2057
	Medium	0.1139	0.0731	0.1309	0.1479
	Tight	0.0901	0.0561	0.1105	0.0969
25-45	Loose	0.1037	0.0901	0.1207	0.1479
	Medium	0.0799	0.0595	0.1003	0.0901
	Tight	0.0595	0.0459	0.0833	0.0697
45-70	Loose	0.0765	0.0833	0.1003	0.1003
	Medium	0.0595	0.0527	0.0799	0.0697
	Tight	0.0459	0.0391	0.0663	0.0527
70-100	Loose	0.0629	0.1445	0.0833	0.1853
	Medium	0.0493	0.0459	0.0663	0.0595
	Tight	0.0391	0.0357	0.0527	0.0493
>100	Loose	0.05270	0.2159	0.0697	0.0731
	Medium	0.0391	0.0357	0.0561	0.0629
	Tight	0.0323	0.0289	0.0459	0.0391

Table 5.11: EmRadius p_T binned cut values used to select 1-Prong and 3-Prong hadronic taus in $t\bar{t}$ events. Real cuts give pre-set signal selection efficiencies, equivalent cut values match the signal selection efficiency to that for the calorimeter only safe cuts

p_T[GeV]	CutLevel	Efficiency (Safe cuts)	Efficiency (EmRadius cut)	Rejection	
		TauRec Before/After	TauRec Before/After	Safe Cuts	EmRadius Cut
10-25	Loose	0.48	0.69	2.86	1.89
	Medium	0.19	0.51	7.92	2.7
	Tight	0.10	0.32	14.57	4.63
25-45	Loose	0.60	0.70	5.21	3.37
	Medium	0.3	0.52	15.88	6.84
	Tight	0.16	0.30	26.41	15.62
45-70	Loose	0.73	0.68	6.68	8.22
	Medium	0.39	0.50	24.27	17.23
	Tight	0.18	0.29	42.01	31.81
70-100	Loose	0.95	0.69	1.68	13.95
	Medium	0.43	0.50	32.90	26.15
	Tight	0.24	0.30	44.68	42.80
>100	Loose	0.98	0.69	1.11	22.35
	Medium	0.36	0.46	51.48	42.20
	Tight	0.16	0.27	77.55	59.84

Table 5.12: Hadronic 1-Prong tau selection efficiency and rejection factors with respect to reconstructed taus. Values are shown for a single cut on EmRadius and for the tau calorimeter only safe cuts for $t\bar{t}$ events. Real EmRadius cuts are shown intended to give selection efficiencies of 70%, 50% and 30%

p_T[GeV]	CutLevel	Efficiency (Safe cuts)	Efficiency (EmRadius cut)	Rejection	
		TauRec Before/After	TauRec Before/After	Safe Cuts	EmRadius Cut
10-25	Loose	0.92	0.69	1.15	1.60
	Medium	0.64	0.49	1.64	2.07
	Tight	0.20	0.31	3.77	2.86
25-45	Loose	0.84	0.69	1.65	2.43
	Medium	0.37	0.50	4.97	3.77
	Tight	0.17	0.30	9.69	6.12
45-70	Loose	0.72	0.71	2.78	3.81
	Medium	0.39	0.50	9.82	6.87
	Tight	0.16	0.32	21.05	11.36
70-100	Loose	0.97	0.71	1.23	6.43
	Medium	0.42	0.51	14.56	12.52
	Tight	0.22	0.29	26.16	26.41
>100	Loose	0.75	0.70	8.76	10.72
	Medium	0.61	0.51	13.74	19.35
	Tight	0.14	0.30	62.08	38.92

Table 5.13: Hadronic 3-Prong tau selection efficiency and rejection factors with respect to reconstructed taus. Values are shown for a single cut on EmRadius and for the tau calorimeter only safe cuts for $t\bar{t}$ events. Real EmRadius cuts are shown intended to give selection efficiencies of 70%, 50% and 30%

p_T[GeV]	CutLevel	Efficiency (Safe cuts)	Efficiency (EmRadius cut)	Rejection	
		TauRec Before/After	TauRec Before/After	Safe Cuts	EmRadius Cut
10-25	Loose	0.48	0.48	2.86	2.88
	Medium	0.19	0.20	7.92	8.01
	Tight	0.10	0.10	14.57	14.49
25-45	Loose	0.60	0.61	5.21	4.85
	Medium	0.30	0.30	15.88	15.62
	Tight	0.16	0.15	26.41	27.08
45-70	Loose	0.73	0.74	6.68	6.28
	Medium	0.39	0.41	24.27	23.37
	Tight	0.18	0.19	42.01	40.98
70-100	Loose	0.95	0.95	1.68	1.79
	Medium	0.43	0.43	32.90	31.40
	Tight	0.24	0.22	44.68	50.26
>100	Loose	0.98	0.98	1.11	1.14
	Medium	0.36	0.37	51.48	48.69
	Tight	0.16	0.17	77.55	78.09

Table 5.14: Hadronic 1-Prong tau selection efficiency and rejection factors with respect to reconstructed taus. Values are shown for a single cut on EmRadius and for the tau calorimeter only safe cuts for $t\bar{t}$ events with the EmRadius selection efficiencies matched to those of the equivalent safe cut

p_T[GeV]	CutLevel	Efficiency (Safe cuts)	Efficiency (EmRadius cut)	Rejection	
		TauRec Before/After	TauRec Before/After	Safe Cuts	EmRadius Cut
10-25	Loose	0.92	0.92	1.15	1.18
	Medium	0.64	0.63	1.64	1.69
	Tight	0.20	0.20	3.77	3.85
25-45	Loose	0.84	0.85	1.65	1.69
	Medium	0.37	0.38	4.97	5.01
	Tight	0.17	0.17	9.69	10.09
45-70	Loose	0.72	0.71	2.78	3.81
	Medium	0.39	0.37	9.82	9.97
	Tight	0.16	0.14	21.05	20.32
70-100	Loose	0.97	0.97	1.23	1.3
	Medium	0.42	0.40	14.56	18.54
	Tight	0.22	0.23	26.16	31.52
>100	Loose	0.75	0.74	8.76	9.29
	Medium	0.61	0.64	13.74	14.49
	Tight	0.14	0.17	62.08	53.29

Table 5.15: Hadronic 3-Prong tau selection efficiency and rejection factors with respect to reconstructed taus. Values are shown for a single cut on EmRadius and for the tau calorimeter only safe cuts for $t\bar{t}$ events with the EmRadius selection efficiencies matched to those of the equivalent safe cut

Global Pt Cut

Following the same procedure as for IsolationFraction, a global p_{T} EmRadius single variable selection was evaluated. Fig. 5.13 shows the EmRadius distributions and efficiency curves for the 1-Prong (a) and 3-Prong (b) taus, while the background rejection factors for the assigned signal selection efficiencies are given in table 5.16. These can then be compared back to the p_{T} binned EmRadius rejection factors in tables 5.12 and 5.13. As for IsolationFraction, the global p_{T} cut provides a rejection akin to that of the p_{T} binned cut for the 25-45 GeV region, with the global cut being looser at larger p_{T}. Noting that the shape of the background distribution is similar for each of the p_{T} bins but that the signal shape changes, it is possible to see how tightening the cut via the use of a p_{T} binned selection can provide a better rejection at higher p_{T}. This applies for both hadronic tau prongs. Comparing back to the IsolationFraction global cut in table 5.10 the global EmRadius cut is seen to perform significantly better.

5.8 Overall Conclusions

Within this chapter a general introduction was given on tau identification with the ATLAS detector. The calorimeter only tau safe cuts were introduced and an investigation was carried out to compare their performance for $t\bar{t}$ events to that for a combined sample of $Z \rightarrow \tau\tau$ and $bbA \rightarrow bb\tau\tau$ events. It was concluded that with regards to good tau selection efficiencies the safe cut performance compared well

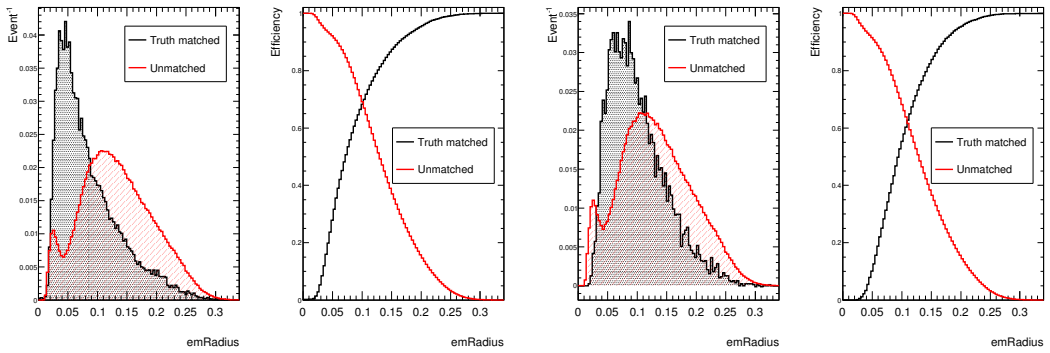

(a) 1-Prong *(b)* 3-Prong

Figure 5.13: EmRadius : Signal and background (fake tau) distributions and efficiencies for hadronic taus over the entire p_{T} range

Decay type	Cut Level	Cut Value	Efficiency (EmRadius) TauRec Before/After	EmRadius Rejection
1-Prong	Loose	0.1037	0.70	3.03
	Medium	0.0731	0.51	6.49
	Tight	0.0527	0.32	11.63
3-Prong	Loose	0.1207	0.69	2.22
	Medium	0.0935	0.50	3.63
	Tight	0.0731	0.31	6.11

Table 5.16: Hadronic tau selection efficiency and rejection factors with respect to reconstructed taus. Values are shown for a single cut on EmRadius for $t\bar{t}$ events. Single cuts are produced in one bin for the whole tau p_{T} range

in top events relative to the cleaner sample, behaving in the same way but with a slightly lower efficiency. Two alternative selections were proposed based on a single variable only, and it was concluded that for the same p_{T} binning as the safe cuts, an equivalent performance could be obtained using a single cut on the EmRadius. A global p_{T} selection was also studied and seen to perform in a similar way to a p_{T} binned selection in the p_{T} range of 25-45 GeV. [4]

[4]Since this study was completed, a new safe tau selection has been produced by the ATLAS tau working group [55]. The new selection uses only 3 variables (of which EmRadius is the main discriminant) and two p_{T} bins covering 0-100 GeV and >100 GeV respectively.

Chapter 6

Measurement of the $t\bar{t}$ Cross Section

6.1 Introduction

Described in this chapter is a proposed method for measuring the $t\bar{t}$ production cross section at the LHC, via the tau+jets channel with the ATLAS detector. Intended for use with early LHC data, the analysis is based on a series of simple cuts. These were designed to suppress the various standard model backgrounds whilst simultaneously increasing the purity of the desired section of the $t\bar{t}$ signal. The analysis has been largely developed with Monte Carlo simulated events, with a first look being made at the 2010 ATLAS data.

6.2 Signal

At the LHC $t\bar{t}$ pairs are produced readily. The events are classified by the top decay products as described in 1.5. Excluding the fully hadronic $t\bar{t}$ events, these were simulated for a centre-of-mass energy of 7 TeV, at next to leading order (NLO), using the MC@NLO v3.41 event generator [56] coupled to Herwig/Jimmy to provide the parton shower modelling [56]. A top mass of 172.5 GeV was assumed and the CTEQ66 NLO pdf set used [56]. The sample was simulated with a cross-section of 80.201 pb for the non-hadronic $t\bar{t}$ and then scaled to a more recent theoretical prediction by Ulrich Husemann (Moch and Uwer) [57] by use of a 'K-factor'of 1.11 [58].

6.3 Backgrounds

For the purposes of the analysis described, the fully hadronic $t\bar{t}$ decay (not including taus) is considered as part of the background. This was also simulated using Mc@NLO and Herwig/Jimmy with a cross-section of 64.064 pb corrected by a K factor of 1.17 [58]. The same pdf set was also used as for the signal sample. Single top samples contribute a small background and were generated with Mc@NLO coupled to Herwig to provide the parton showering [58]. Cross-sections for the single top samples were taken directly from the generator at NLO [58].

The primary backgrounds for top studies are provided by W/Z + jets (both light quark and heavy flavour) and QCD events. The primary background varies depending on the particular top decay being studied. For tau+lepton events, the

W/Z+jets are more significant, whereas controlling the QCD background is the key factor for studies in the tau+jets scenario. For W/Z+jets a series of different Monte Carlo samples was generated with Alpgen [58] with the parton shower modeled by Herwig/Jimmy [58]. A pdf set based on CTEQ6L1 was used. The samples were generated in the form W+Np(i) and Z+Np(i) where i corresponds to the number of additional partons produced in association to the W boson. Samples were separately produced for the W or Z decaying to each of the lepton flavours. Likewise, similar samples were produced of the form $W/Z+\bar{b}$+Np(i) which have a smaller cross-section but final state closer to the $t\bar{t}$ signal. As for the different top samples K factors were used to rescale the cross sections.

QCD multijet samples were generated with Alpgen, again using Herwig/Jimmy to provide the parton shower modelling [58]. Samples were split up into a series of p_{T} slices and based on the number of additional initial partons in the scatter. A separate set of samples of the same type were produced in the same way with the addition of a $\bar{b}$ pair. K factors were not used for the QCD samples. In addition, the very large cross sections present for the low p_{T} and low parton cases meant that it was not possible to simulate a number of events of similar magnitude to that expected in the data. Whilst scale factors were used to get an idea of the QCD contribution, ideally the QCD background should be evaluated by data driven techniques. From the Monte Carlo, a second estimate of the QCD contribution was obtained by examining an inclusive dijet sample generated by and with the parton shower provided by Pythia [40]. This was divided into nine p_{T} slices labeled J0 to J9, with large scale factors again required for the lowest. The sample binning

was classified acording to the p_{T} of the hard scatter, with the ranges defined; J0 = 10-17 GeV, J1 = 17-35 GeV, J2 = 35-70 GeV, J3 = 70-140 GeV, J4 = 140-280 GeV, J5 = 280-560 GeV, J6 = 560-1120 GeV, J7 = 1120-2280 GeVand J8 = 2280 GeVand above [59]. As better statistics were available for the Pythia samples, these were used in preference to the Alpgen samples to estimate the regions of phase space expected to be occupied by QCD events after a given selection was applied. However, due to both statistics and uncertainties in the cross-sections [58], it was necessary to estimate the true shape and normalisation of the QCD events from data.

6.4 LHC Data Periods

During 2010 the ATLAS detector collected a nominal 45.0 pb^{-1} of proton-proton physics data [21]. These data were divided into nine main luminosity periods labeled A-I [60]. The bulk of the data were collected in the last two of these periods, with periods H and I together comprising a nominal 32.3 pb^{-1} [60]. It is this sample that was examined by the analysis described in this chapter. Data during these two periods were output into four inclusive data streams; egamma, jetTauEtMiss, muon and minBias [61]. For the purpose of this analysis the jetTauEtMiss stream was used, with checks for good data applied via the appropriate 'good run lists' (GRL) for periods H [1] and I [2] respectively [62]. After application of the GRL the total

[1] data10_7TeV.periodH.166466-166964_LBSUMM_DetStatus-v03-pass1-analysis-2010H_top_allchannels_7TeV.xml

[2] data10_7TeV.periodI.167575-167844_LBSUMM_DetStatus-v03-pass1-analysis-2010I_top_allchannels_7TeV.xml

luminosity processed by the analysis was 26.4 pb^{-1} [63].

6.5 Object Pre - Selections

6.5.1 Tau

The good tau selection used was based on the EmRadius single variable, global p_{T}, cut described in 5.7.5. Tau candidates were however required to be both calorimeter and track seeded. This was then developed in a way consistent with the electron and muon selections used by the ATLAS top physics group. As such, selected tau candidates were required to pass the tight cut level (by possessing an EmRadius < 0.05 for the 1-Prong case and < 0.07 in the three prong case, where the prong was defined in terms of the number of reconstructed tracks. 1-Prong candidates were required to have exactly one track and 3-Prong greater than or equal to two tracks), have offline $p_T > 20$ GeV and satisfy $|\eta| < 2.5$ (so as to lie within the real calorimeter coverage). To improve the discrimination between genuine taus and fakes with a narrow jet topography, candidates were required to have exactly one or three reconstructed tracks. Fig 6.1 shows the number of tracks for candidates which are matched to 1-Prong and 3-Prong hadronic taus in the signal sample, compared to the non-matched candidates. Similarly, it was required that the charge of the selected candidates be ± 1, with Fig. 6.2 showing the charge of truth matched and non truth matched candidates in the Monte Carlo signal sample. Finally, the calorimeter crack region that was excluded from the selected electrons was also excluded from the tau

selection (see section 6.5.6). Any tau candidate found within $1.37 < |\eta| < 1.52$ was therefore discarded. This was to prevent any electrons produced in an event but going into the crack region from being incorrectly reconstructed as tau candidates and not removed by overlap removal. As discussed previously 5.2, the good tau selection was only intended to identify hadronic decaying taus. Any taus which decayed directly to either electrons or muons were considered as such.

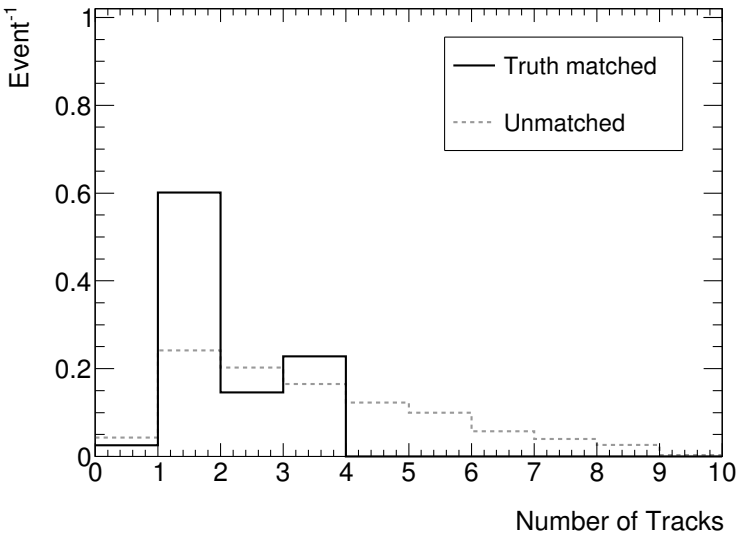

Figure 6.1: Number of tracks associated with reconstructed tau candidates when either matched to a Monte Carlo truth hadronic tau or not. Plots are normalised to unit area

6.5.2 Jet

Jets were reconstructed via the Anti-$k_\perp$ algorithm for a D size parameter of 0.4 [64] and calibrated in accordance with the H1 calibration at the hadronic scale [56]. These were built from uncalibrated calorimeter topological clusters at the EM scale [56]. Topological clustering is the current ATLAS default strategy which sums neighbour-

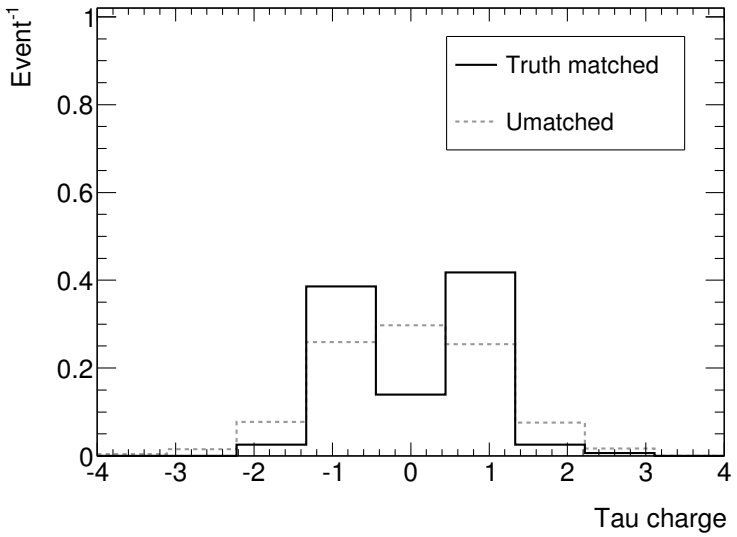

Figure 6.2: Charge of reconstructed tau candidates when either matched to a Monte Carlo truth hadronic tau or not. Plots are normalised to unit area

ing calorimeter cells based on their energy significance to build up the cluster, which can be of varying size [65]. This contrasts to the alternative algorithm (formerly the ATLAS default when used with calorimeter towers as an input) which used a fixed size cone in $\eta \times \phi$. Jets were required to have an offline $p_{\mathrm{T}} > 20$ GeV (minimum jet p_{T} was set at this stage to allow overlap removal as per 6.5.6). It was also required that any jets lie within the combined ATLAS calorimeter and inner tracker coverage of $|\eta| < 2.5$. This was necessary to allow the use of B-tagging, while $t\bar{t}$ events are also typically produced at central values of η.

6.5.3 Missing Et

Missing E_{T} in each event was calculated via the MET_RefFinal method (which uses a refined calibration). This takes input cells, associates them with reconstructed

objects (which are ordered electron, photon, hadronic tau, jet and muon) and then replaces the original cell calibration with that from the relevant reconstructed object (which is considered to be better known [66]). Cells are only associated with the first valid reconstructed object (if they contribute to several different objects) so as to prevent overlaps in the missing E_{T} calculation. The calculation carries out separate sums for the E_{x} and E_{y} components of the total missing E_{T}, with all cells being included. Any cells which do not form part of any reconstructed object have a global calibration applied. A 20 GeV base missing E_{T} cut was required.

6.5.4 Electron

Electrons are reconstructed in ATLAS events via three different algorithms. 'Standard electrons' are produced via a cluster based algorithm used to identify high energy isolated electrons in the EM calorimeter [67]. 'Soft electrons' are produced by an algorithm, seeded from an inner detector track, intended to identify either low energy electrons or electrons originating from a hadron jet. The third algorithm focuses on identifying electrons produced in the forward region of the detector. For the purposes of the selection applied here, electron candidates were required to originate from either the standard or soft algorithm. Candidates were required to possess an offline $p_{\mathrm{T}} > 20$ GeV and lie within $|\eta| < 2.5$ but not in the calorimeter crack region of $1.37 < |\eta| < 1.52$. In addition, they were required to pass the medium level 'isEM' quality cuts comprising a series of calorimeter isolation and shower shape cuts together with limited tracking constraints. Finally, a futher isolation requirement

was added by requiring the etcone20 (total E_{T} contained within a cone of ΔR <0.2 around the cluster [56]) variable to have a value $> 4 + 0.023\times$(candidate offline p_{T}), while the track matched to the calorimeter cluster was required to have a value for E/p_{T} of the correct size for an electron plus a hit in the B-layer (first layer of the tracker pixels where the track should cross an active detector).

6.5.5 Muon

A number of different muon reconstruction algorithms are available within ATLAS which are split into two groups. These are 'standalone' muons which only use information from the muon spectrometer, and 'combined' muons which use the muon spectrometer in association with the inner detectors. Here 'MuID' (Muon IDentification) muons were taken as the starting point, which combine the muon spectrometer tracks with inner detector tracks and calorimeter deposits. Selected muons (with author of 12) were required to pass the tight quality cuts, whilst possessing an offline $p_{\mathrm{T}} > 20$ GeV and $|\eta| < 2.5$. In addition, two futher isolation constraints were applied by requiring the variables Ptcone30 (total track p_{T} in a cone of ΔR <0.3 around the muon candidate excluding the muon track) and Etcone30 (total calorimeter E_{T} in a cone of ΔR <0.3 around the muon candidate) to be smaller than 4 GeV.

6.5.6 Overlap Removal

Each aspect of the ATLAS reconstruction considers the detector signatures independently. Consequently, providing the relevant constraints are passed, a particular set of signatures in the detector could be simultaneously reconstructed as (for example) an electron, tau and jet. To avoid double counting, a process of overlap removal was carried out. For electrons-jet and muon-jet overlaps the same procedure was followed as per [56] with removal based on spatial matching. Any selected jet located within $\triangle$R<0.2 of a selected electron was removed. Likewise, any selected muon located withing $\triangle$R<0.4 of a selected jet was then also removed. In addition, further overlaps were processed with respect to the selected taus. Any selected tau found within $\triangle$R<0.2 of a remaining selected electron was removed. Then any remaining selected jet within $\triangle$R<0.4 of the remaining good taus was removed. Finally, any muons remaining within $\triangle$R<0.4 of a selected tau were removed.

6.6 Event Selections

6.6.1 Choice of $t\bar{t}$ channel

As discussed in 1.5 $t\bar{t}$ events are characterised by the decay of the W-bosons coming from the two top quarks. Consequently there are three different classes of $t\bar{t}$ events featuring taus:

- Tau + jets : One of the W-bosons decays to a hadronic tau and the sec-

ond decays to a quark pair. The event is characterised by the presence of a hadronic tau, four jets (of which two are b-jets) and significant missing E_{T} as a consequence of the neutrino produced in the tau decay.

- Tau + lepton : One W-boson decays to a hadronic tau with the second decaying to either an electron or a muon. As such the event signature comprises a hadronic tau, single high energy lepton, two b-jets and missing E_{T} arising from the neutrinos produced in both W decays.

- Two tau events : Both W-bosons decay to hadronic taus. Two b-jets are also produced and large missing E_{T} observed.

It should be noted that for the purposes of this analysis a tau was interpreted as the hadronically decaying cases only. Taus decaying to leptons were lumped in with the standard leptonic modes as they are virtually indistinguishable from an experimental viewpoint.

Of the three event topologies, the tau + jets and tau + lepton cases are the most useful. Both have positive and negative points associated with them. The tau + jets channel has the advantage that one of the top quarks in the $t\bar{t}$ pair decays hadronically and so can be fully reconstructed. This has the advantage that plotting the invariant mass of the hadronic top provides a method of verifying whether selected events do indeed come from a $t\bar{t}$ pair. However, the signature for this channel comprises a hadronic tau, four hadron jets and missing E_{T}. Consequently, it would be expected to suffer badly from QCD backgrounds in the enviroment of a proton collider. Considering the tau + lepton channel, the situations are largely reversed.

In this case a hard lepton is produced in the event, which both allows for easy triggering and also acts as a powerful supression against QCD. However, neither of the top quarks can be fully reconstructed, thereby making it more difficult to verify the $t\bar{t}$ content of any events passing a given selection. Furthermore, the tau + lepton channel is known to suffer a significant cross talk background from the other decay channels of the $t\bar{t}$ pair which is difficult to remove [68]. Table 6.1 shows the number of events which pass basic preselections for tau + jets and tau + lepton channels when a small test study was carried out for 1000 $t\bar{t}$ events. For the former the selection to be described in 6.6.2 was used whereas for the latter exactly one good selected tau and lepton were required, together with two good jets and missing E_{T} greater than 20 GeV. As can be seen, for the tau + lepton selection the signal only makes up 20% of the events passing.

Channel	Events passing (tau + jets selection)	Events passing (tau + lepton selection)
Tau + jets	380	33
Tau + lepton	21	124
Double tau	6	7
Lepton + jets	265	513
Dilepton	7	74
S/B	1.27	0.2

Table 6.1: Comparison of the number of events in different $t\bar{t}$ signal channels passing preselections for tau + jets and tau + lepton events

Two tau events suffer the same disadvantages as both of the other two channels in that they do not contain a lepton for QCD supression and neither top quark can be fully reconstructed.

The remainder of this chapter describes a technique developed to allow a measurement of the $t\bar{t}$ cross section from the tau + jets channel, including an estimate of the QCD background to the channel from data. The analysis was deliberately developed to use simple cuts which were considered to be safe in the early ATLAS data. Multivariant techniques were therefore deliberately avoided.

6.6.2 Tau + Jets Channel Preselection

As described above, the tau + jets channel in the decay of a $t\bar{t}$ decay is characterised by the presence of a hadronically decaying tau lepton, two jets originating from b quarks, two light quark jets (plus any additional jets produced by gluon radiation) and a degree of missing E_{T} due to the presence of neutrinos associated with the $W \rightarrow \tau$ decay. An initial event preselection was therefore introduced, in addition to the object selections already described, to discard any events which did not fit in to the expected tau + jets topology. The cuts applied were as follows:

- Require exactly one good 1-Prong tau, passing the tight hadronic tau selection and with p_{T} >20 GeV.
- Veto any event containing either a good electron or good muon (as described in the object selections) with p_{T} >20 GeV.
- Demand at least four good jets with p_{T} >20 GeV, of which at least three possess p_{T} >40 GeV.
- Require a minimum of 20 GeV missing E_{T}.

While the base pre-selection alone removes a large proportion of the non top-like backgrounds, such as low multiplicity QCD and W/Z+jets events where the W bosons decay to real leptons within coverage, several further cuts are required to aid isolation of the signal channel.

6.6.3 Missing E_{T} and event scalar E_{T}

Two techniques which can be used to further suppress background from QCD multijet processes are by raising the cut on the event missing E_{T} and by cutting on the total scalar E_{T} of the event.

In a pure QCD process, energetic neutrinos are not expected to be produced. As a consequence, it would not be expected for large amounts of missing E_{T} to feature in such events. Fig. 6.3 shows missing E_{T} plotted versus three jet mass (for the combination with the highest combined p_{T}, see 6.7.1 for details) for the Monte Carlo $t\bar{t}$ dataset and the Pythia QCD samples. Requiring missing $E_{\mathrm{T}} > 50$ GeV cuts out a significant portion of the $t\bar{t}$ signal, but almost entirely removes the remaining low energy QCD events from the region where cross sections are expected to be large.

The total scalar E_{T} of each event was formed by summing the individual E_{T}'s of the selected tau candidate with that of the four highest p_{T} jets and the missing E_{T}. It can be seen from Fig. 6.4 how putting an upper cut on the total scalar E_{T} at 500 GeV controls the high energy part of the QCD spectrum without significantly cutting into the $t\bar{t}$ signal region.

Combining the two variables, candidate events were required to have missing $E_{\mathrm{T}} >$ 50 GeV and an event scalar $E_{\mathrm{T}} < 500$ GeV.

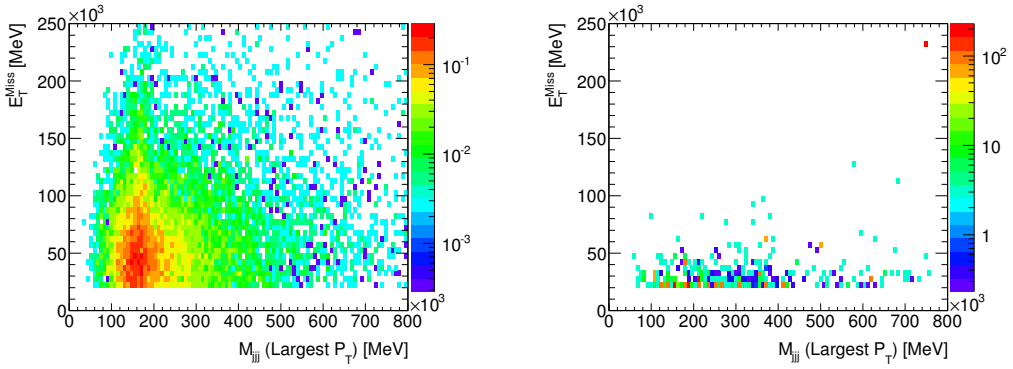

(a) $t\bar{t}$ *(b)* Pythia QCD

Figure 6.3: Correlation between the missing E_{T} and the three jet mass m_{jjj} with the highest combined p_{T} for Monte Carlo $t\bar{t}$ events and Pythia QCD samples. Plots are normalised to 26.4 pb^{-1}

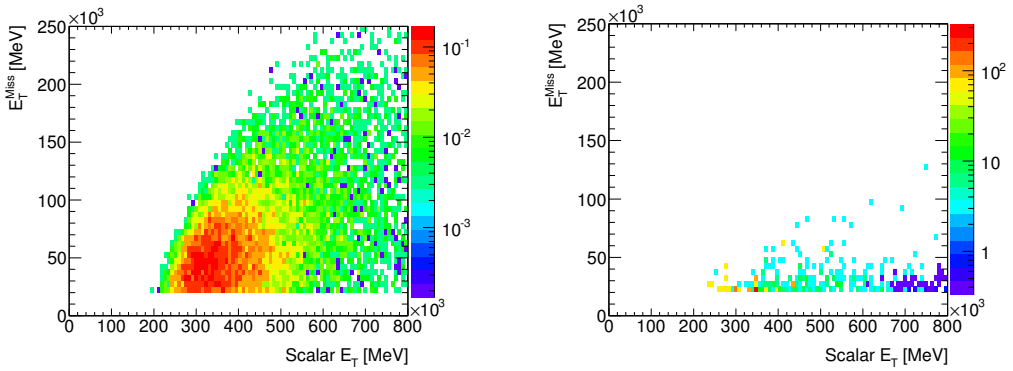

(a) $t\bar{t}$ *(b)* Pythia QCD

Figure 6.4: Correlation between the missing E_{T} and the event scalar E_{T} for Monte Carlo $t\bar{t}$ events and Pythia QCD samples. Plots are normalised to 26.4 pb^{-1}

6.6.4 Transverse Mass Cut

It is possible to calculate the transverse mass of the tau candidate and the event missing E_{T} via;

$$m_{\mathrm{T}} = \sqrt{(E_{\tau} + E^{\mathrm{T}}_{\mathrm{miss}})^2 - ((p_{\mathrm{x}_{\tau}} + E^{\mathrm{x}}_{\mathrm{miss}})^2 + (p_{\mathrm{y}_{\tau}} + E^{\mathrm{y}}_{\mathrm{miss}})^2)}. \tag{6.1}$$

The main purpose of calculating the transverse mass was to provide a means of reducing the self contamination of the tau + jets channel from the other decay modes of the $t\bar{t}$ pair. Fig. 6.5 illustrates the transverse mass plotted for the tau + jets case when compared to the other decays of the top pair which pass the preselection. In the case of the tau + jets channel the distribution is roughly constant from zero up to around 70 GeV and then falls away for values above this. In contrast, for the semileptonic decays with no truth taus present in the decay (and also to a less extreme degree for the dileptonic decays), the distribution is seen to be strongly peaked at around 80 GeV. Consequently, it was required that events should have a transverse mass for the tau and missing $E_{\mathrm{T}} < 60$ GeV. Whilst this increases the signal purity, it also helps to remove any other background where the transverse mass of the missing E_{T} and the tau candidate should fall above the cut value.

6.6.5 B Tagging

ATLAS makes use of a variety of algorithms designed to identify hadronic jets originating from or containing b quarks/mesons. Of these methods the so called 'SV0' tagger uses the long lifetime of b-quark to search for b-jets. B-quark lifetimes

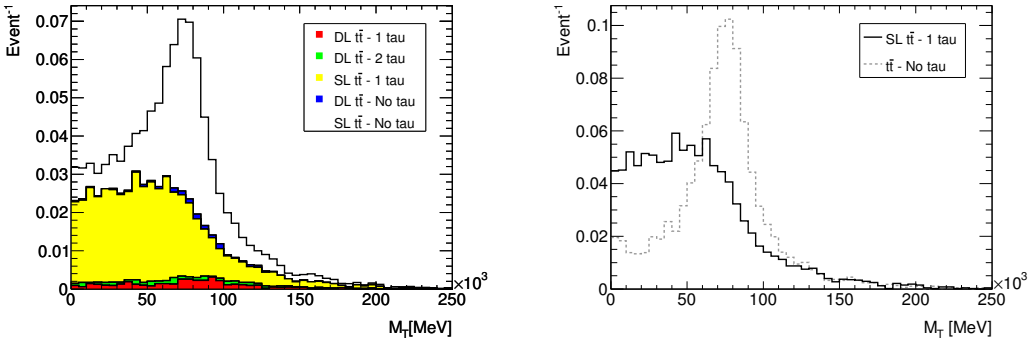

(a) *(b)*

Figure 6.5: Transverse mass of the tau and missing E_{T} in non-hadronic Monte Carlo $t\bar{t}$ events. Shown in 6.5(a) is a breakdown of all the channels within the sample while 6.5(b) shows the distribution for tau + jets events when compared to the modes where no truth hadronic tau is present. Plots are normalised to unit area

are sufficiently long that a b-hadron can travel for a few mm before it decays [56], which can therefore produce a secondary vertex displaced from the jet origin at the point were the decay takes place. SV0 is the simplest of the ATLAS secondary vertex taggers [69] and was considered safe for use in the 2010 data [56]. It returns a weight for each jet which is the signed decay length significance [69] of the displaced vertex relative to the main jet origin. The likelihood that a jet originated from a b-quark can therefore be established by a cut on the SV0 weight. Jets possessing a weight > 5.72 can be said to have a 50% chance of originating from a b [56]. As the genuine tau + jets events should contain two b-jets, it was therefore required that at least one, but no more than two, jets in a candidate event possess an SV0 weight > 5.72. Approximately two thirds of genuine tau + jets events are expected to pass this cut.

6.6.6 Trigger

During 2010 running the trigger menus used evolved with the ramping up of the LHC machine luminosity. As a consequence, triggers varied between luminosity periods and were different to those that had been implemented within the Monte Carlo productions. During periods H and I the two lowest unprescaled triggers most suitable for this analysis were EF_xe40_noMu and tau16_medium_xe22_noMu. The former is chained to L2_xe30_noMu and L1_XE25 as the LVL2 and LVL1 components respectively. For the latter the chain was built from L1_XE25. It is expected that any events remaining after the complete set of offline selection cuts would have passed either one or both of these triggers.

6.6.7 Cut flow and purity

After application of the pre-selection and the additional cuts, the overall semi and dileptonic $t\bar{t}$ signal selection efficiency is seen to be 4×10^{-3}, with a signal purity for the tau + jets channel of 63% in $t\bar{t}$ events (excluding the fully hadronic decays). Fig. 6.6 shows the cut flow for the different components of the $t\bar{t}$ sample. Table 6.2 shows the number of signal and background events expected to pass the selection, excluding QCD backgrounds, for a range of integrated luminosities. Results from the samples generated with Pythia [40], although scaled by large factors, showed that the size of the QCD background would be expected to be of a similar order to the signal.

Process	Expected Events					
	10 pb^{-1}	26.4 pb^{-1}	40 pb^{-1}	100 pb^{-1}	200 pb^{-1}	1 fb^{-1}
$t\bar{t}$	3.7	9.76	14.79	36.97	73.94	369.72
W+jets	0.19	0.49	0.75	1.87	3.75	18.73
Single top	0.13	0.34	0.52	1.3	2.6	12.99
Z+jets	0.03	0.09	0.14	0.34	0.68	3.42
W+bb+jets	0.02	0.07	0.1	0.25	0.49	2.47
Diboson	0	0.01	0.01	0.02	0.05	0.29
Hadronic top	0.17	0.45	0.68	1.71	3.42	17.11
Total background	0.55	1.45	2.2	5.5	10.99	55.01

Table 6.2: Number of Monte Carlo signal and background events expected to pass the selection for a range of integrated luminosities (excluding QCD backgrounds)

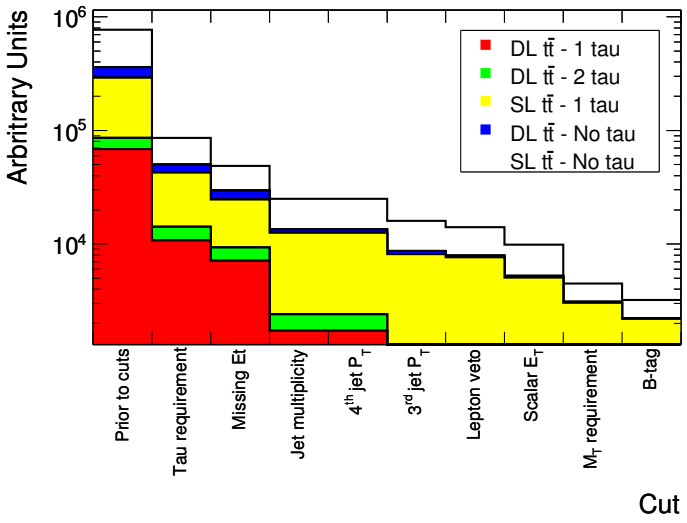

Figure 6.6: Cut flow for non-hadronic $t\bar{t}$ events passing the complete event selection, broken down into the sample components. Numbers shown are for the complete Monte Carlo sample totaling 773167 events

6.7 Cross Section Measurement and QCD Background Estimation

The $t\bar{t}$ cross section can be calculated via a counting experiment by use of the equation;

$$\sigma_{t\bar{t}} = \frac{N_{\text{Data}} - N_{\text{Background}}}{\varepsilon \mathcal{L}} \tag{6.2}$$

where N_{Data} is the number of events observed in a chosen signal region, $N_{\text{Background}}$ is the number of background events in that region (estimated via a combination of Monte Carlo and data driven methods), ε is the efficiency with which signal events are expected to be selected in that region (estimated from Monte Carlo) and $\mathcal{L}$ is the integrated luminosity of the data sample.

6.7.1 Hadronic Top Mass Reconstruction

Having selected the tau + jets channel events, it is possible to reconstruct the top which decays hadronically. A common technique for doing this is to form the three jets in the event which possess the highest combined three jet p_{T} [70]. This procedure has been demonstrated to find the correct combination in approximately 35% of lepton + jets events [70]. This distribution is shown in Fig. 6.7 for the Monte Carlo $t\bar{t}$ signal and Monte Carlo backgrounds (excluding QCD) when scaled to an integrated luminosity of 26.4 pb^{-1}.

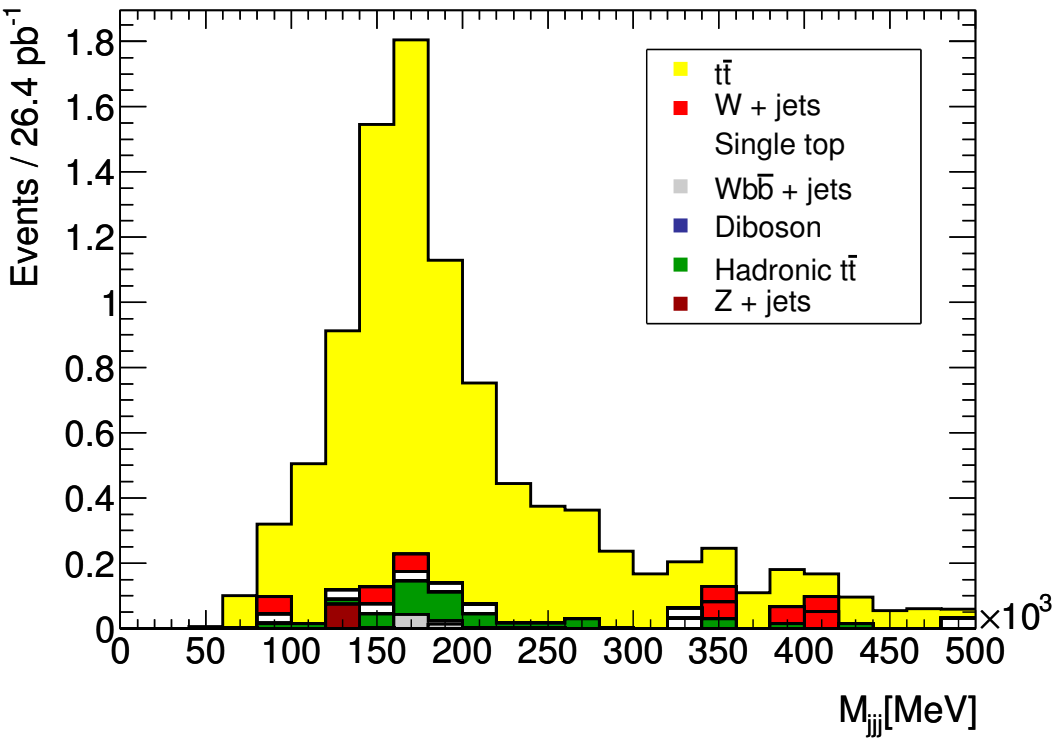

Figure 6.7: m_{jjj} distribution for the highest combined three jet p_{T} in non-hadronic $t\bar{t}$ events and main backgrounds with the exception of QCD. Normalised to 26.4 pb^{-1}

6.7.2 Defining signal region and data driven estimate of QCD background

By reconstructing the hadronic top in the selected events, it was possible to use a window around the top mass (currently measured as $m_{\mathrm{t}} = 172.0 \pm 0.9 \pm 1.3$ GeV [9]) to obtain a value for N_{Data}. In order to estimate the QCD contribution to this region, the number of events was examined in the signal region in a QCD enriched sample and then subtracted from N_{Data} after normalising to a sideband in the mass distribution and correcting for any signal found in the diluted sample.

To produce a sample containing a QCD enriched three jet mass (m_{jjj}) distribution it was necessary to find a variable which, when adjusted, would alter the proportion of QCD and signal in the top m_{jjj} plot but without altering the shape of the distributions. This was achieved through the SV0 b-tag used as the last step of the selection procedure. Shown in Fig. 6.8 are the plots of m_{jjj} for the signal, taken from the Monte Carlo, for the usual described b-tagged selection in 6.8(a), and for an anti b-tagged selection in 6.8(b). The anti-tagged selection shown in 6.8(b) used exactly the same cuts, but with events required to fail the final b-tag contraint. As can be seen the shapes of the distributions are roughly consistent, with the ratio of anti-tagged to tagged events being approximately 0.4. In order to check the same was true for the background, the equivalent plots were produced for the data as shown in Fig. 6.9. The missing E_{T} selection used to produce these plots was changed from the standard >50 GeV cut, to requiring missing E_{T} to lie in the window $20 < E_{\mathrm{T}}^{\mathrm{miss}} < 30$ GeV so as to select a sample highly populated by QCD. The fact that the

tagged and anti-tagged background shapes shown in Fig. 6.9 are the same is important as it the assumption that the b-tag does not alter the shape which is used in the method proposed for accounting for the QCD background in the signal.

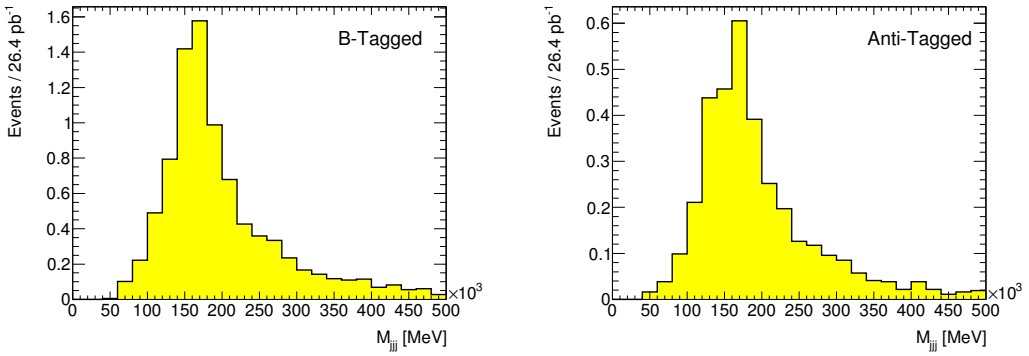

(a) *(b)*

Figure 6.8: Monte Carlo distributions for m_{jjj} possessing the highest combined three jet p_{T} in non-hadronic $t\bar{t}$ events for SV0 b-tagged 6.8(a) and anti-tagged 6.8(b) selections. Plots are normalised to 26.4 pb^{-1}

To calculate the cross section and carry out the subtraction of the QCD background, plots of m_{jjj} were produced for the standard tagged selection and in addition for the anti-tagged events. A window around the top mass peak from 100 GeV to 250 GeV was defined to be used to measure N_{Data} in the b-tagged plot. A sideband region, where the $t\bar{t}$ contribution is expected to be negligible was also defined from 400 GeV to 500 GeV. Although the contribution of the signal in the sidebands was expected to be negligible, the strength of the cuts required to suppress the QCD contribution before the b-tag meant that the contribution from $t\bar{t}$ in the signal region of the antitag distribution was non-negligible. This therefore had to be taken into account

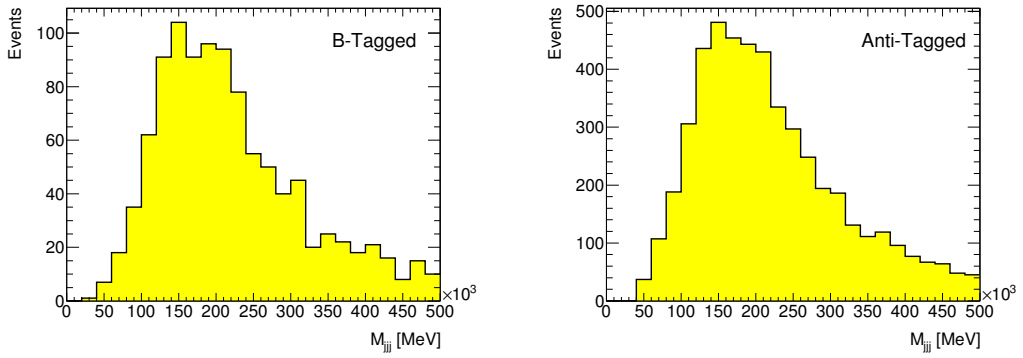

(a) *(b)*

Figure 6.9: Data distributions for m_{jjj} possessing the highest combined three jet p_{T} after the complete SV0 b-tagged 6.9(a) and anti-tagged 6.9(b) selections but for the requirement $20 < E_{\mathrm{T}}^{\mathrm{miss}} < 30$ GeV. The integrated luminosity was 26.4 pb^{-1}

as part of the background subtraction procedure. It was possible to parameterise the $t\bar{t}$ and QCD contributions in the tagged and anti-tagged samples as per Fig. 6.10.

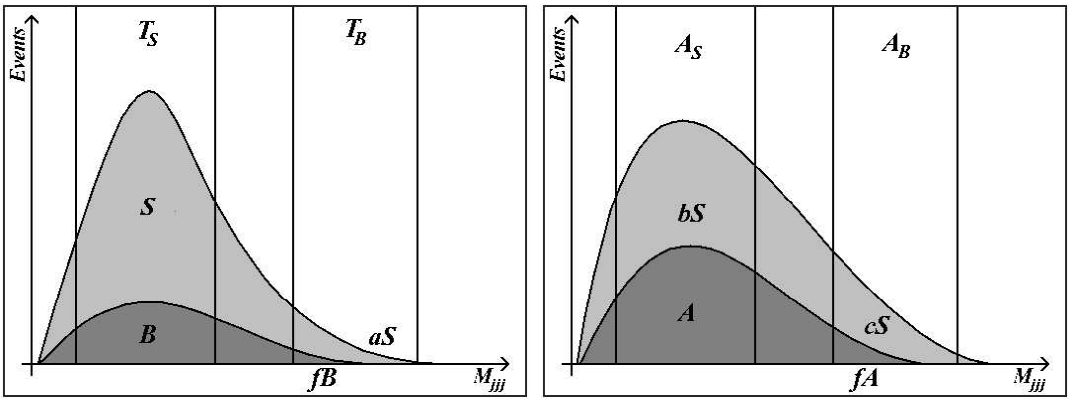

(a) B-tagged *(b)* Anti-tagged

Figure 6.10: Schematic diagrams illustrating the variable assignment in the SV0 B-tagged 6.10(a) and anti-tagged 6.10(b) samples for the signal and sideband regions

Here $T_{\rm S}$, $T_{\rm B}$, $A_{\rm S}$ and $A_{\rm B}$ are the number of events observed in the signal and sideband regions for the tagged and anti-tagged samples. S is the number of $t\bar{t}$ events present in the signal region of the tagged distribution and B is the number of QCD background events in the same region. A is the number of QCD events in the signal region of the anti-tagged sample. f represents the ratio of QCD in the signal region to the sideband region, which is the same for both the tagged and anti-tagged cases. Of the variables, $T_{\rm S}$, $T_{\rm B}$, $A_{\rm S}$ and $A_{\rm B}$ are measured from the data plots, the ratios a, b and $c$can be extracted from the $t\bar{t}$ Monte Carlo and S, B, $A$and f are unknowns. The measureables $T_{\rm S}$, $T_{\rm B}$, $A_{\rm S}$ and $A_{\rm B}$ can be expressed in tems of the other variables by;

$$T_{\rm S} = S + B \tag{6.3}$$

$$T_{\rm B} = aS + fB \tag{6.4}$$

$$A_{\rm S} = bS + A \tag{6.5}$$

$$A_{\rm B} = cS + fA. \tag{6.6}$$

Fig. 6.8 shows the distributions for the tagged and anti-tagged $t\bar{t}$ samples, given by the $t\bar{t}$ Monte Carlo, normalised to 26.4 pb^{-1}. These plots show that the signal contribution to the sideband region is expected to be negligible in both cases.

Neglecting the signal contributions in the sidebands therefore allows equations 6.4 and 6.6 to be simplified to;

$$T_{\mathrm{B}} = fB \tag{6.7}$$

$$A_{\mathrm{B}} = fA. \tag{6.8}$$

It is possible to define a new variable, N_{Calc}, which is given as;

$$N_{\mathrm{Calc}} = N_{\mathrm{Data}} - N^{\mathrm{Scaled}}_{\mathrm{Anti-Tag}}. \tag{6.9}$$

Taking N_{Data} as T_{S}, the number of events measured in the signal region of the b-tagged plot, and $N^{\mathrm{Scaled}}_{\mathrm{Anti-Tag}}$ as the number of anti-tagged events in the same region scaled by the ratio of the events seen in the sidebands, it is possible to write;

$$N_{\mathrm{Calc}} = T_{\mathrm{S}} - \frac{T_{\mathrm{B}}}{A_{\mathrm{B}}} A_{\mathrm{S}} = (S + B) - \left(\frac{fB}{fA}\right)(bS + A) \tag{6.10}$$

and therefore rearranging;

$$N_{\mathrm{Calc}} = T_{\mathrm{S}} - \frac{T_{\mathrm{B}}}{A_{\mathrm{B}}} A_{\mathrm{S}} = S\left(1 - b\frac{B}{A}\right). \tag{6.11}$$

Consequently, by using 6.7 and , the number of non-QCD events, S, in the signal region of the b-tagged sample can be expressed as;

$$S = \frac{\left(T_{\mathrm{S}} - \frac{T_{\mathrm{B}}}{A_{\mathrm{B}}} A_{\mathrm{S}}\right)}{\left(1 - b\frac{T_{\mathrm{B}}}{A_{\mathrm{B}}}\right)}. \tag{6.12}$$

Running over the ATLAS data periods H and I, the m_{jjj} distributions produced for the tagged and anti-tagged samples are shown in Fig. 6.11. Reading off the number of events in each distribution for both the signal and sideband regions produced the numbers shown in table 6.3.

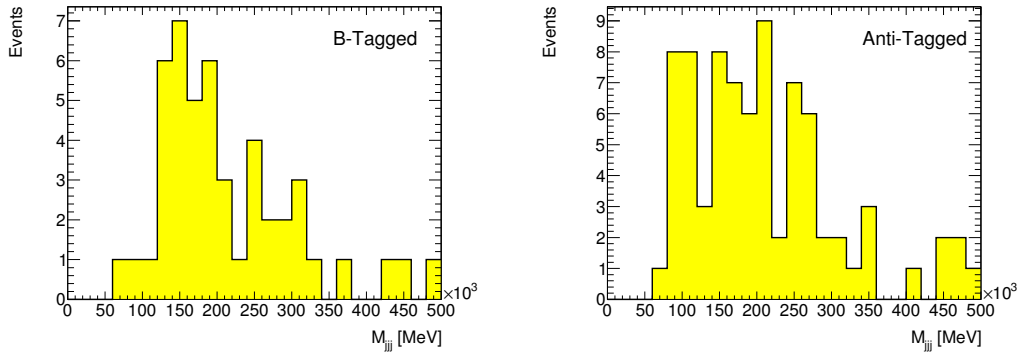

(a) *(b)*

Figure 6.11: Data distributions for m_{jjj} possessing the highest combined three jet p_{T} after the complete SV0 b-tagged 6.11(a) and anti-tagged 6.11(b) selections. The integrated luminosity was 26.4 pb^{-1}

The statistical errors were produced by taking each of T_{S}, T_{B}, A_{S} and A_{B} to be the mean value of a poisson distribution. The uncertainties were then formed using a 68% confidence interval on the mean value.

A value for b was produced by taking the ratio of the events in the signal region for the tagged and anti-tagged samples, via the non luminosity-scaled version of the

Region	Events
T_{S}	$31^{+6.6}_{-5.5}$
T_{B}	$3^{+2.9}_{-1.6}$
A_{S}	$46^{+7.8}_{-6.8}$
A_{B}	$6^{+3.6}_{-2.4}$

Table 6.3: Number of events produced in data for the signal and sideband regions for tagged and anti-tagged selections. Integrated luminosity totaled 26.4 pb^{-1}

plots shown in Fig. 6.8. This gave a value for b of 0.399 ± 0.015.

In order to produce a value for S the measured numbers from table 6.3 together with the value for b were substituted into equation 6.12, yielding a value for S of 10 events. To estimate the statistical error on the value, a toy Monte Carlo was used to carry out a large number of pseudo-experiments where T_{S}, T_{B}, A_{S} and A_{B} were all taken as input mean values of four poisson distributions. A random generator was used in each pseudo-experiment to produce new values for T_{S}, T_{B}, A_{S} and A_{B} which were combined with b to produce a new value for S. After many experiments, a 68% confidence band was applied to the resulting distribution for the generated values of S. Reading off the upper and lower values of the interval resulted in a measurement of S of 10^{+15}_{-32} events. As can be seen, a statistical error of the order of between 150 and 300% is produced on S, which is a direct consequence of the small number of events seen in the data in the sideband region for both the b-tagged and anti-tagged (background enriched) distributions.

The statistical error on S is such that it is not possible to produce a statistically

significant measurement of $\sigma_{t\bar{t}}$ via this channel with the current ATLAS dataset. A 'nominal' value of the cross-section was still calculated however, so as to demonstate the method. The value S represents the number of non-QCD events in the top signal window. Consequently, the equation for calculating the $t\bar{t}$ non all hadronic cross-section given in 6.2 can be re-written as;

$$\sigma_{t\bar{t}} = \frac{S - \Sigma N_{\text{Background}}^{\text{Non-QCD}}}{\varepsilon \mathcal{L}} \tag{6.13}$$

where $\Sigma N_{\text{Background}}^{\text{Non-QCD}}$ is the sum of the non-QCD backgrounds, which are small and were taken from Monte Carlo for the signal region. These are shown in table 6.4.

Process	Expected Events / 26.4 pb^{-1}
W+jets	0.12
Single top	0.15
Z+jets	0.09
W+bb+jets	0.07
Diboson	0.01
Hadronic top	0.32
Total background	0.76

Table 6.4: Number of Monte Carlo non-QCD background events expected to pass the selection for an integrated luminosities of 26.4 pb^{-1}

The efficiency ε for non-hadronic $t\bar{t}$ events to pass the selection cuts and end up in the signal region of the tagged m_{jjj} plot was also calculated from Monte Carlo via Fig. 6.8(a) and was found to be $3.1 \times 10^{-3} \pm 0.1 \times 10^{-3}$, where a binomial error is

assumed. The luminosity $\mathcal{L}$ was taken from machine parameters [71] where recent measurements have put the error on the luminosity scale during 2010 at $\pm 3.4\%$ [71].

Combining everything together, a value for the $t\bar{t}$ non-fully hadronic cross section $\times$ BF (where BF is the branching fraction), was produced of;

$$\sigma_{\mathrm{t\bar{t}}} \times \mathrm{BF}_{\mathit{Non\ all\ hadronic}} = 113^{+183}_{-390}\mathrm{pb} \tag{6.14}$$

It should be noted that this measurement is taken for an efficiency that, while enriched in tau + jets, is calculated for a mixture of $t\bar{t}$ channels. Ultimately, once the measurement became statistically valid it would be necessary to subtract the contribution from the other modes (preferably via use of consistent measurements of those channels) and so hence forth obtain a value for the pure $t \rightarrow \tau$ cross section.

Scaling the non-fully hadronic value produced here by the theoretical branching fraction from the Monte Carlo of 0.543, a nominal value for the total $t\bar{t}$ cross-section is found to be;

$$\sigma_{\mathrm{t\bar{t}}} = 207^{+337}_{-718}\mathrm{pb} \tag{6.15}$$

As discussed, the statistical error on S means that it is not possible to claim a measurement of $\sigma_{\mathrm{t\bar{t}}}$ via this method with the 26.4 pb^{-1} of data taken during 2010. However, as the values calculated for$S$ and $\sigma_{\mathrm{t\bar{t}}}$ produce an output of the correct order expected it is possible to carry out a simple extrapolation to estimate whether

a measurement would become achievable in the near future for ATLAS. Table 6.5 gives an estimate of how the errors on S would be expected to evolve with luminosity. Here S, T_{S}, T_{B}, A_{S} and A_{B} have been simply scaled by appropriate factors to account for the luminosity scaling, with the statistical error on S again calculated in the form of a 68% confidence band via the toy Monte Carlo.

Value	Events/26.4 pb^{-1}	Events/200 pb^{-1}	Events/500 pb^{-1}	Events/1 fb^{-1}	Events/3 fb^{-1}
S	10^{+15}_{-32}	76^{+44}_{-26}	189^{+84}_{-99}	379^{+111}_{-139}	1135^{+220}_{-227}

Table 6.5: Projected evolution of S with increasing luminosity, assuming a simple upscaling of the values for T_{S}, T_{B}, A_{S} and A_{B}

It can be seen that once 500 $\mathrm{pb}^{-1}$of data have been collected the 68% confidence band representing the statistical uncertainty on S has become of approximately the same order of magnitude as the signal. Thus, with an unimproved technique it is possible to achieve an approximate two standard deviation significance for 500 $\mathrm{pb}^{-1}$of data. Once 3 fb^{-1} have been collected this uncertainty band reduces to approximately 40% of the extrapolated value of S, thus corresponding to a fractional statistical error of 20%. Thus a measurement of $\sigma_{\mathrm{t\bar{t}}}$ via the method described would begin to become statistically feasable once ATLAS has collected of the order of 1 fb^{-1} to 3 fb^{-1} of data. This is expected to be achieved during the course of the current 2011 - 2013 LHC run. With refinements to the analysis techniques, discussed in 6.7.4 it is possible that a result could be produced earlier.

6.7.3 Systematic uncertainty on the efficiency

As has been seen, for the immediate future any attempted measurement of the $t\bar{t}$ cross section from the tau + jets decay channel is likely to be limited by the size of the statistical error. Nevertheless, as the efficiency ε is calculated directly from Monte Carlo in this analysis, it is interesting to obtain a first estimate of the magnitude of the systematic error on ε for when the amount of available data has increased. Some of the expected main sources of systematic error on ε were therefore examined.

Jet Energy Scale

The analysis described uses a selection which relies on jet p_{T} cuts, a scalar sum of jet energies and a large missing E_{T} cut. With the efficiency ε being taken entirely from Monte Carlo, a potential source of systematic uncertainty exists due to deviations between the simulated and actual jet energies measured by the ATLAS detector. During 2010 running, it was estimated that the error on the ATLAS jet energy scale lay in the region of 5%, with a slight variation observed as a function of p_{T} and η [72]. For the jet p_{T} range of interest for this measurement (approximately 20 GeV to 80 GeV) this was expected to be closer to the order of 5%. The effects of a 5% uncertainties in the jet energy scale (JES) was therefore considered.

One way of simulating a shift in the JES would be to fully rescale all the jet candidates before any analysis was carried out by $\pm$ a chosen scale factor, including recalculating the missing E_{T}. In this case the energy scale shift was studied by

simultaneously shifting of the cuts dependent on the jet energy. This included assuming the hadronic tau energy scale to also have an uncertainty equivalent to that of the main JES. For example, to represent a 5% underestimation of the JES, the jet p_{T}, tau p_{T} and missing E_{T} cuts were all lowered by 5%, as were the upper and lower bounds of the top m_{jjj} signal region, while the scalar E_{T} and transverse mass cut values were increased by 5%. This adjustment included the cuts used in the object preselections. Table 6.6 shows the effect of the ±5% JES uncertainties on the efficiency.

JES shift	$\Delta\varepsilon/\varepsilon$
+5%	-33%
-5%	+42%

Table 6.6: Fractional uncertainty on the efficiency as a result of a ±5% shift in the jet energy scale

It can be seen that a 5% shift in the JES as modelled here produces a very significant fractional error on ε. However, the scaling technique used means that this is possibly a conservative estimate (for example missing E_{T} is not calculated entirely from jets but is still scaled up by the same amount). Furthermore, while the current estimate of the JES uncertainty is of the order of 5%, this will improve as the detector is better understood, with the aim for ATLAS ultimately to have a JES uncertainty of 1% [35]. At the same time aspects of the analysis could be considered so as to try and reduce the sensitivity to the JES. One possible way of doing this would be to try and loosen some of the jet based cuts.

Monte Carlo Modelling

The Monte Carlo $t\bar{t}$ dataset used as the default throughout the course of this analysis was as per that described in 6.2 where the generators used were MC@NLO (to provide the matrix element) and Herwig/Jimmy to provide the parton showering. The PDF CTEQ6.6 was also used. To examine the effect of different generator/PDF sets, the efficiency was recalculated for two new datasets, both of which simulated the non-fully hadronic $t\bar{t}$ with decays to electons, muons and tau final states allowed. The first sample considered [3] used a matrix element provided by POWHEG [73] with parton showering provided via Herwig [41] and PDF based on CTEQ6L1 [74]. A fractional difference for the efficiency calculated via this dataset compared to the default was seen to be +6%. The second control sample considered [4] used AcerMC [75] to provide the matrix element with Pythia [40] giving the parton shower and the PDF used was based on the MRST [76] case. Recalculating the efficiency for this sample produced a fractional difference when compared to the main Monte Carlo of +1%. Although there are many different PDF sets and generators which could be examined, these two results show that the systematic error on the $t\bar{t}$ efficiency would be expected to be of the order of 5%.

[3] mc09_7TeV.105860.TTbar_PowHeg_Jimmy.merge.log.e540_s765_s767_r1302_r1306

[4] mc09_7TeV.105205.AcerMCttbar.merge.log.e552_s765_s767_r1302_r1306

Matrix Element	Parton Shower	PDF Type	$\Delta\varepsilon/\varepsilon$
POWHEG	Herwig	CTEQ6L1	+6%
AcerMC	Pythia	MRST	+1%

Table 6.7: Fractional uncertainty on the efficiency for two different generator and PDF combinations

Top Quark Mass

The $t\bar{t}$ efficiency is calculated based on the fraction of events ending up in the 100-250 GeV mass window of the m_{jjj} plot. As a consequence of this it could be sensitive to systematic shifts in the location of the top mass peak. In addition, many of the cuts used in the event preselection would also be sensitive to a shift in the top mass as it would be expected to have an effect on the energy spectra of the top decay products. To test this a series of samples were available which were simulated with the same generator settings as per the standard samples, but for a range of different top masses. Table 6.8 shows the fractional change in the efficiency as a result of changing the top mass (compared to the 172.5 GeV mass of the standard $t\bar{t}$ sample) by $^{+2.5}_{-5}$ GeV. As the current statistical and systematic errors on the measured top mass at the TeVatron are each of the order of ± 1 GeV [9] this is a conservative estimate.

As the TeVatron experiments have measured the real value of the top quark mass to an accuracy of the order 1-2 GeV, then it is unrealistic to use the complete fractional error given by the 5 GeV shift as part of an overall systematic error calculation. From the size of the uncertainty produced by the +2.5 GeV shift, it would be reasonable

Mass Shift	$\Delta\varepsilon/\varepsilon$
+2.5 GeV	+7.5%
-5.0 GeV	-19%

Table 6.8: Fractional uncertainty on the efficiency as a result of a shift in the top quark mass

to expect a variation on ε to be of the order of 10% for a -2.5 GeV shift in the top mass.

B-tagging efficiency

The SV0 *b*-tag used in the analysis as set was expected to give a b-jet efficiency of 0.497. The efficiency was recalculated for SV0 weights of 9.08 and 0.08 which correspond to b-jet efficiencies of 0.405 and 0.576 respectively. In data, for 25 $< p_{\mathrm{T}}(\mathrm{jet}) <$ 85 GeV the b-jet tagging efficiency is expected to vary from 40% to 60% [56]. Table 6.9 gives the fractional errors on ε as a result of the variation in the b-jet tagging efficiency.

b-jet efficiency	Δb-jet efficiency	$\Delta\varepsilon/\varepsilon$
0.576	+7.9%	+7.48%
0.405	-9.2%	-14.76%

Table 6.9: Fractional uncertainty on the efficiency as a result of a shift in the b-tagging efficiency

Tau Identification

The tau ID used relied on a single cut on the EmRadius of the tau candidate. This was set to correspond to a hadronic tau selection efficiency in Monte Carlo of 30%. The EmRadius cuts the for 1-Prong candidates (3-Prong candidates were not used) were varied so as the tau selection efficiency varied by ±10% This was a deliberately conservative estimate. This resulted in a variation of the $t\bar{t}$ efficiency of;

Tau ID efficiency	Δtau ID efficiency	$\Delta\varepsilon/\varepsilon$
0.40	+10%	+22.58%
0.20	-10%	-26.82%

Table 6.10: Fractional uncertainty on the efficiency as a result of a ±10% shift in the tau selection efficiency

Monte Carlo Statistics

Non-QCD backgrounds were subtracted from S using Monte Carlo predictions only. As such there is a systematic uncertainty associated with the Monte Carlo statistics available for these samples. Adding the uncertainties for the samples in quadrature, an overall uncertainty was produced of approximately ±20% where the dominant uncertainty was on the measurement of the W+jets background. The overall systematic error on the non-QCD background subtraction could be reduced by attempting to estimate some of these backgrounds from data.

Overall Errors

In order to obtain a conservative estimate for the total overall systematic on ε, the individual systematics were combined by adding the positive uncertainties in quadrature and then repeating for the negative uncertainties. The values combined, together with the total calculated uncertainty are shown in table 6.11. In addition to the systematic uncertainty on ε, subtraction of Monte Carlo backgrounds contribute an uncertainty of $\pm 20\%$, while the ATLAS luminosity error during 2010 was of the order $\pm 3.4\%$ [71].

Source	Uncertainty (%)
JES	$^{+42}_{-32}$
Generator/PDF	$^{+6}_{-6}$
Top Mass	$^{+7.5}_{-10}$
B-Tag	$^{+7}_{-14}$
Tau ID	$^{+22}_{-26.8}$
Total uncertainty	$^{+53}_{-50}$

Table 6.11: Systematic uncertainties on the efficiency ε for selecting $t\bar{t}$ events via the method described

As can be seen, the overall systematic uncertainty is large ($\pm 50\%$) in the current analysis and is dominated by the uncertainties due to the jet energy scale and the tau identification. However, there are ways in which it is believed that these could be improved with time. Firstly, as mentioned reducing the size of the uncertainty on the JES is a significant aim for ATLAS. It would be hoped that this would fall

as ATLAS running progresses from around 5% to approximately the design target value of 1% [35], leading to an automatic drop in the size of the associated systematic error. More sophisticated analysis techniques could also be applied in time so as to reduce the sensitivity to the JES. This would envolve trying to identify those cuts which were most sensitive to the JES and adjusting them so that the effect became less drastic. Once sufficient statistics became available a logical way to do this would be to look at fitting the mass distributions. This would make better use of a given set of statistics and also have the additional effect of reducing the reliance on the number of events in the sideband regions. The 10% shift in the tau identification efficiency applied is conservative, however one way in which the sensitivity to this could be reduced would be to use $Z \rightarrow \tau\tau$ to try and measure the tau identification efficiency in data when sufficient luminosity becomes available. More sophisticated methods of tau identification than the single variable cut used here would also be likely to help reduce the systematic uncertainty, whilst hopefully also allowing some of the other cuts to be loosened, improving the overall $t\bar{t}$ efficiency. Similarly, if a way could be found to measure some of the other Monte Carlo backgrounds, such as the W+jets, from data then the uncertainty on the Monte Carlo background subtraction could also hopefully be reduced. Over time it would also be reasonable to assume that the performance of the available b-taggers should improve and hence reduce the systematic error accordingly.

6.7.4 Future prospects

As was described in 6.7.1, statistics in the background control regions meant that it was not possible to make a significant measurement of the $t\bar{t}$ cross section with the 2010 data. However, table 6.5 when combined with the expected systematic errors on ε and possibilities for improving them show that a measurement will be possible within the current 2011-2013 LHC run. Advancement in analysis techniques such as fitting distributions and possibly using multivariant techniques for tau identification could reduce the period of time this would take providing the systematics could be controlled. It is therefore possible to consider how the analysis could be evolved in the near future. Firstly, this chapter discussed a method to measure the overall $t\bar{t}$ cross section. However a more interesting figure to study is the branching fraction for $t\bar{t}$ to tau decays as this is where the presence of any new physics, such as a light charged Higgs boson, is likely to appear. Therefore, once sufficient data was available a useful measurement to make would be to make a measurement of the cross section times the branching fraction to taus. Comparing this to similar measurements for muons and electons in $t\bar{t}$ events would therefore provide both a cross check of the standard model and a probe for potential new physics.

6.8 Conclusion

Observing the decay of a $t\bar{t}$ pair to tau + jets is a substantial challenge at a hadron collider due to the nature of the final state. A method was proposed, which de-

liberately avoided sophiticated multivariant techniques in favour of simple cuts, to attempt to measure the $t\bar{t}$ cross section via this channel, using early data from the ATLAS detector at the LHC. The analysis was developed on Monte Carlo events and then applied to 26.4 $\text{pb}^{-1}$of 2010 ATLAS data. A series of deliberately simple cuts were used for event selection, and a cut and count technique used to estimate the number of $t\bar{t}$ events in a window around the hadronic top mass peak. A subtraction of QCD background from data was performed by scaling a number of events from a QCD enriched sample by the ratio of events in a sideband region of the hadronic top mass. It was established that with the current available dataset a statistical error is expected of the order of $\pm 400\%$ and thus a measurement is not feasible at this stage. The systematic error on the $t\bar{t}$ selection efficiency was conservatively estimated to be of the order of $\pm 50\%$. However, it was established via a simple luminosity scaling that a measurement should become statistically possible within the period of the current 2011-2013 LHC run, while a few suggestions were made as to how the systematic uncertainty on the efficiency could be reduced.

Appendix A

p_T[GeV]	CutLevel	EmRadius	StripWidth2	IsolationFraction	EnergyRatio
	Loose	≤0.11	≤0.047	≤0.75	≤1.02
10-25	Medium	≤0.072	≤0.045	≤0.65	≤1.02
	Tight	≤0.055	≤0.033	≤0.32	≤1.01
	Loose	≤0.087	≤0.048	≤0.89	>0.0010
25-45	Medium	≤0.058	≤0.043	≤0.24	>0.0011
	Tight	≤0.048	≤0.0030	≤0.20	>0.023
	Loose	≤0.081	≤0.050	≤0.31	>0.00040
45-70	Medium	≤0.050	≤0.035	≤0.26	>0.00040
	Tight	≤0.037	≤0.035	≤0.26	>0.0028
	Loose	≤0.150	≤0.040	≤0.70	>0.0010
70-100	Medium	≤0.045	≤0.036	≤0.14	>0.029
	Tight	≤0.045	≤0.015	≤0.058	>0.029
	Loose	≤0.500	≤0.030	≤0.60	>0.00033
>100	Medium	≤0.034	≤0.030	≤0.60	>0.00033
	Tight	≤0.034	≤0.00069	≤0.049	>0.0015

Table A.1: Calorimeter only safe cut values for identification of 1-prong hadronic taus [53]

p_T[GeV]	CutLevel	EmRadius	StripWidth2	IsolationFraction	EnergyRatio
	Loose	≤0.21	≤0.057	≤0.96	≤1.02
10-25	Medium	≤0.15	≤0.056	≤0.90	≤1.02
	Tight	≤0.096	≤0.048	≤0.62	≤1.01
	Loose	≤0.15	≤0.045	≤0.79	≤1.01
25-45	Medium	≤0.088	≤0.044	≤0.68	≤1.01
	Tight	≤0.068	≤0.044	≤0.42	≤1.01
	Loose	≤0.25	≤0.031	≤0.25	≤1.08
45-70	Medium	≤0.071	≤0.031	≤0.25	≤1.03
	Tight	≤0.053	≤0.026	≤0.25	≤1.01
	Loose	≤0.23	≤0.036	≤0.50	≤1.02
70-100	Medium	≤0.061	≤0.035	≤0.20	≤1.01
	Tight	≤0.048	≤0.035	≤0.18	≤1.00
	Loose	≤0.071	≤0.038	≤0.47	≤1.00
>100	Medium	≤0.061	≤0.037	≤0.20	≤1.00
	Tight	≤0.036	≤0.030	≤0.18	≤0.99

Table A.2: Calorimeter only safe cut values for identification of 3-prong hadronic taus [53]

Bibliography

[1] Wolfgang Wagner, Top quark physics in hadron collisions, *Rept. Prog. Phys.* **68**, 2409–2494 (2005).

[2] M Herrero, The Standard Model, Technical Report arXiv:hep-ph/9812242v1, Universidad Autonoma de Madrid, December 1998.

[3] A. Quadt, Top quark physics at hadron colliders, *The European Physical Journal C - Particles and Fields* **48**, 835–1000 (2006), 10.1140/epjc/s2006-02631-6.

[4] M. Mangano and T. Trippe, The top quark, *The European Physical Journal C - Particles and Fields* **15**, 385–391 (2000), 10.1007/BF02683451.

[5] S. Willenbrock, Top quark theory, (1996).

[6] C. Troncon, Top Quark Physics in Atlas at the Lhc, in *High Energy Physics, ICHEP 2004*, edited by H. Chen, D. Du, W. Li, & C. Lu, pages 1170–1173, Apr. 2005.

[7] T. M. Liss and P. L. Tipton, The discovery of the top quark, *Scientific American 277 N3* , 54–59 ((1997)).

[8] F. Abe et al., Evidence for top quark production in $p\bar{p}$ collisions at $\sqrt{s} = 1.8$ TeV, *Phys. Rev. D* **50**(5), 2966–3026 (Sep 1994).

[9] K. Nakamura et al. (Particle Data Group), Review of Particle Physics, *J. Phys. G* .

[10] Search for top pair candidate events in ATLAS at sqrt(s)=7 TeV, Technical Report ATLAS-CONF-2010-063, CERN, Geneva, Jul 2010.

[11] Marcello Barisonzi, Top physics at ATLAS, *AIP Conf. Proc.* **794**, 85–88 (2005).

[12] The Durham HepData Project, Durham Online Parton Distributions, `http://hepdata.cedar.ac.uk/pdf/pdf3.html`, (accessed 18/01/2011).

[13] Georges Aad et al., Measurement of the top quark-pair production cross section with ATLAS in pp collisions at $\sqrt{s}$ =7 TeV, (2010).

[14] R. Bonciani and A. Ferroglia, Top Quark Production at Hadron Colliders: an Overview, *PoS* **EPS-HEP2009**, 350 (2009).

[15] W. J. Murray, editor, *Proceedings of the School for Experimental High Energy Physics Students*, Science & Technology Facilities Council, September 2009, Technical Report : RAL-TR-2010-010.

[16] S. Lai on behalf of the ATLAS Collaboration, Tau Physics at the LHC with ATLAS, Technical Report ATL-PHYS-PROC-2009-126, Albert-Ludwigs Universitat Freiburg, 79104,Freiburg,Germany, October 2009.

[17] Catherine Biscarat and Mireia Dosil, Charged Higgs search in top quark decays

with the ATLAS detector, ATLAS Publication Note ATL-PHYS-2003-038, IFAE,Universitat Autonomade Barcelona, E-08193 Barcelona, Spain, 2003.

[18] Particle Data Group, Review of Particle Physics, *Journal of Physics G* **33** (July 2006).

[19] A.-C.Le Bihan et al, Identification of hadronic τ decays with ATLAS detector, ATLAS Internal Note ATL-PHYS-INT-2008-003, CERN, January 2008.

[20] D. Boussard et al., The Large Hadron Collider Conceptual Design, Technical Report CERN/AC/95-05, CERN, Geneva, 1995.

[21] ATLAS Collaboration, Luminosity and Run Statistics for 2010 Beam Data, `https://twiki.cern.ch/twiki/bin/view/AtlasPublic/RunStatsPublicResults2%010`, March 2011, (accessed 31/03/2011).

[22] O. Bruning et al, LHC design report. Vol. I: The LHC main ring, Technical Report CERN-2004-003-V-1, CERN, Geneva, 2004.

[23] L. Evans and P. Bryant, LHC Machine, Technical Report JINST 3 (2008) S08001, CERN, Geneva, 2008.

[24] P. Baudrenghien, Beam Control for Protons and Ions, Technical report, CERN, Geneva, 1999.

[25] K. Aamodt et al., The ALICE experiment at the CERN LHC, *JINST* **3**, S08002 (2008).

[26] G. Aad et al. ATLAS Collaboration, The ATLAS experiment at the CERN

Large Hadron Collider, Technical Report JINST 3 (2008) S08003, CERN, Geneva, 2008.

[27] S Chatrchyan et al. The CMS Collaboration, The CMS experiment at the CERN Large Hadron Collider, Technical Report JINST 3 (2008) S08004, CERN, Geneva, 2008.

[28] A Augusto Alves Jr et al The LHCb Collaboration, The LHCb Detector at the LHC, Technical Report JINST 3 (2008) S08005, CERN, Geneva, 2008.

[29] G. Anelli et al., The TOTEM experiment at the CERN Large Hadron Collider, *JINST* **3**, S08007 (2008).

[30] O Adriani, L Bonechi, M Bongi, G Castellini, R D'Alessandro, D A Faus, K Fukui, M Grandi, M Haguenauer, Y Itow, K Kasahara, D Macina, T Mase, K Masuda, Y Matsubara, H Menjo, M Mizuishi, Y Muraki, P Papini, A L Perrot, S Ricciarini, T Sako, Y Shimizu, K Taki, T Tamura, S Torii, A Tricomi, W C Turner, J Velasco, A Viciani, H Watanabe, and K Yoshida, The LHCf detector at the CERN Large Hadron Collider, *J. Instrum.* **3**, S08006 (2008).

[31] F. Gianotti, Collider Physics: LHC, Technical Report ATL-CONF-2000-001, CERN, Geneva, 2000.

[32] ATLAS Collaboration, ATLAS Detector and Physics Performance Technical Design Report: Vol. II, Technical Report CERN/LHCC/99-15, CERN, Geneva, 1999.

[33] G et al. Aad, trigger Expected performance of the ATLAS experiment: detector and physics, CERN, Geneva, 2009.

[34] ATLAS Collaboration, ATLAS Technical Proposal, Technical Report CERN/LHCC/94-43, CERN, Geneva, 1994.

[35] ATLAS Collaboration, ATLAS Detector and Physics Performance Technical Design Report: Vol. I, Technical Report CERN/LHCC/99-14, CERN, Geneva, 1999.

[36] ATLAS Collaboration, Liquid Argon Calorimeter Technical Design Report, Technical Report CERN/LHCC/96-41, CERN, Geneva, 1996.

[37] ATLAS Collaboration, ATLAS Calorimeter Performance, Technical Report CERN/LHCC/96-40, CERN, Geneva, 1996.

[38] ATLAS Collaboration, Tile Calorimeter Technical Design Report, Technical Report CERN/LHCC/96-42, CERN, Geneva, 1996.

[39] Cavendish HEP Theory Group, The MC@NLO Package, `http://www.hep.phy.cam.ac.uk/theory/webber/MCatNLO/`, December 2010, (accessed 09/10/2010).

[40] Richard Corke Stephen Mrenna Peter Skands Torbjrn Sjstrand, Stefan Ask, Pythia, `http://home.thep.lu.se/~torbjorn/Pythia.html`, December 2010, (accessed 09/10/2010).

[41] Mike Seymour et al., HERWIG, `http://hepwww.rl.ac.uk/theory/seymour/herwig/`, December 2010, (accessed 09/10/2010).

[42] Geant4 Collaboration, Geant4, http://geant4.web.cern.ch/geant4/, December 2010, (accessed 09/10/2010).

[43] ATLAS L1Calo Group, The ATLAS Level-1 Calorimeter Trigger, Technical Report 2008 JINST 3 P03001, CERN, Geneva, March 2008.

[44] ATLAS Collaboration, Level-1 Trigger Technical Design Report, Technical Report CERN/LHCC/98-14, CERN, Geneva, 1998.

[45] H. P. Beck et al., The ATLAS Event Filter, CHEP paper, 1998.

[46] ATLAS L1Calo Group, ATLAS Level-1 Calorimeter Trigger Algorithms, Technical Report ATL-DAQ-2004-011, CERN, Geneva, 2004.

[47] The ATLAS Collaboration, Cut bases Identification of Hadronic τ Decays in Early ATLAS Data, 2010, ATLAS Publication Note,ATL-PHYS-PUB-2010-001.

[48] The ATLAS Collaboration, Prospects for measuring top pair production in the dilepton channel with early ATLAS data at $\sqrt{s} = 10TeV$, ATLAS Publication Note ATL-PHYS-PUB-2009-086, CERN, August 2009.

[49] M Wolter, Tau identification using multivariate techniques in ATLAS, Technical Report ATL-PHYS-PROC-2009-016. ATL-COM-PHYS-2008-286, CERN, Geneva, Dec 2008.

[50] F.Tarrade on behalf of the ATLAS Collaboration, Reconstruction and identification of hadronic τ decays in ATLAS, *Nuclear Physics B (Proc. Suppl.)* **169**, 357–362 (2007).

[51] ATLAS Tau Working Group, Tau Algorithm Merging, https://twiki.cern.ch/twiki/bin/view/AtlasProtected/TauAlgorithmMerging%, September 2008, (accessed 21/10/2010).

[52] Cut based identification of hadronic tau decays, Technical Report ATL-PHYS-PUB-2010-001, CERN, Geneva, Jan 2010.

[53] P Bechtle, B Gosdzik, and S Lai, Status report on tauID with safe variables, http://indico.cern.ch/conferenceDisplay.py?confId=43438, December 2008, Talk given to the ATLAS Tau WG (accessed 02/11/2010).

[54] ATLAS Tau Working Group, Tau EDM, https://twiki.cern.ch/twiki/bin/view/AtlasProtected/TauEDM, June 2010, (accessed 22/10/2010).

[55] P Bechtle, Y Coadou, E Coniavitis, M Dam, EN Dawe, L Dell'Asta, S Dhaliwal, M Flechl, J Godfrey, B Gosdzik, J Griffiths, M Janus, A Kaczmarska, S Kuehn, S Lai, R Mazini, Z Meng, DC O'Neil, R Reece, S Rosati, and S Tsuno, Tau identication performance with the ATLAS detector, Technical Report ATL-COM-PHYS-2010-599, CERN, Geneva, Aug 2010, COM backup note.

[56] Georges Aad et al., Measurement of the top quark-pair production cross section with ATLAS in pp collisions at $\sqrt{s} = 7$ TeV. oai:cds.cern.ch:1312983, Technical Report arXiv:1012.1792. CERN-PH-EP-2010-064, CERN, Geneva, Dec 2010, Comments: 30 pages plus author list (50 pages total), 9 figures, 11 tables.

[57] Sven Moch and Peter Uwer, Theoretical status and prospects for top-quark pair production at hadron colliders, *Phys. Rev.* **D78**, 034003 (2008).

[58] ATLAS Top Working Group, Top MC2009, https://twiki.cern.ch/twiki/bin/view/AtlasProtected/TopMC2009, March 2011, (accessed 31/03/2011).

[59] ATLAS Collaboration, Jet/Tau and missing ET Samples, https://twiki.cern.ch/twiki/bin/view/AtlasProtected/JetMissingET, January 2008, (accessed 31/03/2011).

[60] ATLAS Collaboration, Data Periods, https://twiki.cern.ch/twiki/bin/view/AtlasProtected/DataPeriods, March 2011, (accessed 31/03/2011).

[61] ATLAS Collaboration, Trigger Physics Menu, https://twiki.cern.ch/twiki/bin/view/Atlas/TriggerPhysicsMenu, February 2011, (accessed 31/03/2011).

[62] ATLAS Collaboration, Index of Standard GRL, http://atlasdqm.web.cern.ch/atlasdqm/grlgen/StandardGRL/, December 2010, (accessed 31/03/2011).

[63] ATLAS Collaboration, ATLAS Luminosity Calculator, https://atlas-datasummary.cern.ch/lumicalc/, March 2011, (accessed 31/03/2011).

[64] ATLAS Jet Etmiss Working Group, Jet Analysis, https://twiki.cern.ch/twiki/bin/view/AtlasProtected/JetAnalysisDefault_%jet_collections, September 2010, (accessed 31/03/2011).

[65] ATLAS Collaboration, Inputs to jet reconstruction, https://twiki.cern.ch/twiki/bin/view/AtlasProtected/JetInputs, December 2009, (accessed 31/03/2011).

[66] ATLAS Collaboration, EtMiss Ref Final, https://twiki.cern.ch/twiki/bin/view/AtlasProtected/EtMissRefFinalNew_d%efault_selection_criteria_a, November 2010, (accessed 31/03/2011).

[67] ATLAS EGamma Working Group, Electron Reconstruction, https://twiki.cern.ch/twiki/bin/view/AtlasProtected/ElectronReconstruct%ionStandard_electron_cluster_based, January 2011, (accessed 31/03/2011).

[68] Prospects for measuring top pair production in the dilepton channel with early ATLAS data at $\sqrt{s}$=10 TeV, Technical Report ATL-PHYS-PUB-2009-086, CERN, Geneva, Aug 2009.

[69] et al. B. Abbott, Study on reconstructed object definition and selection for top physics, Technical Report ATL-COM-PHYS-2009-633, CERN, Geneva, 2009, limited distribution.

[70] Prospects for the Top Pair Production Cross-section at $\sqrt{s}$ = 10 TeV in the Single Lepton Channel in ATLAS, Technical Report ATL-PHYS-PUB-2009-087, CERN, Geneva, Aug 2009.

[71] Updated Luminosity Determination in pp Collisions at root(s)=7 TeV using the ATLAS Detector, Technical Report ATLAS-CONF-2011-011, CERN, Geneva, Mar 2011.

[72] Measurement of the top quark-pair cross-section with ATLAS in pp collisions at

sqrt(s) = 7 TeV in the single-lepton channel using b tagging, Technical Report ATLAS-CONF-2011-035, CERN, Geneva, Mar 2011.

[73] Powheg Contributors, The Powheg Box, http://powhegbox.mib.infn.it/, (accessed 31/03/2011).

[74] CTEQ Collaboration, CTEQ PDF Group, http://www.phys.psu.edu/~cteq/, (accessed 31/03/2011).

[75] Borut Paul Kersevan and Elzbieta Richter-Was, AcerMC Monte-Carlo Generator, http://borut.home.cern.ch/borut/, (accessed 31/03/2011).

[76] MRS/MRST/MSTW Collaboration, MRS/MRST/MSTW PARTON DISTRIBUTIONS, http://durpdg.dur.ac.uk/hepdata/mrs.html, (accessed 31/03/2011).